



# POLITECNICO MILANO 1863

**SCHOOL OF INDUSTRIAL AND INFORMATION ENGINEERING**

LAUREA MAGISTRALE IN ENGINEERING PHYSICS

---

A micro-optomechanical modulator realized  
by femtosecond laser micromachining

**Candidate**

Michele Spagnolo

**Matriculation number**

876015

**Advisor**

Dr. Roberto Osellame

**Co-advisor**

Dr. Andrea Crespi

---

ACADEMIC YEAR 2017-2018





*Ad Anna e Gianmarco.*



# Introduzione

La Microfabbricazione con Laser a Femtosecondi (FLM) è una tecnica versatile che negli ultimi due decenni ha avuto un ampio e profondo sviluppo. L'intensità di picco estremamente alta associata agli impulsi laser ultrabrevi li rende particolarmente attraenti per produrre modifiche localizzate permanenti su diversi tipi di materiali. Tra questi, i materiali trasparenti meritano particolare considerazione. In un materiale trasparente, infatti, dove il gap energetico tra le bande è superiore all'energia dei fotoni incidenti e perciò l'assorbimento lineare è soppresso, l'assorbimento può avvenire solo tramite processi non lineari. Se il fascio laser è focalizzato in un punto all'interno del volume del materiale, tali processi accadono solo in una piccola regione attorno al punto focale, creando un piccolo centro di assorbimento dove l'energia può localmente depositarsi e produrre modifiche permanenti. Muovendo la posizione relativa del fuoco rispetto al campione è possibile microfabbricare geometrie tridimensionali di quasi arbitraria complessità.

In diversi tipi di vetro, l'esposizione a impulsi a femtosecondi può portare, se correttamente eseguita, ad un aumento localizzato e permanente dell'indice di rifrazione, e ciò consente di scrivere guide d'onda ottiche all'interno del materiale. Questa fu una delle prime scoperte nella storia della FLM, e al giorno d'oggi con questa tecnica vengono realizzati circuiti fotonici di grande complessità. Le loro applicazioni includono, tra gli esempi di maggiore rilievo, l'implementazione di protocolli di informazione quantistica dove gli stati quantistici sono codificati su singoli fotoni e le operazioni sono eseguite tramite opportuni schemi interferometrici.

D'altro canto, la formazione di peculiari nano-fratture periodiche nel fused silica e alcuni altri vetri è stata sfruttata per lo sviluppo di una tecnica in due step denominata FLICE (Irraggiamento con Laser a Femtosecondi seguito da Etching Chimico), in cui il vetro viene prima irraggiato e successivamente immerso in acido fluoridrico, in modo che le parti irraggiate vengano selettivamente scavate. Questo ha consentito la realizzazione di canali sepolti che hanno trovato applicazione nella microfluidica. In particolare, l'integrazione di componenti ottici e microfluidici nello stesso substrato ha aperto la strada a dispositivi lab-on-a-chip optofluidici capaci di eseguire analisi microbiologiche in modo efficiente e compatto.

Entrambe le applicazioni traggono grande beneficio dalla possibilità di riconfigurare le proprietà ottiche del dispositivo. Molto recentemente, è stata dimostrata una tecnica per eseguire modulazione di fase in circuiti ottici scritti con laser a femtosecondi. Si fabbricano dei resistori d'oro sulla superficie del substrato di vetro per creare dei micro-riscaldatori, e si sfrutta l'effetto termo-ottico per modificare l'indice di rifrazione e dunque il cammino ottico della

guida, fino ad uno shift completo di  $2\pi$ . I limiti principali di questa tecnica sono la dissipazione di potenza per il funzionamento in continua, il crosstalk termico tra i resistori, ma soprattutto una limitazione intrinseca della banda dovuta al tempo di diffusione termico. I tempi di riconfigurazione sono tipicamente nell'ordine di decine o centinaia di millisecondi.

L'idea fondamentale alla base di questo lavoro è di ottenere una modulazione ottica sfruttando effetti meccanici anziché termici. Una modulazione optomeccanica potrebbe infatti essere la soluzione per superare le limitazioni degli shifter termici attualmente in uso, poiché le strutture micromeccaniche possono trarre vantaggio dal loro comportamento intrinsecamente risonante per raggiungere regimi molto più veloci, avendo frequenze di risonanza tipicamente nell'ordine di  $10^4$  o  $10^5$  Hz.

Nell'ambito di questo progetto, ci prefiggiamo di realizzare un modulatore di *intensità* optomeccanico tramite l'integrazione di una guida d'onda all'interno di un cantilever (cioè una struttura con un'estremità libera oscillante). La guida attraverserà il cantilever per tutta la lunghezza, di modo che l'oscillazione del cantilever causi un disallineamento delle due estremità della guida. Il disallineamento produrrà un disaccoppiamento dei modi guidati, perciò il movimento meccanico si tradurrà in una modulazione dell'intensità ottica trasmessa.

Nel primo capitolo di questa tesi diamo, senza pretesa di esaustività, una breve panoramica sulla teoria e le applicazioni dei risonatori micromeccanici. Ci concentriamo principalmente sulla dinamica del cantilever e introduciamo un semplice modello di oscillatore armonico per dare conto del suo comportamento a risonanza. Discutiamo poi il concetto di quality-factor e alcuni modelli teorici che cercano di darne una previsione a priori. Il Capitolo 2 introduce i fondamenti della Microfabbricazione con Laser a Femtosecondi. In dettaglio, discutiamo la scrittura di guide e confrontiamo la FLICE con altre tecniche di microstrutturazione, in particolare l'ablazione a contatto con acqua. Passiamo poi al Capitolo 3 per dare una breve descrizione del nostro apparato sperimentale e i diversi setup impiegati per la caratterizzazione di un dispositivo. Nel Capitolo 4 discutiamo la progettazione del nostro modulatore optomeccanico: ne spieghiamo i principi fisici, ne individuiamo le proprietà critiche, discutiamo la scelta del substrato e, di conseguenza, la scelta della tecnica di microstrutturazione. Infine, i nostri risultati sperimentali sono presentati nei capitoli 5 e 6.

Dimostreremo l'ottimizzazione della tecnica di ablazione a contatto con l'acqua, la sua applicazione per rimuovere efficientemente porzioni significative di volume, ed il suo utilizzo per la fabbricazione del cantilever. Descriveremo il processo di caratterizzazione delle proprietà statiche e dinamiche del cantilever e forniremo modelli teorici in grado di predire con ottima accuratezza i nostri risultati sperimentali. Dimostreremo una modulazione del segnale dell'ordine del 10%.

# Contents

<b>Introduction</b>	<b>ix</b>
<b>1 Micromechanical resonators</b>	<b>1</b>
1.1 Theory of harmonic oscillations . . . . .	2
1.1.1 One-dimensional damped mass-spring system . . . . .	2
1.1.2 Quality factor . . . . .	3
1.2 Micro-cantilevers . . . . .	4
1.2.1 Statics . . . . .	4
1.2.2 Dynamics . . . . .	6
1.3 Quality factor of micro-cantilevers . . . . .	7
1.3.1 Validity of the 1D harmonic oscillator model . . . . .	7
1.3.2 Modelling friction . . . . .	9
1.4 State of the art and applications . . . . .	11
1.4.1 Microfabrication . . . . .	11
1.4.2 Readout schemes . . . . .	13
1.4.3 AM-AFM and force sensing . . . . .	15
<b>2 Femtosecond Laser Micromachining</b>	<b>17</b>
2.1 Physical principles . . . . .	17
2.1.1 Nonlinear absorption in dielectrics . . . . .	17
2.1.2 Space localization and bulk micromachining . . . . .	18
2.1.3 Relevant parameters . . . . .	18
2.2 Femtosecond laser waveguide writing . . . . .	20
2.2.1 Operational principles . . . . .	20
2.2.2 Applications . . . . .	21
2.3 Glass microstructuring . . . . .	23
2.3.1 FLICE technique . . . . .	23
2.3.2 Direct laser ablation . . . . .	24
2.3.3 Water-assisted ablation from the rear surface . . . . .	25
<b>3 Materials and methods</b>	<b>29</b>
3.1 Fabrication setup . . . . .	29
3.2 Characterization techniques . . . . .	30
3.2.1 Microscope inspection . . . . .	30
3.2.2 Waveguide characterization . . . . .	31
3.3 Fiber pigtailling . . . . .	33
3.3.1 Nanopositioning setup . . . . .	33
3.3.2 Pigtail operation . . . . .	35

<b>4</b>	<b>Design of the optomechanical modulator</b>	<b>37</b>
4.1	Working principle . . . . .	37
4.2	Choice of the substrate . . . . .	39
4.3	Geometry . . . . .	40
4.3.1	Dimensions . . . . .	40
4.3.2	In-plane VS out-of-plane oscillation . . . . .	41
<b>5</b>	<b>Fabrication of the microcantilever</b>	<b>43</b>
5.1	Developement of water-assisted ablation . . . . .	43
5.1.1	Sample mount and water supply . . . . .	44
5.1.2	Trenches . . . . .	45
5.1.3	Boxes . . . . .	50
5.1.4	Horizontal ablation . . . . .	53
5.1.5	Bubbles . . . . .	54
5.2	The cantilever . . . . .	56
5.3	The waveguide . . . . .	58
<b>6</b>	<b>Static and dynamic characterization</b>	<b>61</b>
6.1	Static characterization . . . . .	61
6.1.1	Experiment and results . . . . .	61
6.1.2	Discussion . . . . .	61
6.2	Dynamic characterization . . . . .	64
6.2.1	Time domain characterization . . . . .	64
6.2.2	Frequency domain characterization . . . . .	65
6.2.3	Results . . . . .	67
6.2.4	Discussion . . . . .	69
6.3	Quality factor . . . . .	73
6.3.1	Theory of an harmonic oscillator actuated by the base . . . . .	73
6.3.2	Measurements and results . . . . .	76
6.3.3	Maximum amplitude of oscillation . . . . .	79
6.3.4	Q-factor at lower pressure . . . . .	80
	<b>Conclusions and future perspectives</b>	<b>83</b>
	<b>Aknowledgements</b>	<b>85</b>
	<b>References</b>	<b>87</b>

# Introduction

Femtosecond Laser Micromachining (or FLM) is a versatile technique that has shown in the last two decades a profound and widespread development. The extremely high peak intensity associated to ultra-short laser pulses renders them particularly appealing for producing permanent, localized modifications on several types of material. Among these, transparent materials deserve special consideration. In a transparent material, where the energy bandgap is larger than the energy of the impinging photons and linear absorption is therefore suppressed, absorption can only take place through nonlinear processes. If the laser beam is focused in a point deep in the bulk of the substrate, such processes happen only in a very narrow region close to the focal point, creating a small absorption spot where energy is locally deposited and can lead to permanent modifications. By moving the relative position of the focal point with respect to the sample, micromachining with almost arbitrary and three-dimensional geometry becomes possible.

In several types of glass, the exposure to femtosecond pulses can lead, when properly executed, to a permanent and localized increase of refractive index which enables to write optical waveguides within the bulk of the substrate. This was among the early discoveries in the history of FLM, and nowadays integrated photonic circuits of great complexity can be realized. Their applications include, among the most prominent examples, the implementation of quantum information protocols where quantum states are encoded in photons and the operations are performed by suitable interferometric schemes.

On the other hand, the formation of peculiar self-organized nanocracks was exploited in fused silica and few other glasses for the development of a two-step technique called FLICE (Femtosecond Laser Irradiation followed by Chemical Etching), where the glass is first irradiated and subsequently immersed in hydrofluoric acid, so that the irradiated regions are selectively etched. This enables the realization of buried channels that have found application in microfluidics. In particular, the integration of microfluidic and optical components on the same substrate has opened the way to optofluidic lab-on-a-chip devices capable of performing microbiological analysis efficiently and compactly.

Both applications greatly benefit from a reconfigurability of the optical properties of the device. Very recently, a technique for performing phase modulation in femtosecond laser-written circuits has been demonstrated. Gold resistors are fabricated on top of the glass substrate to act as local heaters, and the thermo-optic effect is exploited to change the refractive index and thus the optical path of the waveguide, up to a complete phase shift of  $2\pi$ . The main drawbacks of this technique are the power consumption in DC operation, the thermal crosstalk between heaters and, most importantly, an intrinsic bandwidth limita-

tion due to heat diffusion time. Reconfiguration times are typically in the order of tens or hundreds of milliseconds.

The fundamental idea at the basis of our work is to obtain optical modulation by exploiting mechanical effects, rather than thermal. Optomechanical modulation could be indeed the key to overcome the fundamental limitations of the currently employed thermal shifters. In fact, micromechanical structures can take advantage of their intrinsic *resonant* behavior to achieve much faster operation, as their frequency of resonance are typically in the order of  $10^4$  to  $10^5$  Hz.

Here we aim at the realization of an optomechanical *intensity* modulator by integrating a straight waveguide within a cantilever structure. The waveguide will cross the cantilever along its whole length, in such a way that the oscillation of the cantilever will cause a misalignment of the two extremities of the waveguide. The misalignment produces a decoupling of the guided modes, hence the mechanical movement will translate into a modulation of the transmitted optical intensity.

In the first chapter of this work we give, with no claim of completeness, a brief review on theory and applications of micromechanical resonators. We specifically focus on the dynamics of a cantilever beam and we introduce a simple harmonic oscillator model to account for its resonant behaviour. We then discuss the concept of quality factor and some theoretical models that try to give a-priori predictions. Chapter 2 introduces the fundamentals of Femtosecond Laser Micromachining. In detail, we discuss waveguide writing and we compare the FLICE technique with other microstructuring techniques, namely water-assisted ablation. We then move to Chapter 3 to give a brief description of our experimental apparatus and the different setups employed for the characterization of a device. In Chapter 4 we discuss the design of our optomechanical modulator: we explain the physical principles of operation, we individuate its critical properties, we discuss the choice of substrate and, consequently, the choice of microstructuring technique. Finally, our experimental results will be presented in Chapters 5 and 6.



# Chapter 1

## Micromechanical resonators

Sensors based on mechanical resonators are widely used for the most diverse applications [1]. These devices work by coupling the physical quantity of interest to a measurable modification of the mechanical properties of the transducer. Resonant structures are particularly appealing for this task, as their behaviour (in terms of amplitude, frequency and phase) can be very sensitive to such modifications and at the same time provide great flexibility. The development of silicon-based micro- and nanotechnologies witnessed in the last three decades has allowed an extreme miniaturization of such components into micro(nano)electromechanical systems (MEMS). These have been able to provide compact, high precision, low cost sensors and actuators that are now some of the most pervasive technology available, finding as much application in aerospace and defence as in everyday life devices [2]. The integration of optical components in micro-*opto*-electromechanical systems (MOEMS) has emerged in recent years as new, promising ground for further innovation [3].

In the following, we shall briefly recall the theory of harmonic oscillations through the well-known problem of the one-dimensional damped mass-spring system. This theory is generally applicable to almost any mechanical resonator and, despite its simplicity, provides valuable insights into the mechanisms of resonance, allowing for a simple formal definition of the *quality factor* (often abbreviated in *Q-factor*) of the resonator which, as later discussed, is its single most important figure of merit in almost any practical application. We then move to the actual description of the physics of cantilevers. We present a simple theoretical model that accounts for its static and dynamic behaviour, where we show that the cantilever *can* be indeed idealized as a 1D harmonic oscillator and we discuss the limits of validity of such model, particularly regarding the modelling of damping due to air friction. Finally, we shall briefly review some state of the art regarding cantilevers' fabrication processes, readout methods and applications.

## 1.1 Theory of harmonic oscillations

### 1.1.1 One-dimensional damped mass-spring system

Let us consider the system schematized in FIG. 1.1. When the mass is displaced from its rest position, the spring exerts a force  $F_{\text{spring}} = -kx$  where  $k$  is the elastic constant. Let us further assume that viscous drag is present, for example due to air friction, that is opposite and proportional to the velocity of the body through a linear coefficient  $\gamma$  called *viscous friction coefficient*, so that  $F_{\text{drag}} = -\gamma\dot{x}$ . Finally, let us introduce some external force  $F$  that acts on the mass, and the equation of motion of the system reads as

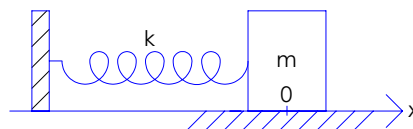


FIGURE 1.1: Damped mass-spring system. The rest position of the spring is assumed to be in the origin of the axis.

$$m\ddot{x} = -\gamma\dot{x} - kx + F \quad (1.1)$$

Actually, the most commonly employed form of Eq. (1.1) is the following

$$\ddot{x} + 2\zeta\omega_0\dot{x} + \omega_0^2x = f \quad (1.2)$$

where

$$\omega_0 = \sqrt{k/m}; \quad \zeta = \gamma/2m\omega_0; \quad f = F/m. \quad (1.3)$$

$\omega_0$  is called *natural frequency* (or *resonance frequency*),  $\zeta$  is called *damping coefficient*. The response of the system can be solved in terms of sinusoidal components. A convenient tool to perform such analysis is the Laplace transform, which is commonly used to describe dynamic systems and to quickly evaluate and compare their responses. In the Laplace domain, Eq. (1.2) reads as

$$x(s) = \frac{f(s)}{s^2 + 2\zeta\omega_0s + \omega_0^2} = T(s)f(s) \quad (1.4)$$

where

$$T(s) = \frac{1}{s^2 + 2\zeta\omega_0s + \omega_0^2} \quad (1.5)$$

is the *transfer function* of the dynamic system. The fundamental theorem of frequency response states that when an asymptotically stable linear-time-invariant system is fed with a sinusoidal input of the form  $f(t) = A \sin(\omega t + \varphi)$ , the output is in the form  $x(t) = B \sin(\omega t + \psi)$ , where  $B = A|T(j\omega)|$  and  $\psi = \varphi + \arg(T(j\omega))$ . In other words, the frequency response of the system is fully determined (both in amplitude and phase) by the form of its transfer function. The Bode diagram, where amplitude and phase are both plotted in logarithmic scale versus the angular frequency, is commonly employed to evaluate frequency responses. The Bode diagram associated to the transfer function of Eq. (1.5) is shown in FIG. 1.2 for  $\omega_0 = 10 \text{ krad s}^{-1}$  and three values of  $\zeta$ . The amplitude peaks and the abrupt  $\pi$ -phase-shift around  $\omega_0$  are typical of resonant behaviour. FIG. 1.2 clearly shows that the height of the peak increases when  $\zeta$  decreases. This is a general property of underdamped ( $\zeta < 1$ ) systems.

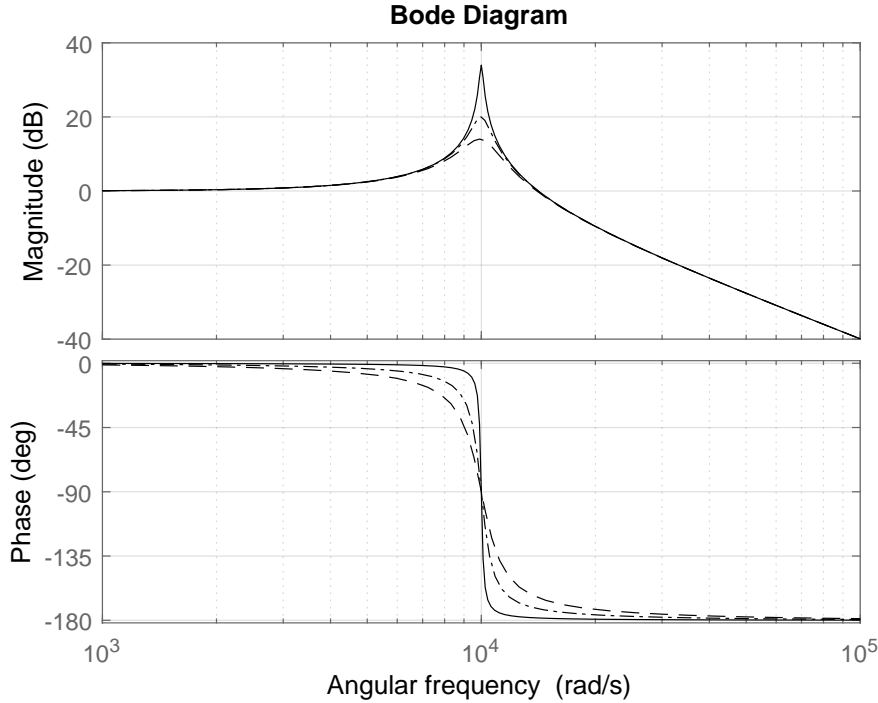


FIGURE 1.2: Frequency response of a damped harmonic oscillator with  $\omega_0 = 10 \text{ krad s}^{-1}$  and  $\zeta = 0.1$  (dashed line),  $\zeta = 0.05$  (dash-dot line),  $\zeta = 0.01$  (continuous line). Amplitude is normalized to its value in stationary condition.

### 1.1.2 Quality factor

As we mentioned, the Q-factor is the single most important figure of merit of a resonator. Its formal definition is not univocal in literature, as the definition is often adapted to the particular application or to the theoretical approach (see for example [4] and [5]). Its physical meaning, however, is absolutely clear and profound, and is twofold:

- the Q-factor is a measure of how much the frequency response of the device is peaked around its resonant frequency: a higher and narrower peak corresponds to a higher Q-factor;
- the Q-factor is a measure of how much energy the resonator loses per cycle with respect to its total energy: smaller losses correspond to higher Q-factors.

In this work, we will consider the Q-factor as defined by

$$Q = \frac{\omega_0}{\Delta\omega_{\text{FWHM}}} \quad (1.6)$$

where  $\Delta\omega_{\text{FWHM}}$  is the full width of the peak at  $1/\sqrt{2}$  of the amplitude maximum (that is  $1/2$  of the power maximum, hence the acronym *full width at half*

*maximum*). For a simple harmonic oscillator with small damping (that is  $\zeta \ll 1$ ), it is rather straightforward to demonstrate, starting from the transfer function of Eq. (1.5), that

$$Q = \frac{\omega_0}{\Delta\omega_{\text{FWHM}}} = \frac{1}{2\zeta} \quad (1.7)$$

and that the amplitude peak corresponds to

$$T_{\text{max}} = |T(j\omega_{\text{max}})| = \frac{1}{2\zeta\omega_0^2} = \frac{Q}{\omega_0^2} \quad (1.8)$$

where

$$\omega_{\text{max}} = \omega_0 \sqrt{1 - 2\zeta^2} \quad (1.9)$$

A system with smaller damping factor (meaning smaller energy losses) has a higher Q-factor. A higher Q-factor produces a narrower resonant peak and a larger amplification factor, as given by  $T_{\text{max}}$ . In Sect. 1.4.3 we shall give a brief but meaningful example of its great importance for applications.

## 1.2 Micro-cantilevers

A *cantilever* is a beam anchored at one extremity and free at the other. The static and dynamic behaviour of such structure are among the archetypical and most extensively studied problems of structural mechanics. Cantilever-like structures have been largely used for sensing application for long time [1] because of their simple and predictable behaviour, but their brake into large-scale market is mostly connected to the invention of AFM (Atomic Force Microscopy) in 1986 [6]. Nowadays, the most common implementation of AFM is based on amplitude-modulation (AM) resonant operation [7], whose resolution entirely depends on the *quality-factor* of the cantilever (see Sect. 1.4.3 for a brief example). In addition, cantilevers find applications in an wide variety of other fields, particularly in force sensing and chemical and biological sensing [8]. Cantilevers made of piezoelectric materials have recently emerged as a promising tool for energy harvesting: some external mechanical energy (like the vibrations of a watch on a person's wrist) is coupled to the oscillation of the beam and transformed into deformation energy of the piezo, which turns it into an electric potential [9].

What most applications have in common is that they rely on the well-known, easily predictable resonant behaviour of the beam. All their figures of merit (sensitivity of the sensors, efficiency of the energy harvesters, and so on) are strongly dependant on the Q-factor of the resonator, which has therefore been the object of extensive theoretical and experimental investigation (see Sect. 1.3).

### 1.2.1 Statics

The physics of the cantilever is treated in any structural mechanics textbook under the so-called Euler-Bernoulli beam theory [10], which we briefly recall here. Let us consider a simple rectangular beam such as the one depicted in FIG. 1.3 and let us define the length  $L$ , the thickness  $t$  and the width  $w$  (thickness

and width are usually defined as the dimensions respectively parallel and orthogonal to the direction of bending).

The deflection of the beam is defined by the quantity  $u_z(x)$ , which describes the displacement in  $z$ -direction of the beam as a function of the distance from its base. Under the hypothesis of small deflection and of only lateral loads, the deflection follows the Euler-Bernoulli equation

$$\frac{d^2}{dx^2} \left( EI \frac{d^2 u(x)}{dx^2} \right) = q_z(x) \quad (1.10)$$

where  $q_z(x)$  is a distributed load (i.e. a force per unit length) acting along  $z$ ,  $E$  is the elastic modulus of the material and  $I$  is the second moment of area of the beam's cross section. For a beam oriented along  $x$  and loaded along  $z$ ,  $I$  is defined as

$$I = \iint_A z^2 dy dz \quad (1.11)$$

where the origin of the axis must be set in the centroid of the beams's cross section. For a beam of rectangular section as the one we are considering, the previous expression trivially simplifies into

$$I = \frac{wt^3}{12}. \quad (1.12)$$

Furthermore, for beams with constant section and large length-to-thickness ratios  $I$  can be considered constant and so is the product  $EI$  (also called *flexural rigidity* of the beam), therefore Eq. (1.10) simplifies to

$$EI \frac{d^4 u(x)}{dx^4} = q(x) \quad (1.13)$$

from which the actual bending of the beam can be easily computed alongside the corresponding mechanical stress on the structure.

In the case of a point-like force  $F$  acting at the extremity of the beam, the solution for the displacement  $u(x)$  is easily calculated as

$$u(x) = \frac{L}{2EI} x^2 \left( 1 - \frac{x}{3L} \right) F. \quad (1.14)$$

The maximum deflection of the beam is at  $x = L$  and is a linear function of the force, therefore an equivalent spring constant for the cantilever can be defined as

$$k_{\text{cant}} = \frac{3EI}{L^2} = \frac{Ewt^3}{4L^3} \quad (1.15)$$

such that  $u(L) = F/k_{\text{cant}}$ , which justifies the idealization of the cantilever as a mass-spring system.

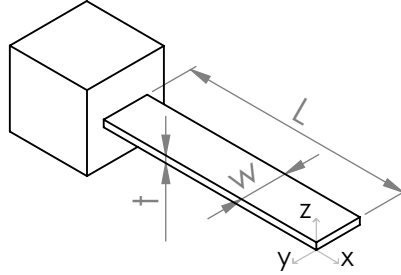


FIGURE 1.3: Rectangular cantilever beam with vertical deflection.

## 1.2.2 Dynamics

The Lagrangian of the system is

$$\begin{aligned}\mathcal{L} &= \frac{1}{2} \mu \left( \frac{\partial u}{\partial t} \right)^2 - \frac{1}{2} EI \left( \frac{\partial^2 u}{\partial x^2} \right)^2 + q(x)u(x, t) = \\ &= \frac{1}{2} \mu \dot{u}^2 - \frac{1}{2} EI u_{xx}^2 + qu = \mathcal{L}(t, u, \dot{u}, u_{xx})\end{aligned}\quad (1.16)$$

where  $\mu$  is the linear mass density (mass per unit length) of the beam,  $\dot{u}$  is the first time derivative of  $u$  and  $u_{xx}$  is the second  $x$ -derivative of  $u$ . The first term is clearly associated to the kinetic energy, the second to the elastic flexural potential, the third to the work of the distributed load. The generalized Euler-Lagrange equation for this form reads as

$$\frac{\partial \mathcal{L}}{\partial u} - \frac{\partial}{\partial t} \left( \frac{\partial \mathcal{L}}{\partial \dot{u}} \right) + \frac{\partial^2}{\partial x^2} \left( \frac{\partial \mathcal{L}}{\partial u_{xx}} \right) = 0. \quad (1.17)$$

The derivatives are trivial to compute and result in

$$\frac{\partial \mathcal{L}}{\partial u} = q; \quad \frac{\partial \mathcal{L}}{\partial \dot{u}} = \mu \dot{u}; \quad \frac{\partial \mathcal{L}}{\partial u_{xx}} = -EI u_{xx} \quad (1.18)$$

which plugged into Eq. (1.17) give

$$\frac{\partial^2}{\partial x^2} \left( EI \frac{\partial^2 u}{\partial x^2} \right) = -\mu \frac{\partial^2 u}{\partial t^2} + q. \quad (1.19)$$

which, in the static case, correctly simplifies into Eq. (1.10). Again, for a rectangular beam of constant cross section with large length-to-thickness ratio, the flexural rigidity  $EI$  is constant, therefore the final equation of motion of the beam reads as

$$EI \frac{\partial^4 u}{\partial x^4} = -\mu \frac{\partial^2 u}{\partial t^2} + q. \quad (1.20)$$

Let us now consider the case of free oscillations, where  $q = 0$ , and Eq. (1.20) is further simplified in

$$EI \frac{\partial^4 u}{\partial x^4} + \mu \frac{\partial^2 u}{\partial t^2} = 0. \quad (1.21)$$

Let us approach the solution through the Fourier decomposition and write  $u$  as

$$u(x, t) = \text{Re} [\hat{u}(x)e^{i\omega t}] \quad (1.22)$$

where  $\omega$  is the angular frequency of vibration. Then Eq. (1.21) simplifies into the ordinary differential equation

$$EI \frac{\partial^4 \hat{u}}{\partial x^4} - \mu \omega^2 \hat{u} = 0 \quad (1.23)$$

whose general solution is in the form

$$\hat{u} = A_1 \cosh(\beta x) + A_2 \sinh(\beta x) + A_3 \cos(\beta x) + A_4 \sin(\beta x) \quad (1.24)$$

where  $\beta = \sqrt[4]{\mu\omega^2/EI}$ . To determine the final solution we need to impose four boundary conditions. For a cantilever beam these are

$$\hat{u}|_{x=0} = 0; \quad \left. \frac{d\hat{u}}{dx} \right|_{x=0} = 0; \quad \left. \frac{d^2\hat{u}}{dx^2} \right|_{x=L} = 0; \quad \left. \frac{d^3\hat{u}}{dx^3} \right|_{x=L} = 0. \quad (1.25)$$

The first two conditions refer to the base of the beam being clamped, so that it cannot move from its position ( $\hat{u}(0) = 0$ ), and the surface must keep parallel to the base ( $\hat{u}_x(0) = 0$ ). The third and fourth imply that the free extremity of the beam is subjected to no bending moment and no shear force. Now, non trivial solutions of Eq. (1.24) exist only for  $\cosh(\beta_n L) \cos(\beta_n L) + 1 = 0$ . This equation needs to be solved numerically, and the first few roots are  $\beta_1 L = 1.875$ ,  $\beta_2 L = 4.694$ ,  $\beta_3 L = 7.855$ . Then by the definition of  $\beta$  we finally find our eigenfrequencies as

$$\omega_n = \beta_n^2 \sqrt{\frac{EI}{\mu}} \quad (1.26)$$

Writing  $\beta$  as a function of  $L$ , substituting  $I$  with its expression from Eq. (1.12), and expressing the linear density  $\mu$  as a function of the material density  $\mu = \rho A = \rho wt$ , the final formula for the first eigenfrequency of the cantilever is

$$f_1 = \frac{1.015}{2\pi} \frac{t}{L^2} \sqrt{\frac{E}{\rho}} \quad (1.27)$$

The theory we briefly discussed here allows an immediate understanding of the problem and provides a simple formula for the eigenfrequencies and the analytical shape of the eigenmodes. We should emphasize, however, that it is intrinsically limited by a series of approximations that are related to the simplicity of the geometry considered. With more complex geometries, retrieving analytical solutions quickly becomes impractical. Furthermore, even in the simple rectangular beam case, it is not immediate to retrieve more complex information as, for instance, the stress distribution in the region close to the base of the beam, or the shape and frequencies of the torsional modes. It is therefore greatly convenient to be equipped with some more sophisticated simulation software, as will be shown later in this work.

## 1.3 Quality factor of micro-cantilevers

### 1.3.1 Validity of the 1D harmonic oscillator model

The Q-factor of cantilevers, or generally their frequency response, has been the object of extensive theoretical and experimental investigation for decades. We should emphasize that the theory we presented in Sect. 1.2.2 retrieves eigenfrequencies and eigenmodes, but does not account for any damping mechanisms, so nothing can be inferred about the Q-factor. Some basic, general concepts can be inferred, instead, by going back to the harmonic oscillator model, specifically referring to Eq. (1.7). The Q-factor was proved to be inversely proportional to the damping coefficient  $\zeta$ , whose definition was given in Eq. (1.3) as  $\zeta = \mu/2m\omega_0$ . The damping coefficient is proportional to viscous

friction and inversely proportional to mass and frequency. Viscous friction is absolutely not trivial to calculate (see next section) and depends on the geometry of the beam, but it has been shown to be mostly connected to the cross-sectional area of the beam with respect to the direction of bending (that would be  $A = wL$  in FIG. 1.3). It is obvious to see, therefore, that a thicker cantilever, which has at the same time a larger mass and a larger resonant frequency, as by Eq. (1.27), will have a smaller damping coefficient, therefore a *higher Q-factor*. Similar reasoning can be done for shorter cantilevers, and the conclusion is a general rule of thumb that, when the main dissipation mechanism is external viscous friction, *stiffer resonators have higher Q-factors*. The problem is that, in many applications, stiff cantilevers are impractical. The technological challenge is, therefore, obtaining cantilevers with high Q-factor but low resonant frequency.

The real problem of damping is, however, much more complicated than that. For instance, it is well known that, when damping increases, the resonant frequency of the cantilever measurably *decreases*, as clearly shown in [11] and [12]. Eq. (1.9) shows indeed that  $\omega_{\max}$  decreases when  $\zeta$  increases, but it does not fully account for this effect. Furthermore, we will later show that if the theory presented in Sect. 1.1 is slightly modified to model an actuation "by the base" of the cantilever (see Sect. 6.3.1), the equivalent of Eq. (1.9) becomes Eq. (6.7), which predicts an *increase* of the resonant frequency that is contradicted by all observations. This clearly suggests that the real drag force acting on the cantilever cannot be modelled by just a simple velocity-proportional term as introduced in Eq. (1.1). More accurate models, indeed, introduce also terms proportional to acceleration, which happen to be dominant for viscous fluids like air. The rigorous model proposed in [5] introduces the two terms into the real Lagrangian of the system presented in Eq. (1.16) and re-computes the dynamics from there. In our harmonic oscillator model, we can still account for the phenomenon by adding to Eq. (1.1) a drag force that is proportional to acceleration, obtaining

$$m\ddot{x} = -\gamma\dot{x} - kx + F - \gamma_2\ddot{x}. \quad (1.28)$$

Rearranging the terms, it is evident that the system becomes equivalent to an harmonic oscillator with an equivalent mass

$$m_{\text{eq}} = m + \gamma_2 \quad (1.29)$$

so that the resonant frequency becomes  $\omega_0 = \sqrt{k/m_{\text{eq}}} = \sqrt{k/(m + \gamma_2)}$ , which *decreases* as the damping increases. The physical explanation for this phenomenon, as reported by Sandberg *et al* [12], is that the oscillation of the cantilever causes the surrounding gas molecules to move alongside with the beam, therefore the effective mass of the beam will be larger as the density of the gas (i.e. the pressure) increases.

We should finally emphasize that the harmonic oscillator model accounts for a single resonant frequency, while a real cantilever has several eigenmodes, therefore several resonant frequencies. However, it has always been experimentally evident, and it was rigorously demonstrated by Sader [13], that the rigorous frequency response of a cantilever in low-damping regime is approximated by that of an harmonic oscillator in the proximity of resonance peaks, so our model is nonetheless appropriate and the quality factor can be analytically defined as in Eq. (1.6). It is evident, however, that the damping term  $\zeta$  represents, in that



case, a sum of several damping mechanisms and cannot be directly related to the simplistic velocity-proportional definition presented in Eq. (1.3).

### 1.3.2 Modelling friction

Several theoretical approaches have been proposed to provide some *a priori* prediction of the Q-factor of cantilevers. The aim of such models is to provide design rules and guidelines to obtain the best performance from a cantilever out of a given set of conditions. Literature is neither univocal nor conclusive on this matter, but there seems to be a general agreement on the regimes subdivision first proposed by Newell [14]. Newell identified an *intrinsic*, a *molecular* and a *viscous* region, each of them having their own dominant damping mechanisms. Their definition depends on pressure, but the limits of each regime are not sharp nor immediately retrievable.

In the intrinsic region, pressure is so low that air damping becomes negligible compared to intrinsic loss mechanisms such as the internal frictions and viscosity of the material. In this regime, usually associated to high vacuum (meaning pressures in the order of 1 Pa or less), quality factors as high as  $10^4$  or  $10^5$  have been demonstrated [15, 16]. Yasumura *et al* [15] offer good insights into the effects of different materials, coatings, pressure and geometry on the quality factors in this region. A predictive model, however, is still missing.

In the molecular region, which Blom *et al* [5] associated to pressures in the range of 1 to  $10^2$  Pa, the damping caused by the gas dominates over that of the intrinsic losses, but the gas is sufficiently rarefied to allow a modelling of the damping as the effect of single collisions of gas molecules with the sides of the beam. The problem can be therefore treated through the kinetic theory of gases, and Blom derived for the Q-factor

$$Q_{\text{molecular}} = \frac{\beta_n^2}{k_m p} \left( \frac{t}{L} \right)^2 \sqrt{\frac{\rho E}{12}} \quad (1.30)$$

where  $k_m = \sqrt{32M/9\pi RT}$  with  $M$  the mass of the molecules,  $R$  the gas constant,  $T$  the absolute temperature. In this regime the quality factor is inversely proportional to pressure.

The region of greatest interest is the viscous regime since, being associated to pressures higher than  $10^3$  Pa, it includes operation at atmospheric pressure, which is the most common practical scenario. In this region, cantilevers usually exhibit Q-factors [17] in the range of 100 to 1000, with few exceptions. In [18], for instance, a resonator with  $Q > 1400$  is reported, but such high Q-factor is achieved at the expense of an extremely high resonant frequency (60 MHz) associated to the in-plane vibration mode.

In the viscous region, air must be treated as a viscous fluid and its interaction with the cantilever must be calculated through fluid dynamics theory, which makes the prediction of the frequency response extremely challenging from a modelling perspective. Numerous approximated solutions have been proposed, and we shall here review a few of them to later discuss them based on our experimental results, presented in the last chapter of this work. A first formula was proposed by Newell [14] and reads as

$$Q_{\text{Newell}} = \frac{1}{24} \frac{wt^2}{L^2} \frac{\sqrt{E\rho}}{\gamma_{\text{air}}} \quad (1.31)$$

where  $\gamma_{\text{air}}$  is the viscosity of air and  $\rho$  the density of the material.

Because a sphere oscillating in a fluid is one of the very few problems that allow analytical solutions of the Navier-Stokes equations for the drag force, the most commonly employed formula for the calculation of the Q-factor approximates the cantilever as an oscillating sphere of radius  $R$ . By such a model, Blom [5] derives

$$Q_{\text{Blom}} = \frac{\beta_n^2 \omega t^2 \sqrt{E\rho/12}}{6\pi\gamma_{\text{air}}RL(1 + R/\delta)} \quad (1.32)$$

where  $\delta = \sqrt{2\gamma_{\text{air}}/\rho_{\text{air}}\omega}$ . This is clearly an approximation where  $R$  is not known *a priori* and could depend, in principle, not only on the geometry of the cantilever but also on all other parameters. For instance,  $R$  might not be the same for two different vibration modes of the same cantilever. Many authors have tried to connect  $R$  to the actual dimensions of the beam [4]. Ikehara *et al* [17], for instance, have shown good agreement with their experiments on a large set of cantilevers assuming an equivalent cross-section approximation as  $R_{\text{Ikehara}} = \sqrt{wL/\pi}$  (the cantilever and the sphere have the same cross-sectional area). This result, however, contrasts with the results by Blom and Bergaud [4, 5], who have found instead a practically linear dependence of  $R$  with the length of the beam  $L$ . The connection between  $R$  and the actual geometry, therefore, remains largely elusive, so that in most cases  $R$  needs to be retrieved by fitting the formula to the experimental results. It is clear, therefore, that the sphere model does not strictly provide an *a priori* prediction of the Q-factor, but rather some general guidelines.

Hosaka and Itao [19] have proposed a refined version of the sphere model by idealizing the cantilever as a string of independently moving spheres with radius  $R = w/2$ , and have found

$$Q_{\text{Hosaka}} = \frac{2qtw^2\omega_n}{3\pi\gamma_{\text{air}}w + \frac{3}{4}\pi w^2\sqrt{2\rho_{\text{air}}\omega_n}}. \quad (1.33)$$

Lee *et al* [20] have compared the formulas by Newell and Hosaka and have proposed an empirical correction based on their experimental results that reads as

$$Q_{\text{Lee}} = \frac{(0.24qtwL)\omega_n}{[0.69(3\pi\gamma_{\text{air}}w) + 0.33(\frac{3}{4}\pi w^2\sqrt{2\rho_{\text{air}}\omega_n})](\frac{L}{w})(\frac{w}{L})^{0.38}} \quad (1.34)$$

To conclude, we ought to briefly discuss the only model that provides an analytical solution to the actual problem of a rectangular cross-section cantilever immersed in a viscous fluid, i.e. the model presented by Sader in a well-known article of 1998 [13]. The model is based on the following hypothesis:

1. the beam has uniform cross section over its entire length;
2. the length of the beam is much larger than the width ( $L \gg w$ );
3. the beam is made of an isotropic linear elastic material and the intrinsic losses are negligible;
4. the amplitude of vibration is much smaller than any other dimension of the beam.

In the limit of small dissipative effects, Sader finds

$$Q_{\text{Sader}} = \frac{\frac{4\mu}{\pi Q w^2} + \Gamma_r(\omega_n)}{\Gamma_i(\omega_n)} \quad (1.35)$$

where  $\Gamma(\omega) = \Gamma_r(\omega) + i\Gamma_i(\omega)$  is a complex quantity called *hydrodynamic function*. The hydrodynamic function for a circular beam  $\Gamma_{\text{circ}}(\omega)$  has an analytical expression. The hydrodynamic function for a rectangular beam  $\Gamma_{\text{rect}}(\omega)$  can be computed numerically, but the author provides instead an empirical correction factor  $\Omega(\omega)$  that, with the additional hypothesis of  $t \ll w$  (or *infinitely thin cantilever*), allows to express the rectangular one as a function of the circular one:  $\Gamma_{\text{rect}}(\omega) = \Omega(\omega)\Gamma_{\text{circ}}(\omega)$ . The resulting expression can be found in the original paper [13] and is extremely complicated. In fact, even after these results were published, most authors kept working on the approximated models, such as the sphere.

We should point out that all the models presented strictly deal only with the fundamental mode of oscillation, although some authors have tried to extend them to higher modes. Sader's model is supposed by the author to work on the first few modes, and Bergaud [4] has shown that it appears to be reliable only up to the second. Exploring high order modes is of large interest because, as pointed out in [21], the sensing performances of longer cantilevers driven at higher modes are the same as those of shorter cantilevers driven at the fundamental mode, and longer cantilevers are often more convenient and easier to fabricate reliably. However, to the best of our knowledge, no model has been proposed yet that accounts for a truly multimodal behaviour.

Finally, we must emphasize that all the models we considered are strictly referred to cantilevers in completely open space, meaning that the surrounding air is fully free to move and any other wall is very far away from the beam as compared to its dimensions.

## 1.4 State of the art and applications

### 1.4.1 Microfabrication

Microfabrication of MEMS has been a subject of extensive research in the past decades. Although a wide variety of substrates and thin films can be used to fabricate MEMS and microcantilever devices, the most commonly employed is single crystal silicon. This is due to the fact that most MEMS microfabrication techniques rely on the same approaches developed for standard silicon-based microelectronics [8]. These usually involve deposition, photolithographic patterning and etching steps where other materials such as silicon oxide and silicon nitride are often employed to create structural or sacrificial layers which allow to create highly complex geometries, thanks to their different response to different etchants. A common fabrication scheme for cantilevers is shown in FIG. 1.4. Despite the predominance of silicon-based microtechnology, a plethora of other materials are employed with similar techniques. Some polymers, for instance, seem promising for their chemical resistance and biocompatibility [22].

The choice of material, design and fabrication method is ultimately dictated by the operation mode of the sensor, the readout method, and the application to

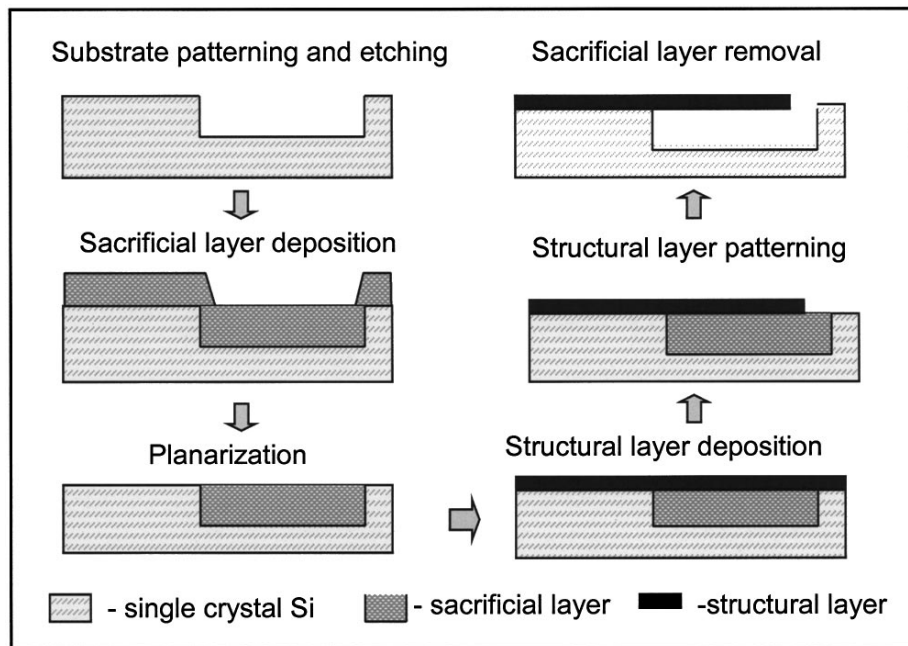


FIGURE 1.4: General fabrication scheme for silicon microcantilevers. In this example, silicon oxide is used as sacrificial layer and silicon nitride is used a structural layer. Image from [8].

which the cantilever is directed. As an example, a 50 to 150 nm metal layer is often deposited on the top surface of the cantilever to provide the reflectivity needed for the optical readout (see Sect. 1.4.2). Metal layers are also required for charge or tunnelling effect readout and, because of their high thermal expansion coefficient, they can be engineered to cause a bending of the cantilever at different temperatures, thus effectively realizing temperature sensors. Other types of readout require deposition of piezoelectric or piezoresistive layers [8].

Among the greatest advantages of silicon-based photolithographic techniques are the possibility of borrowing great expertise and an entire production apparatus from the electronics industry, and the possibility of fabricating in large batches while achieving sub-micrometric accuracy with high repeatability. This has made low-cost AFM cantilevers largely available, and most structural and geometrical requirements for MEMS cantilever transducers are similar to those applicable in AFM. In analogy to AFM cantilevers, MEMS cantilever transducers have typical lengths in the range of 100 to 500  $\mu\text{m}$  and thicknesses in the range of 0.5 to 5  $\mu\text{m}$  (see FIG.

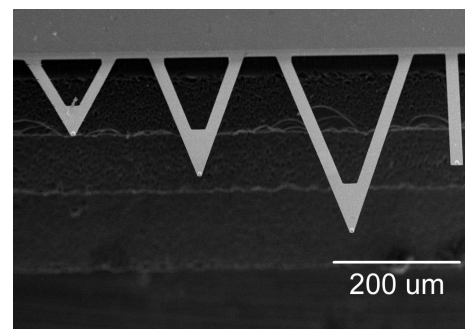


FIGURE 1.5: Example of commercial AFM cantilevers. The triangular shapes are engineered to minimize torsional effects.

1.5), corresponding to spring constants in the order of 1 to  $0.01 \text{ N m}^{-1}$ .

The main drawbacks of photolithographic techniques include the requirement of multi-step processing, the need of clean room facilities and the expensive production of masks. Even more importantly, lithographic techniques are inherently bound to surfaces, meaning that they have little or no access to the bulk of the sample, which is instead achievable through different techniques such as laser writing.

### 1.4.2 Readout schemes

The operation of any cantilever sensor requires the ability to monitor the deflection of the beam in real-time with at least nanometre accuracy, so the readout method is a fundamental (and often limiting) part of the performance of the sensors. Depending on the specific application and operation environment, several readout schemes have been proposed.

**Optical methods.** The most commonly employed scheme is, again, directly inherited from AFM, and is the so called *optical lever* method (see FIG. 1.6), originally proposed by Meyer and Amer [23]. A laser beam is focused on the top surface of the cantilever, and the angular deflection of the cantilever is amplified by a displacement of the laser beam, detected by a PSD (*position-sensitive detector*). The method allows to measure extremely small displacements, and measurements of up to  $10^{-14} \text{ m}$  have been reported. The main limitations of this method are the complex alignment procedure, the fact that it can only work on cantilevers that have a reflective surface of at least  $10 \times 10 \mu\text{m}$  (so, for instance, it is not applicable to nano-cantilevers), the fact that it can only be operated in low opacity and low turbidity media, and an intrinsic bandwidth limitation due to the PSD, whose bandwidth is typically in the order of several kilohertz. When the bandwidth requirements become more critical, different methods have been proposed based on avalanche photodiodes or interferometric techniques [8].

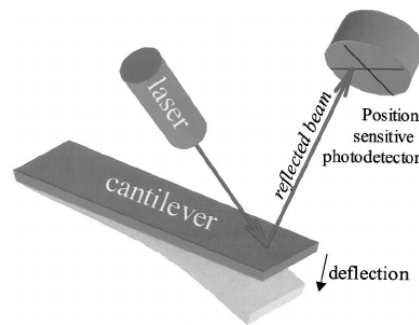


FIGURE 1.6: Schematic view of the optical lever method.

**Piezoresistive and piezoelectric methods.** Because of the aforementioned limitations of optical techniques, *integrated* readout methods are strongly appealing, as they are provided by the cantilever itself and not by some external system. Piezoresistive readout is based on the change in resistance of a material due to the mechanical stress associated to the bending of the cantilever. Excellent piezoresistivity has been shown with doped single-crystal silicon and doped polysilicon. The resistance is usually measured through a DC-biased Wheatstone bridge, which also constitutes the main drawback of the technique, as a current flow implies heat dissipation that can cause temperature instability and piezoresistance changes. Piezoelectric readout methods can overcome this issue

and have also been shown to be able to produce self-exciting cantilevers. However, they require piezoelectric layers with a thickness well above the optimal operating region of the cantilever. Furthermore both of these techniques require electrical connections to the cantilever, which can be impractical to implement in many cases.

**Capacitance and tunnelling methods.** Capacitance readout is based on measuring the change in capacitance between a conductor layer on the cantilever and another fixed conductor that is separated from the cantilever by a small gap. Change in gap due to oscillations of the cantilever result in a change of capacitance. While this method is highly integratable in standard CMOS technology, it suffers from parasitic effects due to variations of the dielectric constant of the medium.

When a conducting tip and the cantilever are separated by a subnanometre gap, tunneling current can occur that is very strongly dependant on the distance between the two, hence on the deflection of the cantilever. This was actually the first readout scheme proposed by the inventors of AFM [6], where the idea of tunnelling current measurement originated from their previous invention of the STM (scanning tunnelling microscopy).

**Integrated optical readout.** From the present discussion, it clearly emerges that having an integrated *optical* readout scheme, combining the convenience of integrated methods with the accuracy and non-invasive nature of optical methods, could be greatly beneficial for cantilever sensors. One would need to find a way to couple some light into the very structure of the cantilever, and engineer it in such a way that the movement of the cantilever causes some measurable modification to the light path. To the best of our knowledge, only one implementation of such a scheme has been proposed [24, 25], of which we

here report the schematics in FIG. 1.7. The idea is to have the cantilever itself acting as a waveguide, which is possible because of the positive index contrast with respect to air. An input and an output waveguide are then coupled to the cantilever, and the movement of the cantilever causes a misalignment with the output waveguide that results in a modulation of the transmitted intensity. Despite the simplicity of the concept, the realization of the final device, as explained by Dominguez *et al* [24], is extremely complex, especially having to deal with the fact that the cantilever is made of  $\text{SiO}_2$ , which has positive index contrast with air but negative contrast with the Si substrate, therefore a  $\text{Si}_3\text{N}_4$  junction had to be fabricated so that the light could be evanescently coupled into the cantilever. As pointed out by the authors, the resolution limit of the scheme is ultimately determined by the noise of the measurement, which determines how small a transmission change can be detected, therefore how

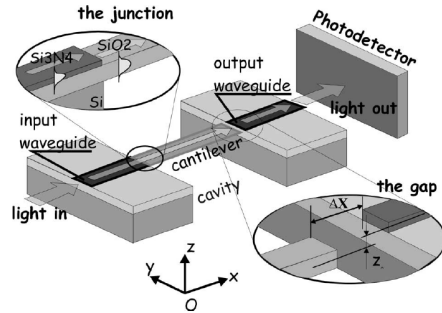


FIGURE 1.7: Schematics of the device proposed by Zinoviev *et al* [24].

small a displacement of the cantilever can be sensed. In any case, the signal to noise ratio improves if higher intensities are transmitted through the device. Yet, despite the very high insertion losses and the consequent small output intensity, by operating the cantilever around its resonance frequency and measuring its response with a spectrum analyser, they were able to demonstrate an impressive resolution of 0.04 nm.

### 1.4.3 AM-AFM and force sensing

The applications of cantilevers as sensors are extremely wide and diverse. A comprehensive review is beyond the scope of this work, but a fairly extensive one can be found in [8]. We shall here present, instead, a single application – arguably the most important – which, despite its specificities, exemplifies concepts, issues and approaches that are common to almost all others.

As already mentioned, the theoretical and experimental interest for cantilevers exploded after the invention of Atomic Force Microscopy (AFM). In this technique, a very sharp tip is fabricated at the free extremity of the beam, and the minuscule force acting between the tip and the surface of the sample translates into a measurable change of its mechanical properties. Because such force is very strongly dependent on the distance between the tip and the surface, the measure becomes extremely sensitive to surface topology, hence its great interest for surface science. In static mode, the measurement consists in monitoring the deflection of the cantilever as a given area of the sample is scanned. The most common implementation of AFM, however, is in amplitude-modulation (AM) mode, where the cantilever is operated around its resonance frequency. The problem can be modelled through the harmonic oscillator theory by introducing an additional external force  $F(z)$ , where  $z$  is the direction orthogonal to the surface.  $F(z)$  can always be expanded to the first order in the form  $F(z) = F_0 + [dF(z)/dz]z$ . Plugging it back into Eq. (1.1), we can clearly see that this is equivalent to having the spring constant of the oscillator shifted as  $k_{\text{eff}} = k - dF(z)/dz$ , which also implies a shift of the resonant frequency to  $\omega'_0 = \sqrt{k_{\text{eff}}/m}$ . The beam is driven at constant frequency, therefore a shift of the resonant frequency will translate into a change in the amplitude of the oscillation, as shown in FIG. 1.8. While the *horizontal* resolution of the microscope entirely depends on the sharpness of the tip, the *vertical* resolution depends on how small a frequency shift can be detected. The sharper the resonant peak, the greater the amplitude variation will be. It easy to demonstrate that indeed, working in the steepest part of the

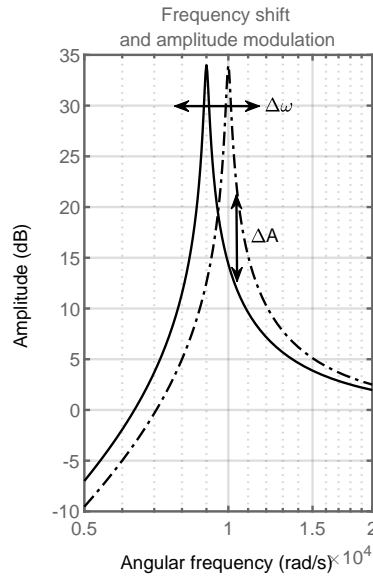


FIGURE 1.8: Amplitude modulation due to frequency shift in AM-AFM.

curve, the amplitude shift is given by  $\Delta A = Q (2A_0 dF/dz) / (3\sqrt{3}k)$  where  $Q$  is the quality factor of the cantilever [7]. We can see, once more, why it is highly desirable to have a cantilever with large  $Q$ -factor but low spring constant  $k$ : a larger  $\Delta A$  ultimately allows to measure smaller forces.

From this brief discussion, one could assume that if an arbitrarily small  $\Delta A$  can be measured, then an arbitrarily small force can be detected. This is untrue, because an even more fundamental limit comes into play, that is thermomechanical noise. Its presence is due to the very fact that the cantilever is in thermal equilibrium with its environment, and there exist a coupling between the two which will cause the mechanical energy of the beam to leak into the environment, but also some random excitation from the many microscopic degrees of freedom of the heat bath to the cantilever. This is a consequence of the *fluctuation-dissipation theorem* of statistical mechanics. The coupling between cantilever and environment is proportional to dissipation losses, which are inversely proportional to  $Q$ . By the equipartition theorem and the assumption that the noise spectrum is white, it straightforward to demonstrate [15] that the minimum theoretically detectable force is  $F_{\min} = \sqrt{4kk_B T B / \omega_0 Q}$ , which leads to the same conclusions as before regarding the need of high- $Q$  and low- $k$  cantilevers.



## Chapter 2

# Femtosecond Laser Micromachining

*Femtosecond Laser Micromachining* (or *FLM*) is a general definition that identifies the use of femtosecond lasers to produce permanent modifications on materials with micro- or sub-micrometer resolution. The technique was first demonstrated in 1994, when a femtosecond laser was used to produce micrometer-sized features on silica and silver surfaces [26, 27], and has now become widespread as femtosecond lasers have become more available and reliable. Its applications are extremely wide, ranging from direct writing techniques such as waveguide writing, 2-photon polymerization [28], material processing and data storage [29, 30], to biological nanosurgery [31] and microfluidic channels for on-chip biological analysis [32].

For the purpose of this work, we shall present a brief review of FLM on transparent materials [33], mainly referring to the micromachining of glass substrates. We shall start by describing the physical principles and the common operation parameters of the technique, and we shall then give some more details about waveguide writing and microstructuring techniques on glass.

## 2.1 Physical principles

### 2.1.1 Nonlinear absorption in dielectrics

A dielectric material is *transparent* to light of a given frequency  $\nu$  if it has an energy gap  $E_g$  between valance and conduction band that is greater than the photon energy  $h\nu$ . This implies that no first order absorption can occur. At high intensities, however, absorption can take place through nonlinear phenomena such as multiphoton, tunnelling and avalanche ionization [34, 35]. Multiphoton absorption occurs when multiple photons are simultaneously absorbed, so that the sum of their energy exceeds  $E_g$ . Tunnelling occurs when the electric field of the laser beam is strong enough to lower the Coulomb potential barrier and alter the band structure in such a way to enable an electron to tunnel from the valence to the conduction band. Avalanche ionization occurs when an electron that is already in the conduction band is accelerated to an energy greater than  $E_c + E_g$  (where  $E_c$  is the bottom energy of the conduction band) so that, when

hitting an electron in the valence band, it can transfer energy high enough for the second electron to jump to the conduction band as well. Then the second electron is also accelerated and is able to excite new electrons, generating an avalanche process that grows exponentially and lasts for the whole duration of the laser pulse.

Pulses longer than several picoseconds cannot achieve peak intensities high enough to trigger multiphoton and tunnelling processes, so only avalanche ionization can take place. The avalanche needs to start from an initial seed of free electrons, which in an insulator are due to structural defects of the material. Since their number is subject to large fluctuations, this process is erratic and poorly reproducible. On the other hand, femtosecond pulses can achieve extremely high intensities. For instance, a 100 fs pulse of 1  $\mu\text{J}$  energy focused on a 200  $\mu\text{m}^2$  area corresponds to a peak intensity of  $5 \times 10^{20} \text{ W m}^{-2}$ . At such high intensities, the local electric field is comparable with the binding electric field of valence electrons [33], therefore multiphoton and tunnelling processes can both take place and create free electrons which *then* start the avalanche process, leading to an overall phenomenon known as *optical breakdown* of the material. In this case the process is completely deterministic, as no seed electrons in conduction band are needed. Depending on the irradiation parameters, it can lead to permanent modifications of the material. Because the physical principles are substantially the same in any dielectric, the technique is applicable to almost any transparent material [33], although with significant differences in the irradiation parameters and the modifications obtained.

### 2.1.2 Space localization and bulk micromachining

The absence of linear absorption is the very reason why transparent materials are highly appealing for femtosecond laser micromachining. Indeed, the strongly nonlinear nature of the process causes it to occur *only* where the intensity is high enough, substantially behaving as a threshold process. In practice, when the laser beam is strongly focused in a point inside the bulk of the material, the threshold is reached only in a narrow region around the focal point, where light is confined to a small area and the intensity is therefore very high (see FIG. 2.1). As a result, it is possible to modify the bulk of the material without affecting its surface, which is a major advantage with respect to standard micromachining techniques like the photolithographic processes described in Sect. 1.4.1. Furthermore, as the relative position of the focal point and the sample is moved, microstructuring with almost arbitrary geometry becomes possible. Notice, in particular, that, as opposed to photolithography, this technique is intrinsically 3D-capable, since the focal point can be moved also in the vertical direction. Finally, if the laser beam is focused deep under the surface, small imperfections of the surface like defects or dust grains have little or no effect on the focal region, therefore the technique is fairly solid with respect to surface quality and does not require clean room facilities, which is a major operational advantage.

### 2.1.3 Relevant parameters

While the absorption process of femtosecond laser pulses in dielectrics is well assessed, the mechanisms through which it leads to permanent modifications of

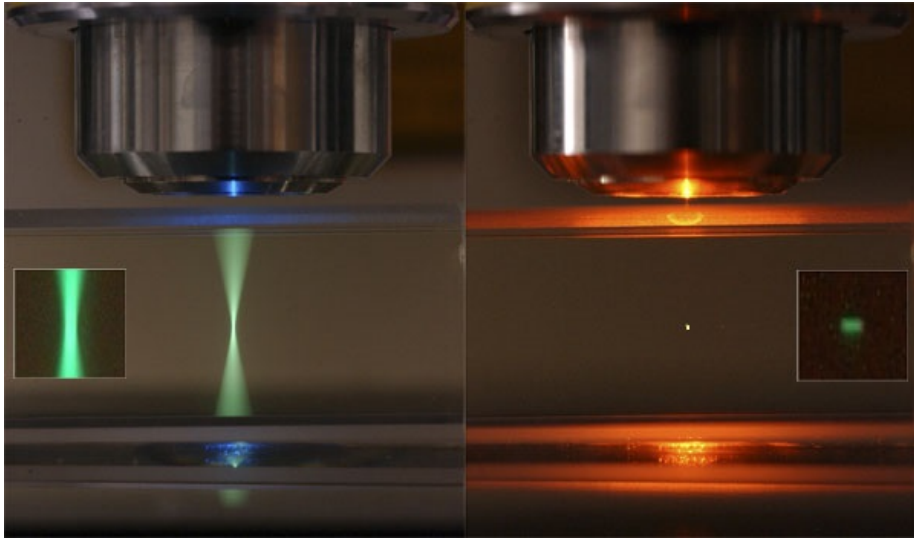


FIGURE 2.1: Comparison between linear (left) and nonlinear (right) absorption processes. Nonlinear absorption is very strictly confined around the focal point of the objective, while linear absorption occurs all along the path of the beam. Particularly notice that the nonlinear process does not involve any interaction with the surface of the sample. Image from UC Berkeley (<http://mcb.berkeley.edu/labs2/robey/content/2-photon-imaging>).

the material is not yet fully understood. In fact, the nature of such modification *does* strongly depend on the type of material, and it is also highly susceptible to small changes of the irradiation parameters, namely the pulse length and energy, the numerical aperture of the focusing objective, the repetition rate, and the writing speed. What seems to be evident is that the modification is the result of a complex interaction between the laser pulse and different excitation and relaxation processes, some of which take place with different time scales. In FIG. 2.2 some of the most relevant processes with their relative time scale are reported.

If the energy transfer from the laser pulse to the material was caused solely by multiphoton or tunnelling absorption, the intensity threshold  $I_{th}$  to produce permanent modifications should have a very strong dependence on the energy gap  $E_g$ . As a matter of fact,  $E_g$  has little effect on  $I_{th}$ , which indicates the importance of avalanche ionization for creating the damage: multiphoton absorption creates the initial seed, but the main structural modification of the material is due to the dynamics of avalanche electrons. What is most relevant, instead, on the type of damage to the material is the pulse energy  $E_p$ . Values of  $E_p$  just above the damage threshold lead to a change in refractive index of the material, being therefore the most commonly employed region for the fabrication of optical waveguides and photonic devices. Higher values of  $E_p$  lead to the creation of a high-energy plasma of free electrons that causes catastrophic damage and formation of voids [36].

The numerical aperture (NA) of the focusing objective is also important in determining the shape of the affected region. A minimum theoretical numerical aperture is necessary to reach  $I_{th}$ , but in practice higher NAs have to be used to limit the effects of different nonlinear phenomena like self-focusing and white

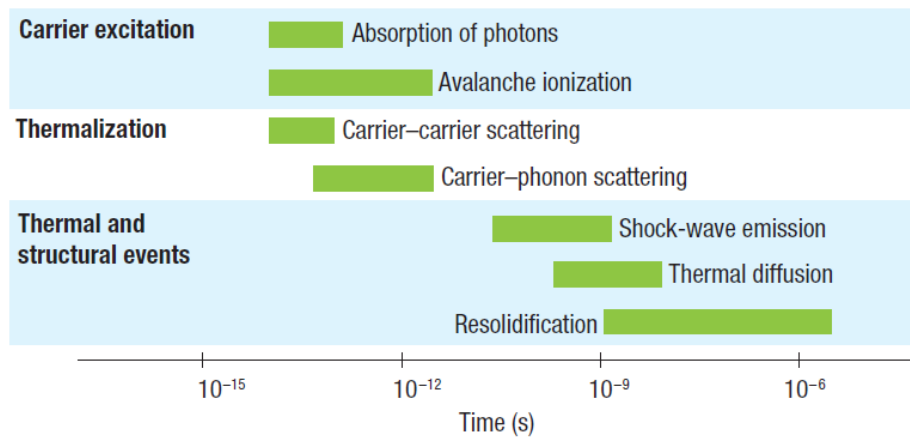


FIGURE 2.2: Time scale comparison of the most relevant excitation and relaxation mechanisms involved in the interaction between dielectric materials and ultrashort pulses. Image from [33].

light generation [37] which reduce the repeatability of the technique. For NAs close to or larger than unity, the focusing is extremely tight, so that micromachining can be accomplished with energy pulses as low as few nanojoules. In general, numerical apertures higher than 0.6 yield small, almost spherically symmetric features, while smaller NAs produce larger and asymmetric structures. As a downside, objectives with large NAs have very short working distances, which limits their range of operation in the vertical direction.

## 2.2 Femtosecond laser waveguide writing

### 2.2.1 Operational principles

Waveguide writing was one of the first demonstrations [38, 39] of the capabilities of FLM for photonic applications. As mentioned, the physical mechanisms that lead to a local increase of the refractive index of glass (hence the guiding effect) after the exposure to femtosecond pulses are still not fully understood [34]. Several mechanisms have indeed been proposed to account for such phenomenon, including colour centres formation [40], thermal modifications due to melting and rapid solidification [41, 42] and direct photostructural changes (i.e. rearrangements of the chemical bonds network) [43]. In practical cases all mechanisms play a role and their contributions are difficult to disentangle, so that the optimization of the writing parameters is often largely empirical.

In addition to all the parameters mentioned in the last paragraph, waveguide writing has an intrinsic, fundamental dependence on the repetition rate and on the writing speed. In fact, depending on the repetition rate, the operation can be roughly categorized in either *low frequency* or *high frequency* regime. In low frequency regime the modification is the result of the interaction with the single pulses [44], whereas in high frequency regime the spatial and temporal distance between successive pulses are shorter than the thermalization typical length and time [45, 46], therefore thermal cumulative effects take place. Since the

thermal relaxation time is typically in the order of  $1\ \mu\text{s}$  (see FIG. 2.2), thermal effects start to take place with repetition rates in the order of 1 MHz.

Waveguides of interest for photonic circuits are typically written by moving the sample orthogonally with respect to the direction of the beam, i.e. in *transversal* configuration (see FIG. 2.3). Waveguides can also be written in *longitudinal* configuration, i.e. by moving the sample parallel to the direction of the beam. This type of waveguides show a perfectly symmetric profile, but are limited in length by the working distance of the objective. On the contrary, waveguides written orthogonally can have arbitrary length, but show strongly asymmetric profiles caused by the difference between the focal diameter (which determines the horizontal dimension) and the confocal parameter (usually much greater, which determines the vertical dimension). This can lead to undesirable asymmetric mode shapes. The problem is overcome in low frequency regime by astigmatic beam shaping techniques [48] that yield a more symmetric focal region, and in high frequency regime is largely tamed by the isotropic nature of heat diffusion, which by itself leads to much more symmetric profiles (see for instance [44]). Recently, a two-step process involving waveguide writing and successive thermal annealing of the sample has been shown to provide waveguides with very low losses, very low birefringence and a highly symmetric guided single mode [49, 50].

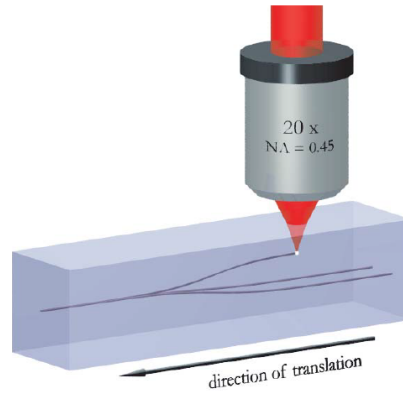


**FIGURE 2.3:** Writing of waveguides in transversal mode. In detail, the image represents a 1 to 3 power splitter. Notice the 3D geometry of the device. Image from [47].

### 2.2.2 Applications

Femtosecond laser waveguide writing has been applied to the realization of both active and passive devices. Active devices include active waveguides and amplifiers, as well as waveguide lasers [34]. Passive devices are particularly appealing for many other applications, as they can provide high quality integrated photonic circuits that can yield complex optical functions on-chip, allowing for very low cost, space saving devices that, as an obvious side benefit, do not suffer from the misalignment and mechanical vibration issues of an equivalent table-top setup. The complexity of such on-chip photonic circuits has increased over the years as laser sources and fabrication techniques have become more reliable. The fabricated devices quickly escalated from simple Y-splitters [47, 51–55] to directional couplers [56–61] to Mach-Zender interferometers [57, 62]. Nowadays, by cascading several of these fundamental elements and by exploiting the 3D capabilities of the technique, circuits of very high complexity can be produced, as shown in FIG. 2.4A and FIG. 2.4B. One of the applications for which they have become increasingly appealing is quantum photonics, where low losses, solid alignment and mechanical noise rejection are of extreme importance. These devices have been able to demonstrate several photon-based quantum information protocols [63–67].

One of the current frontiers of integrated photonic circuits is the fabrication of reconfigurable devices. While the first proof of concept [62], based on electro-optic effect in fused silica, needed to apply a 400 V bias to obtain a mere  $20^\circ$  phase shift, Flamini *et al* [68] have recently demonstrated a thermal phase-shifting technique where gold resistances are built on top of the chip and used as local heaters, as shown in FIG. 2.4C. The phase-shifting is caused by thermo-optic effect, which changes the refractive index of the waveguide, and allows a full configurability of the circuit as well as fine tuning of the phases between multiple arms of the interferometers. The downside of thermo-optic phase shifting are heat dissipation and cross-talk between heaters, as well as forcing the waveguides to be written rather close to the surface. New phase-shifting techniques, for instance based on strain-optic effect [69], are now under investigation and represent an open field of research.

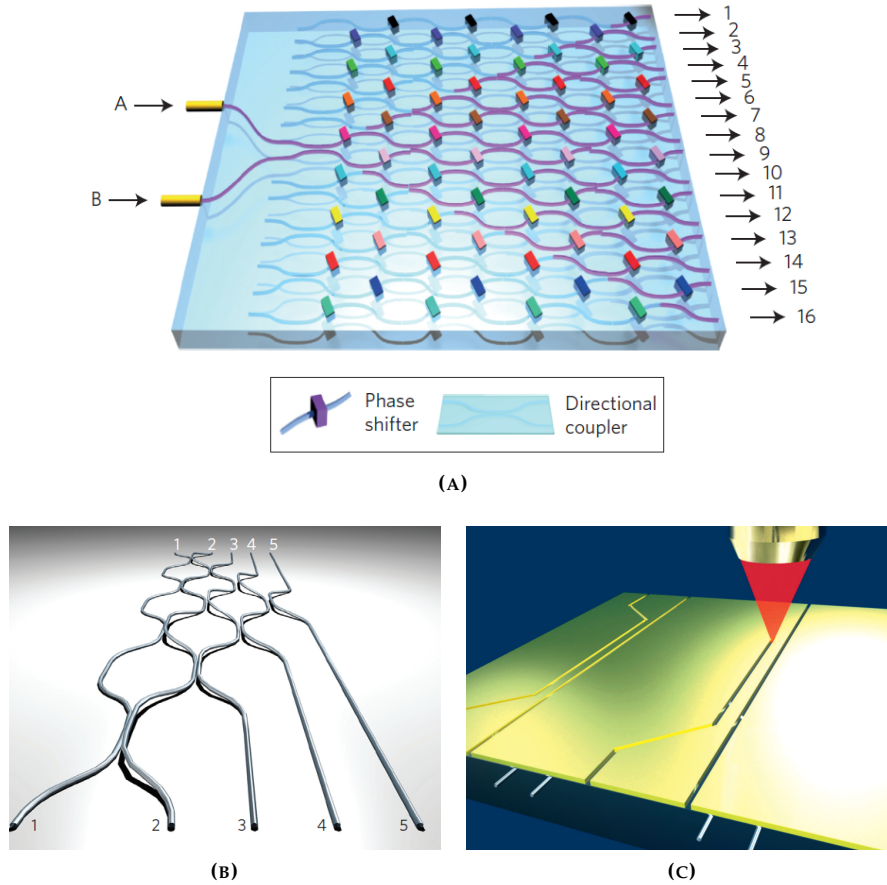


FIGURE 2.4: Examples of state-of-the-art photonic devices for quantum photonic applications realized by FLM on glass substrates. (A) Interferometer in 8 stages for the simulation of photonic quantum walk [66]. (B) Interferometer for photonic boson sampling [65]. (C) Patterning of gold resistors for thermal phase shifting [68].

## 2.3 Glass microstructuring

With *laser microstructuring* we indicate the ability to remove material from a substrate with micrometric control by exploiting laser light irradiation in at least one step of the process. *Direct laser ablation*, i.e. the removal of material due to laser-induced micro-explosions, was discovered very early in the history of short-pulse lasers, and the significant advantages of femtosecond pulses over pico- or nanosecond pulses were immediately evident and confirmed by many studies [70, 71], as we shall later discuss. The field of laser microstructuring is extremely vast and has important industrial applications such as laser cutting. For the purpose of this work, we shall limit ourselves to a brief review of microstructuring techniques in fused silica and borosilicate glass, as these transparent materials offer the intriguing possibility of integrating microstructures with laser-written photonic devices.

### 2.3.1 FLICE technique

The technique was first demonstrated in [72] and, as mentioned, is based on a two-step process that only works on a few materials, such as fused silica and Foturan glass by Schott. First, a portion of the substrate is irradiated by femtosecond pulses, with all the geometrical advantages we described in Sect. 2.1. Second, the sample is immersed in a hydrofluoric acid (HF) solution. Although the acid reacts with all the sample, the irradiated regions show an increase in etching rate of up to two orders of magnitude. This allows to produce structures with high aspect ratios and to create channels inside the glass that are of great appeal for microfluidic applications [73]. The physical mechanisms leading to the increase in etching rate in fused silica have been thoroughly investigated. A first mechanism is the decrease of the Si-O-Si bond angle induced by the hydrostatic pressure created in the irradiated region [74]. This explanation is particularly suited for low-intensity irradiation regimes. However, only a very modest increase in etching rate is obtained after irradiation in such regime. Much higher etching rates can be obtained with higher intensities, which lead to the formation of very peculiar self-ordered nanocracks perpendicular to the polarization direction of the beam [75]. The process through which such nanocracks are formed is described in [76] and [77]. The fact that they form perpendicularly to the polarization direction makes the polarization alignment critical for FLICE: if the beam is polarized orthogonally to the translation direction, the cracks will be aligned with the channel axis, thus favouring the diffusion of the etchant. Conversely, if the beam is polarized along the translation direction, the cracks will block the etchant and the etching rate will be significantly worse.

With respect to other standard techniques used in silicon-based processes such as wet chemical etching and deep reactive ion etching, microstructures produced with FLICE have several advantages: i) they avoid photolithography and clean rooms, ii) they create directly buried channels that do not require sealing with a cover glass, iii) they allow straightforward fabrication of 3D channels, which is otherwise prohibitive requiring complex multistep processes, iv) they naturally produce channels with circular cross-section, which are highly desirable in microfluidics and are not easily obtained through other techniques. State-of-the-art applications of FLICE for micro-optofluidics can be reviewed in [78–82] and a couple of examples are reported in FIG. 2.5.



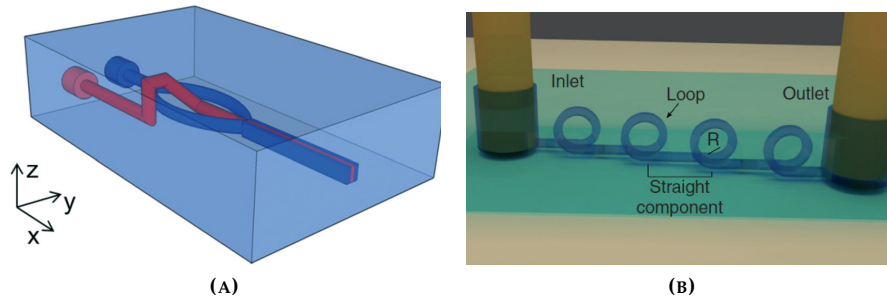


FIGURE 2.5: State-of-the art microfluidic devices realized by FLICE technique to perform different types of particle focusing. Image (A) from [78]. Image (B) from [80].

### 2.3.2 Direct laser ablation

Laser ablation was already discovered in the seventies as soon as short-pulse high energy lasers became available. The ablation process is strongly nonlinear, with physical principles very similar to the ones we discussed in Sect. 2.1, which makes it almost wavelength-independent. Ablation takes place when the density of free electrons in conduction band reaches a critical value. This happens when the laser fluence exceeds a certain threshold, at which point the electrostatic repulsion between the free electrons and the ionized nuclei is strong enough to cause a breakdown of the material and an expulsion of the nuclei. The minimum fluence below which the ablation process cannot be initiated is defined as *ablation threshold* [83]. The ablation threshold has been investigated in several materials [84] and it has been shown to depend strongly on the pulse length  $\tau$ . For  $\tau > 10$  ps, the process is controlled by the thermal conduction through the atomic lattice, which scales with  $\sqrt{\tau}$ . With pulses in the range of 100 fs, instead, the optical breakdown is a nonthermal process that is mostly triggered by nonlinear absorption such as multiphoton, tunnelling and avalanche. In this case the threshold still decreases with  $\tau$ , but less prominently. In the case of dielectrics, the material bandgap and the wavelength have been shown to have measurable effects on the threshold, as well as atmospheric pressure and gas conditions. As well as decreasing the ablation threshold, the use of femtosecond pulses has considerable advantages also on the geometrical and surface qualities of the ablated structures, as already shown in [70], of which we report three images for comparison in FIG. 2.6. An extensive, up-to-date review of most femtosecond laser ablation techniques can be found in [85], where a detailed description of the interaction dynamics between the pulse and the surface is also provided.

We should point out that laser direct ablation is typically limited to surface micromachining. Ablating features of significant depth is complicated by the presence of debris, which soon starts to interfere with the laser beam and prevents it from being focused on deeper regions, as well as blocking the expulsion of the ablated particles. The problem can be tamed by performing the ablation procedure with water covering the surface, and water-assisted laser processes have been known and employed for long time also in industrial applications, as extensively reviewed in [86, 87]. The presence of water has at least two effects: i) it helps the removal of debris in the machined areas by



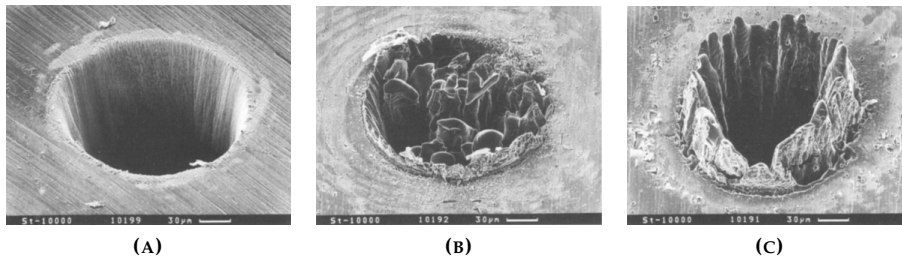


FIGURE 2.6: (A)  $\tau = 200$  fs,  $E = 120$   $\mu$ J,  $F = 0.5$  J cm<sup>-2</sup>. (B)  $\tau = 80$  ps,  $E = 900$   $\mu$ J,  $F = 3.7$  J cm<sup>-2</sup>. (C)  $\tau = 3.3$  ns,  $E = 1$  mJ,  $F = 4.2$  J cm<sup>-2</sup>. Comparison of single-pulse ablation traces with different pulse lengths on a steel foil. Notice that shorter pulses need a lower fluence to produce features of approximately the same size. Images from [70].

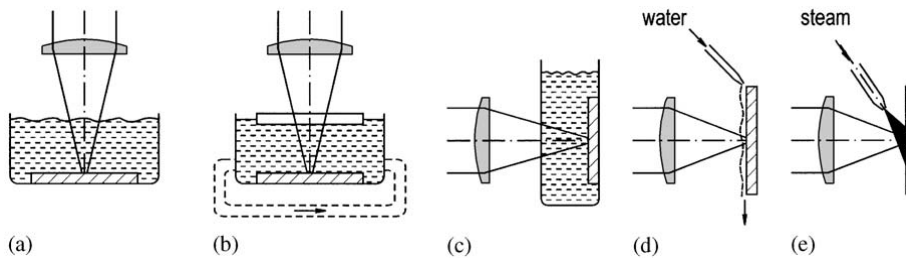


FIGURE 2.7: Schemes for providing water in the working area statically (a,c) or dynamically (b, d, e). Image from [87].

thermal convection or by bubble-induced liquid motion, which allows to ablate features with cleaner and steeper profiles, and ii) it favours heat flow, thus reducing thermal damage in the neighbouring areas. FIG. 2.7 shows some possible schemes for providing water in the working area, both statically and dynamically. In all of these schemes, the laser beam has to travel through the water layer before reaching the surface of the sample. This constitutes the main limitation of the technique, as the ablated material will still be accumulated close to the region of operation, thus often reducing the transparency of water. The movement of water itself can also interfere with the irradiation, particularly due to the formation of vapour bubbles. Therefore, albeit improved, there is no possibility of reaching 3D geometries even close the ones achievable with FLICE.

### 2.3.3 Water-assisted ablation from the rear surface

A smart solution to the problem was first proposed by Li *et al* [88]. If the main issue preventing in-depth ablation is the coincidence between the direction of the laser beam and the direction of ablation, they realized that a transparent material, where first-order absorption is suppressed (see Sect. 2.1), would allow to reverse the scheme and perform ablation *from the rear surface*, with the setup schematized in FIG. 2.9. They showed once more the difference between ablation in atmosphere and ablation underwater (FIG. 2.8A), they demonstrated holes with high aspect ratio (200  $\mu$ m deep while only 4  $\mu$ m wide) and, for the

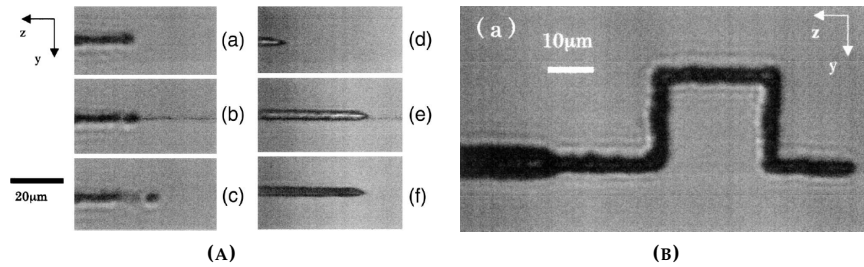


FIGURE 2.8: First example of water-assisted laser ablation from the rear surface. (A) Comparison between holes ablated in air (a,b,c) and in water (d,e,f). (B) Three-dimensional channel ablated in silica glass from the rear surface. Images from [88].

first time, they showed the ability to ablate three-dimensional channels (FIG. 2.8B). Hwang *et al* [89] repeated and expanded the experiment showing curved channels and trying different liquids, concluding that low-viscosity liquids are most advantageous for this purpose. In [90], the original experiment by Li *et al* was repeated in soda-lime glass with a very similar setup showing similar results, and the same authors published a further work [91] showing the ablation of microchambers, which probably constitutes the first demonstration of buried *volume* ablation.

The first microfabrications of this type were performed with short bursts of pulses, rather than with a continuous exposure. The scheme typically consisted of a Ti:sapphire laser with a 1 kHz repetition rate and a fast mechanical shutter. The shutter was opened in very short intervals to allow the exposure to a given number of pulses, then it was closed, the sample was moved to the next position, and the procedure was repeated until the desired geometry was achieved. Initially, dwell times were also added between successive bursts to allow the water to flow inside the channel. The authors of [91] were the first to demonstrate that dwelling was unnecessary and to perform the operation with a continuous exposure at 1 kHz and a writing speed of  $50 \mu\text{m s}^{-1}$ .

In [92] a first systematic, in-depth study of the dependence of the process upon several parameters was presented. Particular interest was given to the effect of different pulse energies, as a peculiar behaviour takes place when performing water-assisted ablation. When ablating in air, increasing the pulse energy increases both the width and the depth of the ablated channel, while producing rougher sidewalls. When ablating in water, instead, the depth of the channel increases only up to a given pulse energy, after which the ablated depth starts to decrease, reaching a final value that will remain the same at even

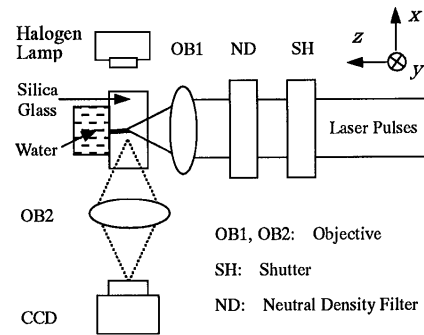


FIGURE 2.9: Schematics of the setup employed by Li *et al* [88]. The laser is focused on the rear surface, which is in contact with water.

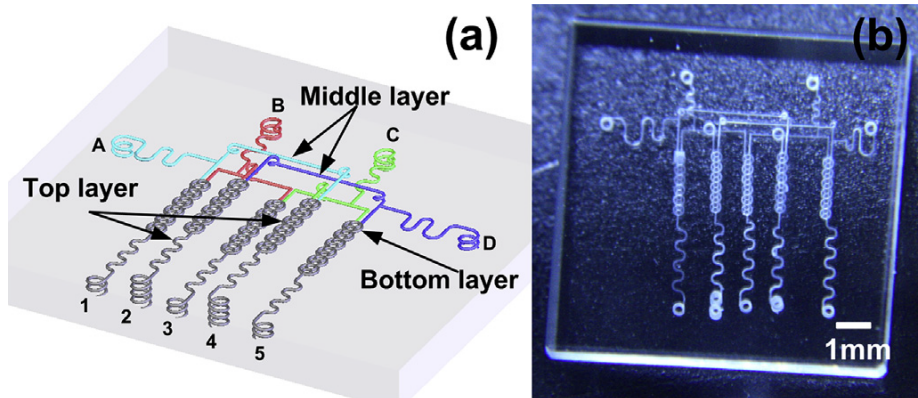


FIGURE 2.10: Water-assisted ablation of a complex 3D microfluidic device. Image from [93].

higher pulse energies. The authors linked this phenomenon to the formation of a hot and dense electron plasma at the glass-water interface which, instead of being quickly cooled and dispersed by water, is confined at the entrance of the channel, thus preventing at the same time the inflow of water and the expulsion of the ablated material.

The authors of [93] gave a different interpretation to water-assisted ablation, and they explained the removal of material as a result of the shock-wave produced when the laser pulse is focused *in water*, close to the surface of the sample. The pulse causes a sudden evaporation which produces a high-speed jet whose pressure is well above the hardness of silica glass, therefore the jet can easily reduce silica to debris and expel it. Anyway, regardless of the interpretation of the microscopical mechanisms, they confirmed that the main issue to the technique and its possibility to ablate very long channels is the correct ejection of the debris, which is problematic especially in 3D geometries. They proposed an innovative solution to the problem, consisting in attaching a rubber tube to the rear surface of the sample, and to periodically push and pull the water pressure into it. They do not explain in detail how this pumping is configured, but they claim that it is very efficient for taking away the debris. They were able, indeed, to demonstrate the ablation of impressively long and complex 3D channels, as shown in FIG. 2.10.

Although not strictly related to *femtosecond* laser micromachining, two more recent works are worth mentioning. In [94] and [95] an internal thread was demonstrated by water-assisted ablation using the second harmonic of a *sub-nanosecond* Nd:Yag laser. The authors demonstrated that an internal thread

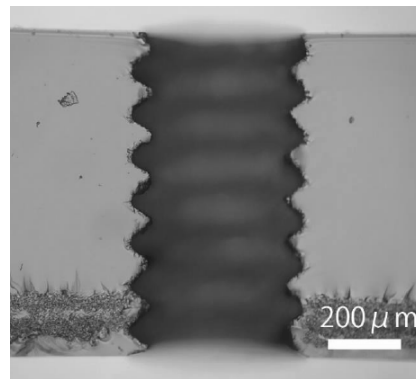


FIGURE 2.11: Internal thread fabricated by water-assisted laser ablation. Image from [94].

	Laser	$\lambda$ [nm]	$\tau$ [fs]	$E_p$ [ $\mu$ J]	NA	$v_{wr}$ [ $\mu\text{m s}^{-1}$ ]	$f$ [Hz]
[88]	Ti:sapph	800	120	1	0.55	[bursts]	$1 \times 10^3$
[89]	Ti:sapph	800	100	3 - 33	0.42	[bursts]	$1 \times 10^3$
[90]	Ti:sapph	800	380	3.2 - 9.3	0.50	[bursts]	$1 \times 10^3$
[91]	Ti:sapph	800	380	1.4	0.50	50	$1 \times 10^3$
[92]	Ti:sapph	800	100	20 - 230	0.30	10 - 60	$1 \times 10^3$
[93]	Ti:sapph	800	120	6	0.40	160	$1 \times 10^3$
[95]	Nd:Yag	532	0.5 ns	20	0.40	1000	$1 \times 10^3$

TABLE 2.1: Collection of the most relevant fabrication parameters of the work reviewed in this chapter. In the order: laser type, wavelength, pulse length, pulse energy, numerical aperture of the focusing objective, writing speed, repetition rate.

could be fabricated with high enough precision to allow the insert of a matching male screw. To the best of our knowledge, this is the first demonstration of the use of water-assisted ablation to remove large volumes from the substrate, as the thread they ablated has a 0.5 mm diameter and is 1 mm high (see FIG. 2.11). The key idea is that ablating the whole volume is unnecessary. Instead, they ablated the outer surface of the thread and an internal cylindrical surface, so that the portion of glass to be removed would simply detach integrally. Together with a writing speed more than ten times higher with respect to all other works, this allowed them to complete the machining of the tread in about 32 minutes.

To conclude this review of water-assisted ablation processes, in TABLE 2.1 we report a comparative table of the fabrication parameters employed by the authors we mentioned. This is not intended as a comprehensive review, but rather a comparative overview of the most commonly employed parameters. We should point out, in particular, that all experiments were invariably conducted with a 1 kHz repetition rate. The use of higher repetition rates, which might further reduce processing times, seems to be still unexplored.

## Chapter 3

# Materials and methods

### 3.1 Fabrication setup

The schematic of our fabrication setup is reported in FIG. 3.1. The laser source is a Spirit One 1040-16 by Spectra-Physics. This is a commercial laser system based on chirped pulse amplification. The Ytterbium-based oscillator works at  $\simeq 63$  MHz with a central wavelength of 1041 nm. The repetition rate of the amplifier can be varied by selecting different regimes corresponding to 200, 350, 500, 750 or 1000 kHz, and an internal pulse picker allows to further divide the repetition rate by integer numbers. As an example, a 50 kHz repetition rate can be obtained by setting the 200 kHz regime and the pulse picker to 4. The laser pulse length is of about 400 fs.

Although the laser has an internal power selector, a finer and handier control is achieved by cascading a  $\lambda/2$  waveplate and a PBS (polarizing beam splitter) at its output. The light exiting the laser is linearly polarized, so the waveplate has the effect of rotating the polarization direction by a given amount, and the transmitted intensity is determined by the relative orientation of the waveplate and the PBS axis.

Two flip-mirrors can be inserted in the path to deviate the beam through an LBO crystal for second harmonic generation, when needed. In our case, all fabrications were performed at 1041 nm so the additional path was never employed. The laser beam therefore goes straight to a mechanical shutter that is electronically synchronized to the motion stages, allowing to open or block the laser beam with a switching time of about 10 ms. The beam is finally focused onto the sample by a microscope objective. Several objectives with different magnifications and numerical apertures are available.

The sample is mounted on a Thorlabs GM100 gimbal which provides fine control over the tilt angles. The translation is operated by a high-precision motion system (Aerotech FIBERGLide 3D). The system is composed by 3 independent linear stages lying on a compressed air bearing and driven by brushless linear electric motors. This allows smooth and uniform three-dimensional movement with a position accuracy below 100 nm. The stages can reach translation velocities of up to  $300 \text{ mm s}^{-1}$  within a  $10 \text{ cm} \times 15 \text{ cm}$  travel range in the horizontal plane and a 5 cm travel range in the vertical direction. The stage position is monitored by optical encoders with a resolution of 1 nm. The movement of

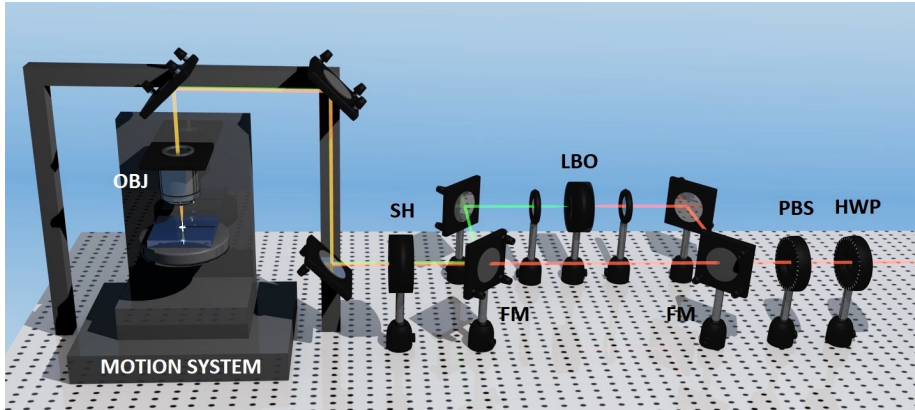


FIGURE 3.1: Schematic of the fabrication setup employed. From right to left: half-wave plate (HWP), polarizing beam splitter (PBS), flip-mirrors (FM) to deviate the beam to the (optional) second harmonic generation path through the LBO crystal, mechanical shutter (SH), focusing objective (OBJ). Image from [96].

the stages, as well as the synchronized opening of the mechanical shutter, is computer controlled and programmed in G-code language, typically used in numeric controlled machines.

The alignment of the sample to the laser beam is critical for a correct fabrication. We can achieve a high precision alignment by observing the back-reflection of the beam with a CCD positioned above the objective, behind the upper mirror. When the beam is precisely focused on the surface of the sample, the back-reflected light will be collected by the objective and imaged onto the CCD, where a bright spot will be visible. The sample is then moved to different positions and the tilt is iteratively adjusted until the sample is perfectly parallel to the horizontal plane. In this way, the position of the sample with respect to the focal point can be referenced with an accuracy of few microns.

We conventionally measure the optical power by inserting the head of the powermeter just before the focusing objective, so to obtain reproducible measurements of the power actually reaching the sample (up to a small loss factor introduced by the objective). Measuring *after* the objective would be, in principle, more accurate, but it is infeasible as there is not enough clearance between objective and sample to insert the head of the powermeter. We employed a Coherent LabMax powermeter with a 3 W maximum power head. The CW power  $P$  we measure is linked to the pulse energy  $E_p$  by the simple relation

$$P = E_p \cdot f \quad (3.1)$$

where  $f$  is the repetition rate.

## 3.2 Characterization techniques

### 3.2.1 Microscope inspection

Laser-fabricated microstructures in glass can be visually inspected through an optical microscope. We used a Nikon ME600 microscope that can be switched

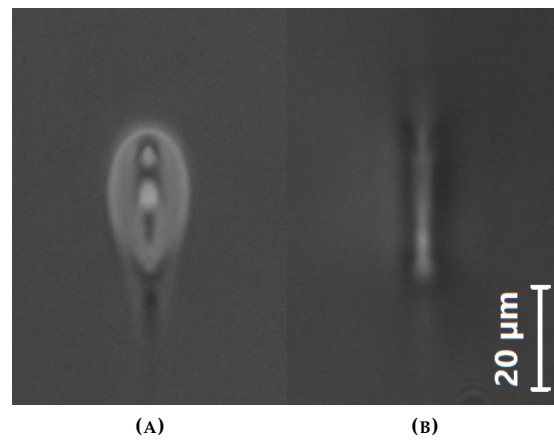


**FIGURE 3.2:** Microscope images of the sample facets with waveguides cross-section. The laser beam impinges from the upper side of the image. (A) Waveguide written at 1 MHz repetition rate, i.e. *high frequency* regime. (B) Waveguide written at 200 kHz repetition rate, i.e. *low frequency* regime. The droplet-like shape of the first image is typical of high frequency writing.

from transmission to reflection mode and is equipped with a Differential Interference Contrast (DIC) module, which allows enhanced vision over features with small index contrasts. The microscope is also equipped with a high resolution CCD camera for real-time acquisition of the image and a dedicated software is calibrated to allow the measurement of the actual dimensions of the microstructures.

In transmission mode, the image can indeed be very sensitive to index contrasts, and even waveguides with moderately low index contrast are usually clearly visible. Additionally, damages or interruptions of the waveguides are immediately recognizable. An inspection of the facets of the sample is usually performed as well. This allows to acquire an image of the cross-section of the waveguide, which provides valuable initial information and comparison over waveguides written in different regimes, as shown in FIG. 3.2.

In the case of microstructures, such as the ones obtained by FLICE or water-ablation, microscope inspection is fundamental to check that the structure was fabricated correctly. Both transmission and reflection mode can be conveniently exploited for this purpose.

### 3.2.2 Waveguide characterization

If the waveguide does not show damages or interruptions at the microscope, we move to its optical characterization. We dispose of several laser sources of different wavelengths for this task. Light is inserted into the waveguide in one of the two ways depicted in FIG. 3.3. In the first case light is focused onto the input facet by a microscope objective. In the second case, light is coupled into a single-mode fiber that has been stripped of the external cladding, so that the tip of the fiber can then be brought close to facet of the sample and meet the extremity of the waveguide. Both methods require the use of micrometric

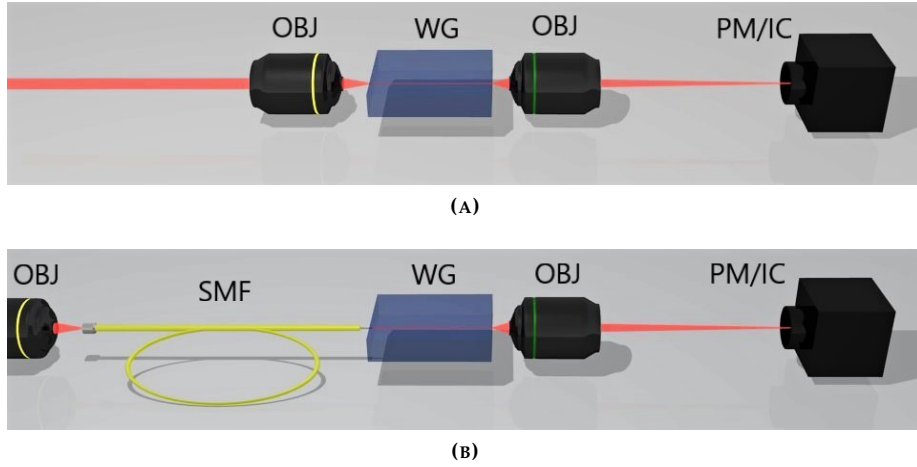


FIGURE 3.3: Setups for the characterization of waveguide performances. (A) From left to right: laser beam, focusing objective (OBJ), sample with written waveguide (WG), collection objective (OBJ), powermeter or imaging camera (PM/IC). (B) Same setup, but with fiber *butt-coupling* through a single-mode fiber (SMF). Image from [96].

multi-axis translators for the accurate positioning of the focusing objective (or fiber), of the sample, and of the collection objective.

We use the final power-meter stage to measure the overall transmitted power. At the end of the experiment, we remove the sample and re-measure the transmission of the optical line. By comparing the two, we calculate the corresponding *insertion losses* as

$$IL_{[\text{dB}]} = -10 \log_{10} (P_{\text{sample}} / P_{\text{no-sample}}) \quad (3.2)$$

which represent the total power loss when the sample is inserted into the line. The overall power losses can be subdivided in at least three separate contributions. *Fresnel losses* are due to reflections at the glass-air interfaces and are related to the difference in refractive index between the two media. They are given by Fresnel's formula

$$FL_{[\text{dB}]} = -10 \log_{10} \left[ 1 - \left( \frac{n_2 - n_1}{n_2 + n_1} \right)^2 \right]. \quad (3.3)$$

We have then *coupling losses*, which originate from the mismatch between the field profile at the input stage (objective or fiber) and the field profile of the guided mode. When coupling with an objective, the input field profile depends on both the output mode of the laser and the characteristics and fine positioning of the focusing objective, so it is not easily retrievable. Therefore, although sometimes less practical, fiber butt-coupling is usually preferred, as in such case the input field profile is given by the mode shape of the fiber, which is known by manufacturer specifications. In such case the coupling losses can be written as

$$FL_{[\text{dB}]} = -10 \log_{10} O \quad (3.4)$$



being  $O$  the so-called overlap integral

$$O = \frac{|\iint E_{\text{wg}}(x, y)E_f(x, y) dx dy|^2}{\iint |E_{\text{wg}}|^2 dx dy \iint |E_f|^2 dx dy} \quad (3.5)$$

where  $E_{\text{wg}}$  and  $E_f$  are the waveguide and the fiber field profiles respectively. As discussed in the next chapter, the field profile of single mode guiding structures has no sign inversion, so it can be retrieved by the corresponding intensity profile. The profile of the waveguide is measured by projecting its output onto the CCD camera and acquiring the corresponding image. The profile of the fiber is measured by removing the sample and bringing the fiber close to the collection objective, so to image its output onto the camera. Once the two images are acquired, a custom software performs the integral operation and estimates the coupling losses.

The last contribution is due to *propagation losses*, which originate from the natural absorption of glass and from the scattering due to defects. As the total insertion losses are given by

$$IL_{[\text{dB}]} = FL_{[\text{dB}]} + CL_{[\text{dB}]} + PL_{[\text{dB}/\text{cm}]} \cdot l \quad (3.6)$$

where  $l$  is the length of the sample, propagation losses can be retrieved as

$$PL_{[\text{dB}/\text{cm}]} = [IL_{[\text{dB}]} - FL_{[\text{dB}]} - CL_{[\text{dB}]}] \cdot l^{-1} \quad (3.7)$$

In curved waveguides the additional contribution of bending losses needs to be taken into account, but that is never the case for the waveguides considered in this work.

### 3.3 Fiber pigtailling

With *pigtailling* we indicate the operation of gluing a fiber to the facet of a sample so that it maintains an optimal alignment with the waveguide. The advantage in performing this operation is twofold: on one side, once the fiber is glued, the sample can be moved without losing the coupling; on the other side, the glue matches the refractive index of glass, so that Fresnel losses are measurably reduced and the overall transmission is improved. We employ a UV-curing glue (Delo Photobond GB345) that is initially liquid and solidifies after the exposure to UV light.

#### 3.3.1 Nanopositioning setup

The pigtailling operation is performed on a high-precision alignment system based on H-811 6-axis hexapods by PI (FIG. 3.4). The hexapod platform is actuated by six brushless motors that provide a travel range of about 2 cm in the three directions with respect to its central position with a repeatability of  $\pm 60$  nm. The motion is computer-controlled and is encoded in six coordinates: three coordinates encode the translation with respect to the  $(x, y, z)$  axis, and three coordinates encode the rotation angles around those axis  $(\theta_x, \theta_y, \theta_z)$ . Besides the great position accuracy, what makes this system particularly suitable for pigtailling is that the angles of rotation can be set at software level to operate

around an arbitrary pivot point. It is greatly convenient to set the virtual center of rotation at the tip of the fiber, so that the fiber can be rotated without moving its extremity, i.e. with no cross-talk on other degrees of freedom, thus allowing an extremely fine optimization of the alignment to the waveguide, difficult to achieve with standard mechanical stages.

Our setup is shown in FIG. 3.5. It is composed of two hexapods (A and B) facing each other, and a sample-mount stage (C) in the middle, which allows to pigtail a sample from both sides in a single step, if needed. A long working distance ( $\simeq 9$  cm) microscope (D) equipped with a CCD camera connected to the computer, allows real time vision with variable magnification to control the fine positioning. Since the magnification of the image can be varied, the illumination needs to be adjusted consequently, and the two movable LED lights (E) serve this purpose. Sample and camera mounts can move on two axis and are both computer-controlled via the same software as the hexapods. Overall, this builds up to a high-precision, high-flexibility positioning system. Furthermore, a second camera equipped with a high magnification macro objective can be mounted in any position around this setup, allowing to have simultaneous imaging from two different angles, which turns out to be greatly convenient when dealing with 3D microstructures.

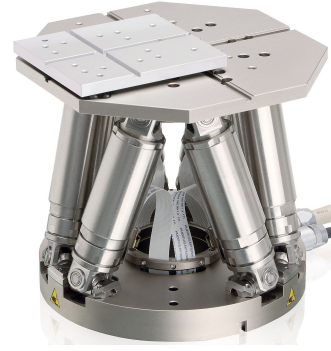


FIGURE 3.4: H-811 hexapod by PI.

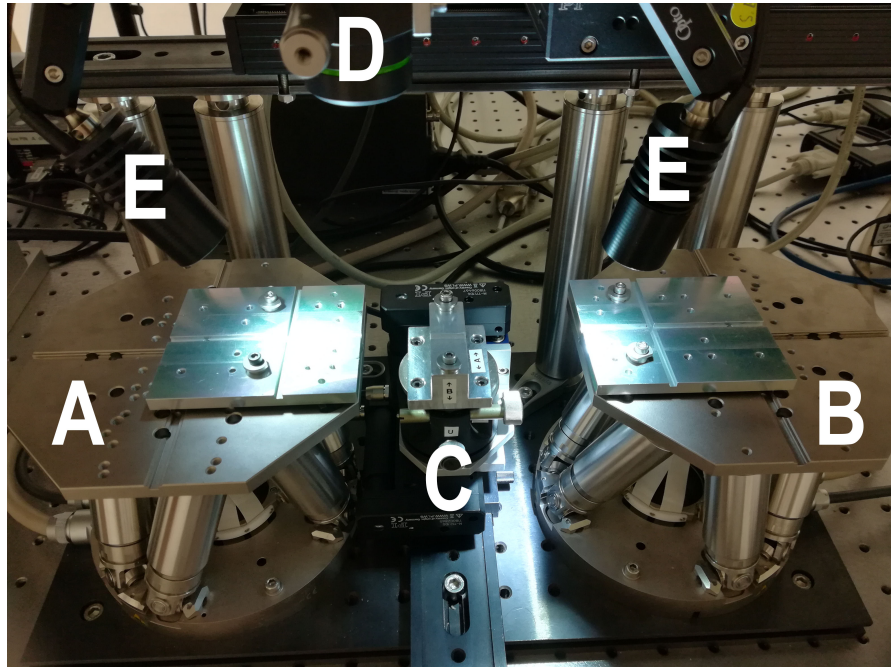
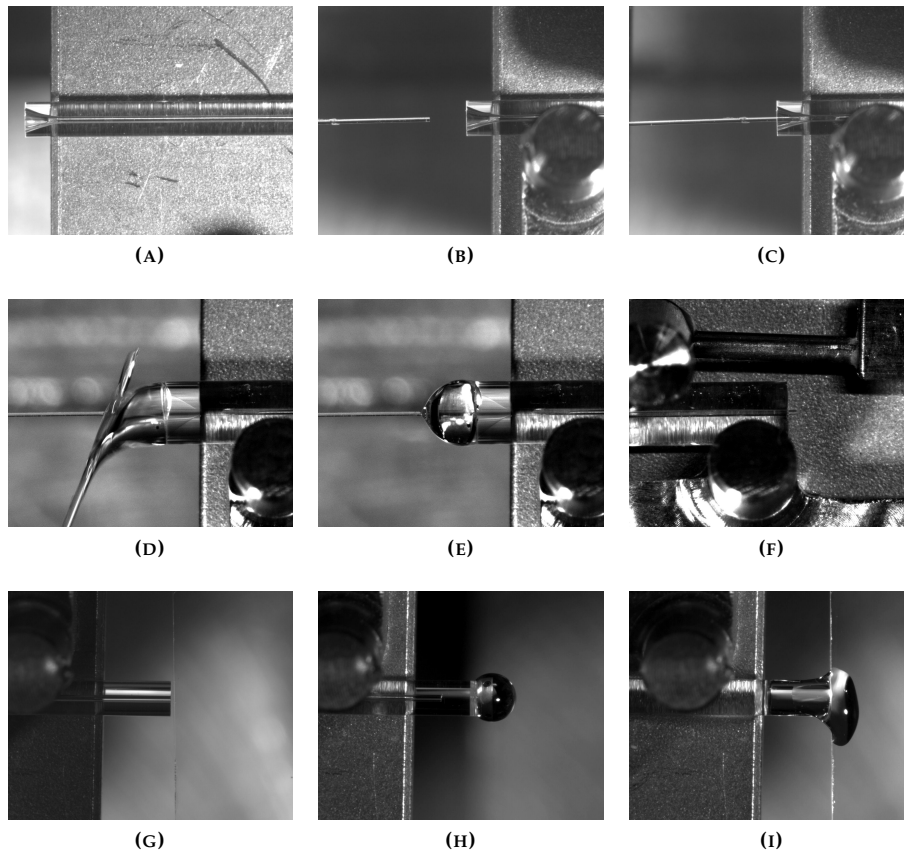


FIGURE 3.5: High-precision micropositioning setup. (A,B) Hexapod stages. (C) Sample-mount stage. (D) Microscope. (E) Illumination LEDs.



**FIGURE 3.6:** Steps for the pigtailing procedure. (A) Ferrule. (B-C) Fiber insertion into the ferrule (initial). (D-E) Glue deposition. (F) Fiber insertion (complete). (G) Fine optimization of the alignment to the waveguide. (H) Pull-back and glue deposition. (I) Final attachment to the sample.

### 3.3.2 Pigtail operation

The pigtail operation is performed in several steps. Since we want the tip of the fiber to get almost in contact with the facet of the sample to match the extremity of the waveguide, we need to strip the fiber of its external cladding and cleave it precisely, with suitable tools. As a downside, the extremity of the fiber becomes rather fragile without the cladding, so gluing it directly to the sample would be possible but impractical, as it would easily break. Therefore, we first insert the fiber into a 10 mm long glass ferrule (FIG. 3.6A), that acts as a protective sock. To do so, the fiber and the ferrule are mounted on the two hexapods through specific holders. The fiber is first inserted into the ferrule by 2 or 3 millimetres (FIG. 3.6B and FIG. 3.6C), which is facilitated by the funnel-shaped aperture of the ferrule. A droplet of glue is then deposited at the entrance of the ferrule (FIG. 3.6D and FIG. 3.6E), and the fiber is pushed forward until its tip exits from the other side of the ferrule by few microns (FIG. 3.6F). The operation is performed in this sequence because, when sliding in,

the fiber will drag some glue inside the ferrule, which will make the resulting "sock" much more solid, once the glue is solidified by exposure to UV light. The hexapods are extremely convenient to perform this operation, as they allow a fine alignment of fiber and ferrule and they reduce the risk of breaking the fiber during the insertion.

Once the ferrule is inserted and the glue is UV-cured, the fiber can be safely managed without any risk of breaking it. Light from a laser source is coupled into the fiber and the fiber is brought close to the sample (mounted onto its designated stage) to couple light into the waveguide. The light at the output of the waveguide is collected with an aspheric lens and imaged onto an Ophir NOVA II power-meter. The alignment is finely optimized by iteratively moving the fiber to maximize the output power (FIG. 3.6G). Once the maximum transmission is reached and we are satisfied with the alignment, the fiber is pulled back from the sample by some millimetres to allow the deposition of another droplet of glue (FIG. 3.6H) and finally brought back to its optimized position (FIG. 3.6I), where the glue will perfectly fill the gap between the fiber and the sample. If the operation is performed correctly, a measurable increase in transmitted power should be seen, due to the index-matching of the glue. Notice that this operation is facilitated by the perfect position repeatability of the hexapods, which ensures that, once the fiber is pulled back, re-entering the coordinates of the optimized position will bring the fiber exactly to the previous place, so that almost no further optimization is necessary. After a final irradiation with UV light to solidify the glue, the operation is completed.

## Chapter 4

# Design of the optomechanical modulator

### 4.1 Working principle

To realize a first proof-of-principle of optomechanical modulation in an entirely FLM-based platform, we aim at demonstrating an intensity modulator based on the integration of the simplest optical element, i.e. a straight waveguide, with the simplest micromechanical element, i.e. a cantilever beam. Writing a waveguide is the simplest part of the problem, while fabricating the cantilever involves some microstructuring technique whose choice will depend on the choice of material (see Sect. 2.3). A conceptual picture of the device is reported in FIG. 4.1. A waveguide is written inside the cantilever passing along the whole length of the beam and continuing on the other side. The motion of the cantilever will then cause a misalignment of the two extremities of the waveguide, therefore causing a (periodical) modulation of the transmitted intensity.

The change in transmitted intensity can be formally interpreted in terms of coupling losses. The spatial displacement of the cantilever, indeed, will also cause a displacement of the field profile of the waveguide, resulting in a mismatch with the field profile on the other side. If we assume that the free-space propagation between the end of the cantilever and the beginning of the next portion of glass is short enough for the field profile not to diverge significantly, then the coupling factor is given by the same overlap integral presented in Eq. (3.5), except in this case we are not computing the overlap of the waveguide's mode with the fiber's mode, but the overlap of the waveguide's mode with itself, displaced by a given vector  $\mathbf{d} = d_x \mathbf{u}_x + d_y \mathbf{u}_y$  ( $z$  is assumed as the direction of propagation, parallel to the length of the cantilever). Considering Eq. (3.5) and normalizing  $\iint |E_{\text{wg}}|^2 dx dy = 1$ , the function describing the coupling efficiency is

$$\eta(d_x, d_y) = \left| \iint E_{\text{wg}}(x, y) E_{\text{wg}}(x - d_x, y - d_y) dx dy \right|^2 \quad (4.1)$$

which is nothing but the convolution of the waveguide's field profile. Now, the theory of guided optics ensures that in single-mode waveguides the fundamental mode has no sign inversion [97], therefore the field profiles can be written in

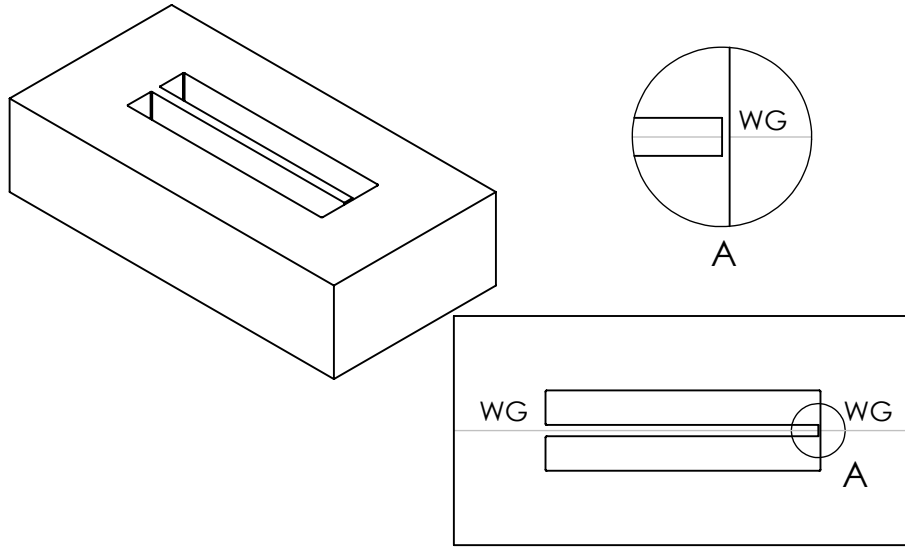


**FIGURE 4.1:** Schematics of the ideal device. The gray line represents the waveguide (WG), and the detail in circle A shows the interruption point between the end of the cantilever and the beginning of the next portion of glass. The movement of the cantilever causes a misalignment of the two extremities, resulting in a modulation of the transmitted intensity.

terms of intensity profiles as

$$\eta(d_x, d_y) = \left| \iint \sqrt{I_{\text{wg}}(x, y)} \sqrt{I_{\text{wg}}(x - d_x, y - d_y)} dx dy \right|^2 \quad (4.2)$$

where  $I_{\text{wg}}(x, y)$  is a quantity that can be directly measured by imaging the output of the waveguide on a CCD camera, as described in Sect. 3.2.2.

The analytical form of the field profile  $E(x, y)$  of a guiding structure is known only in very simple cases, such as step-index cylindrical structures. In graded-index structures such as commercial fibers or, in our case, FLM-written waveguides, no analytical form is typically available. However, in single-mode structures (both fibers and waveguides) the actual shape of the fundamental mode is usually well approximated by a two-dimensional gaussian function, so that the intensity profile can be expressed as

$$I_{\text{wg}}(x, y) = I_0 \exp\left(-\frac{x^2}{2\sigma_x^2}\right) \exp\left(-\frac{y^2}{2\sigma_y^2}\right). \quad (4.3)$$

Inserting this expression into Eq. (4.2) the convolution integral can be separated as the product of two convolutions in  $x$  and  $y$ .

$$\eta(d_x, d_y) = \left| \int \sqrt{I_{\text{wg}}(x)} \sqrt{I_{\text{wg}}(x - d_x)} dx \right|^2 \left| \int \sqrt{I_{\text{wg}}(y)} \sqrt{I_{\text{wg}}(y - d_y)} dy \right|^2 \quad (4.4)$$

It is possible to demonstrate that the convolution of two gaussian functions is itself a gaussian function where  $\sigma_{\text{conv}}^2 = \sigma_1^2 + \sigma_2^2$ . In this case each function

is being convoluted by itself, meaning  $\sigma_{\text{conv}}^2 = 2\sigma^2$ . The final result is easily found as

$$\eta(d_x, d_y) = \eta_0 \exp\left(-\frac{d_x^2}{4\sigma_x^2}\right) \exp\left(-\frac{d_y^2}{4\sigma_y^2}\right) \quad (4.5)$$

where  $\eta_0$  is the transmission when the cantilever is not deflected, i.e. the waveguides are perfectly aligned.

If, for instance, the cantilever is displaced horizontally, so that

$$\eta(d_x) = \eta_0 \exp(-d_x^2/4\sigma_x^2) \quad (4.6)$$

then the expression can be reversed as

$$d_x = 2\sigma_x \sqrt{\ln(\eta_0/\eta)}. \quad (4.7)$$

Let us assume, as an example, that the waveguide has  $\sigma_x = 10 \mu\text{m}$ . To decrease the transmission by 50%, the cantilever needs to be displaced by  $16.6 \mu\text{m}$ . To decrease the transmission by 90% ( $\eta = 0.1\eta_0$ ) the displacement would need to be  $30.3 \mu\text{m}$ . It is evident, therefore, that the mode dimensions of our waveguide will be fundamental in determining the behaviour of our device, and a waveguide with a smaller mode will be always preferred, as it allows to have the same intensity modulation with a smaller displacement of the cantilever, which is easier and safer to achieve.

As a conclusive note, we should point out that, if the cantilever performs an oscillatory motion at a given frequency  $f$ , the intensity transmitted by the waveguide is modulated with frequency  $2f$ . This is because the transmission is symmetric with respect to the cantilever displacement on either side, and in each oscillation period the cantilever crosses its central position (that is also the position of maximum transmission) twice. As a result, in each oscillation cycle of the cantilever, the transmitted intensity will have two maxima (corresponding to crossing the rest position back and forth), and two minima (corresponding to the points of maximum displacement on either side).

## 4.2 Choice of the substrate

The choice of the substrate depends on several considerations. In Sect. 2.3 we reviewed two different microstructuring techniques: FLICE and water-assisted ablation. FLICE is a well-established technique, and has already proved to be able to produce microstructures of much higher complexity than the one we plan to realize here. It appears, therefore, that FLICE would be an easy choice for our purpose. The downside, however, is that FLICE can be only performed, up to now, in fused silica and few other materials. For instance, a recipe to perform FLICE on borosilicate glass, which is among the commonly employed substrates for the fabrication of complex photonic devices such as the ones reviewed in Sect. 2.2.2, has not yet been demonstrated.

As clearly pointed out in [73], the writing of good quality waveguides in fused silica is somewhat problematic. Waveguides have been written in both low frequency [98] and high frequency regimes. In low frequency regime, good waveguides with low losses and symmetric mode shape were achieved, but they show refractive index contrast in the order of  $1 \times 10^{-3}$ , which is too low

to allow the fabrication of curved waveguides (essential for many photonic applications) without significant bending losses. In high frequency regime, on the other hand, an index contrast of around  $6 \times 10^{-3}$  was achieved, but at the expense of some damaging of the region close to the waveguide [73]. On the contrary, borosilicate glass has been shown to provide optimal quality single-mode waveguides with good index contrast within large windows of fabrication parameters.

Since our device consists of a single, straight waveguide, both substrates could be adopted in principle. However, this work is meant to be an initial step towards the integration of micromechanical elements in photonic circuits. Fabricating our device in fused silica with FLICE technique would be most likely easier, but less open to future innovations, as it would be fundamentally bound to work only on a specific material that, at present, does not allow to easily fabricate complex circuits. On the contrary, laser ablation has been demonstrated in almost any material, from metals to dielectrics, so our results would be easily extensible to any other material that allows to write waveguides of some sort (including fused silica).

In conclusion, we decided to realize our device in borosilicate glass through water-assisted ablation.

## 4.3 Geometry

### 4.3.1 Dimensions

Similarly to what is usually done in silicon-based technologies, creating a cantilever requires to dig a U-shaped cavity that starts at both sides of the cantilever and connects underneath it. This frees a portion of material from its surrounding, creating what is often referred to as a *bridge* structure. To have a cantilever it is then sufficient to cut one of the extremities of the bridge to free its motion.

There are two main limitations to how thin a cantilever can be realized. The first is related to the resolution of the ablation technique, which is in the order of few micrometres. As a consequence, one cannot expect to be able to fabricate reliably and repeatably a cantilever that is, as an example, thinner than  $10 \mu\text{m}$ . The second limitation, which is actually more restrictive, is that a waveguide must pass through the cantilever. The cantilever must be thick enough not only to properly host the laser-modified region of the waveguide, but to also accommodate the field profile of the guided mode, which normally extends outside of the modified region by several microns or even tens of microns. If the cantilever were thin enough to intercept the tails of the field profile, light could be coupled outside of the waveguide through the scattering caused by surface imperfection. Knowing that FLM-written waveguides have typical mode dimensions in the order of  $10 \mu\text{m}$  we decided, as a safe initial assumption, to fabricate all cantilevers with a  $50 \mu\text{m}$  thickness.

Once the thickness is chosen, according to Eq. (1.27) the resonance frequency only depends on the length. In principle, there is no limitation as to how short or how long the cantilever should be. However, a very short cantilever will be very stiff, i.e. will have a very high elastic constant and a very high resonant frequency. This is undesirable for several reasons: firstly, as we mentioned in



Sect. 1.4.3, most applications benefit from low- $k$  cantilevers; secondly, displacing the cantilever by a sufficient amount to have a measurable modulation of the transmitted intensity would produce great mechanical stress and possibly cause it to break, while we want our cantilever to operate in a region of safe elasticity. On the other hand, a cantilever too long would be equally undesirable, as it would take very long time to fabricate (especially if we prove unable to increase the writing speed significantly with respect to the ones reported in TABLE 2.1) and the resulting cantilever would probably have a very low quality factor (see Sect. 1.3.2). As a reasonable trade-off, we decided to fabricate cantilevers with lengths in the order of 1 mm. The substrate we use is the commercial Eagle XG glass by Corning which has, by manufacturer's specification, density  $\rho = 2380 \text{ kg m}^{-3}$  and Young's modulus  $E = 73.6 \text{ GPa}$ . This corresponds, through Eq. (1.27), to a theoretical resonance frequency of about 45 kHz.

The choice of the remaining dimension of the cantilever (the width, i.e. the dimension orthogonal to the movement) is irrelevant as far as the resonance frequency is concerned. On one side, we prefer to have it wide enough to a) match the approximations at the base of most theoretical models presented in Sect. 1.3.2 and b) avoid any unwanted coupling of the two orthogonal modes of oscillations. On the other hand, a wider cantilever takes longer to fabricate. Therefore, once again, we chose as a trade-off to fabricate 250  $\mu\text{m}$  wide cantilevers.

### 4.3.2 In-plane VS out-of-plane oscillation

Most cantilevers realized by silicon-based techniques are designed to oscillate out-of-plane, i.e. orthogonally with respect to the surface of the substrate over which they are fabricated. In our case, there are several reasons to prefer, instead, an in-plane oscillation configuration. The geometrical difference between the two can be clearly visualized in FIG. 4.2.

As a first consideration, one can immediately observe that the out-of-plane configuration (right side of FIG. 4.2) forces to remove a wider portion of material underneath the cantilever. This is a region where water has to flow horizontally, instead of vertically, to be in contact with the surface to ablate, and the debris needs to be expelled horizontally as well. The literature we have reviewed in Sect. 2.3 shows indeed that the regions of horizontal ablation tend to be kept as short as possible, as they clearly represent an unfavourable geometry. In our case, the in-plane configuration is more favourable on this regard, as the cantilever represents much less of an obstacle and the region of horizontal ablation is reduced to only 50  $\mu\text{m}$ .

Secondly, we must take into account the possibility that our ablation technique might not have a vertical resolution as good as the horizontal one. The problem is the asymmetry of the nonlinear interaction region, which we already pointed out in Sect. 2.2 and can be well visualized by observing the waveguide profiles of figure FIG. 3.2, particularly the one written in low-frequency regime (B), which is the regime of interest for ablation, as we will use repetition rates well below 1 MHz. It is evident that while in the horizontal direction the interaction region is confined to a small area of few micrometers, in the vertical direction the regions extends for at least 20 to 30  $\mu\text{m}$ . When ablating vertical features, the spot is translated vertically with respect to the sample, which is equivalent to having a "blade" of few micrometres. When ablating horizontal

features such as the region underneath the cantilever, the spot is translated horizontally, so the "blade" is much larger and one cannot expect to have the same resolution. Now, the width and the length of the cantilever are critical in determining its resonant frequency, so we want to be able to reproduce their designed dimensions as accurately as possible. In out-of-plane configuration, the width of the cantilever would be determined by a region of horizontal ablation. Instead, in in-plane configuration the width would be determined vertically, i.e. with a supposedly better resolution, which is why, again, the latter is preferable.

As a final remark, we should point out that waveguides written in transversal mode (see Sect. 2.2) have a tendency to exhibit slightly elliptical mode shapes with  $\sigma_x < \sigma_y$ , due to the same reasons we just discussed. Should that be the case in our device, we would benefit from oscillating along the direction with smaller  $\sigma$  (see Eq. (4.6) and Eq. (4.7)), meaning the in-plane configuration would be more favourable.

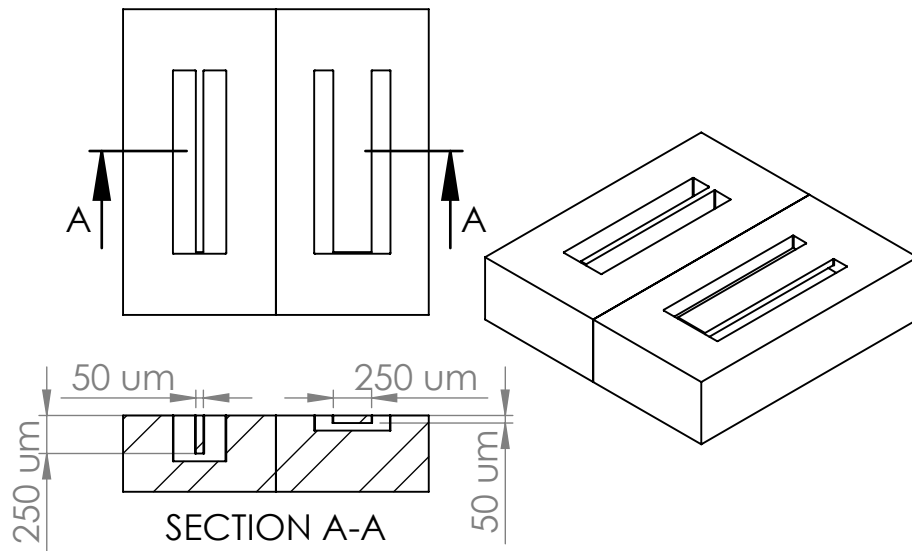


FIGURE 4.2: Comparison between cantilevers designed for in-plane (left) and out-of-plane (right) oscillation. In-plane geometry requires to ablate a longer vertical hole, while out-of-plane geometry requires to ablate a longer horizontal region underneath the cantilever.

## Chapter 5

# Fabrication of the microcantilever

### 5.1 Development of water-assisted ablation

The first experimental step of the work was the implementation and optimization of water-assisted ablation on our platform. In detail, given the geometric specifications we discussed in the previous chapter, we needed to bring our process to a point where it could reliably

- ablate rectangular cavities at least  $300\ \mu\text{m}$  deep, as the cantilever is  $250\ \mu\text{m}$  wide and a portion of material needs to be ablated underneath it;
- ablate buried horizontal regions at least  $25\ \mu\text{m}$  long, as the cantilever is  $50\ \mu\text{m}$  thick and the horizontal region can be ablated in two steps, starting from each side;
- perform a precise cut to free the extremity of the cantilever, ideally as narrow as possible.

As a starting point, we considered the fabrication parameters summarized in TABLE 2.1. Our laser system is the Ytterbium-based oscillator discussed in Sect. 3. We decided to employ a commercial Achroplan 20x - 0.45 NA objective by ZEISS. This objective has a numerical aperture that is in the average of what has been employed in literature. Furthermore, it has a working distance of about 2 mm, which is suitable for performing rear-surface ablation of a substrate that has, in our case, a thickness of 1.1 mm, while maintaining good clearance between objective and sample. As a point of discontinuity with present literature, where a repetition rate of 1 kHz was invariably employed, we decided to start with a repetition rate of 50 kHz, with the purpose of achieving higher writing speeds. The other parameters, most importantly the writing speed and the pulse energy, were subject to a thorough optimization process which we shall describe in the following.

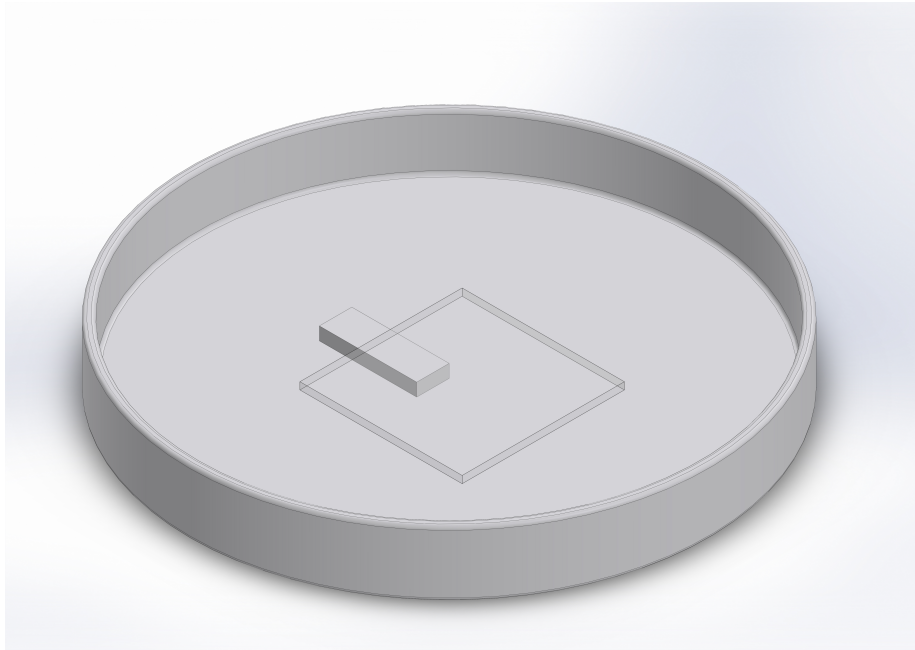


FIGURE 5.1: Picture of the sample-mount setup. A small holder is glued to the bottom of the Petri dish, and the sample is glued on top of the holder by one of its sides.

### 5.1.1 Sample mount and water supply

In our setup, the laser beam is focused from above, as represented in FIG. 3.1, so the ablation needs to start from the bottom surface, where we have to bring water in contact. Water supply has been performed in literature with several different geometries, both statically and dynamically. A dynamic supply, where a specific pumping system is implemented to create a constant flux of water, is particularly suitable for setups where the sample is still and the laser beam is moved.

In our setup, where the sample is moving, having a pumping system attached to a moving part would be rather impractical, so we opted for a simpler static supply.

We used a common Petri dish with a diameter of 60 mm. We glued a small piece of spare glass, about 2 mm thick, to the bottom of the dish, to use it as a holder for our sample. The sample was then glued on top of the holder overhanging by one of its side, as shown in FIG. 5.1. We typically managed to mount it with an overlap on the holder of about 5 mm, which left most of the bottom surface free for micromachining, considering that the sample overall dimension in the horizontal plane was 25 mm × 25 mm. The Petri dish was then

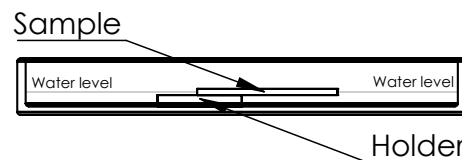


FIGURE 5.2: Schematic of the sample-mount setup. After the holder and sample are properly glued, water is slowly poured until it reaches the bottom surface of the sample, as displayed in figure.

mounted on the motion stages. We should point out that a firm and steady gluing of holder, sample and dish is fundamental to avoid movements during the fabrication, especially due to the acceleration of the stages.

Once the dish is mounted on the stages and all alignment procedures are completed, we slowly pour water into the dish until reaching the bottom surface of the sample, as schematized in FIG. 5.2. This operation is performed while carefully avoiding to spill water on the top surface, as it would cause undesired refractions and aberrations of the laser beam, which we need instead to cross the top surface and the whole thickness of the sample as cleanly as possible. Once water touches the bottom surface, it uniformly adheres to the sample and forms a meniscus along its sides. This has turned out to be beneficial, as it prevents water from slipping over the top surface when the motion stages perform significant accelerations.

### 5.1.2 Trenches

Optimizing the technique requires to have a benchmark for the comparison of structures written with different irradiation parameters. We chose to compare our results on an elementary *trench* structure, i.e. a structure fabricated with the irradiation pattern displayed in FIG. 5.3. Starting from the bottom surface, which is in contact with water, we irradiated straight horizontal lines one on top of each other, separated by a step  $\Delta h$  up to a total irradiation height  $H$ . While  $\Delta h$  was varied to study the effect of different pitches,  $H$  was kept constant to  $400\ \mu\text{m}$ . However, when the debris formed during the irradiation is not ejected correctly, it can stack into the crack and prevent water from flowing into the trench, thus stopping the ablation before the full height of  $400\ \mu\text{m}$  is reached. The ablated height can be accurately measured by observing the machined sample from its lateral facets with the optical microscope.

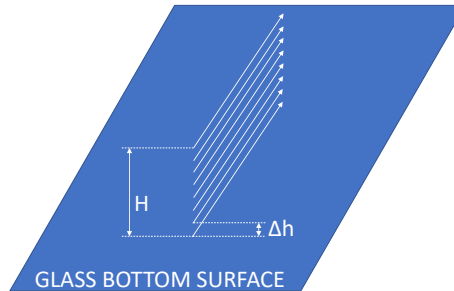


FIGURE 5.3: Schematic of the irradiation pattern for the ablation of a trench.

**Starting z-coordinate.** During the alignment procedure, we set the  $z = 0$  reference plane on the bottom surface of the sample. As a safe initial assumption, we decided to start all ablation processes from a negative z-coordinate to make sure that the bottom surface was correctly ablated. In the case of trenches, this means that the first irradiation lines were focused in water, rather than in glass. Our first fabrications were performed with an initial  $z = -28\ \mu\text{m}$  coordinate. However, a microscope inspection of the ablated structures revealed that the bottom surface was not fully ablated, displaying instead a peculiar pattern of almost periodically ablated and non-ablated features (see FIG. 5.4). We then decided to perform an optimization of the starting z-coordinate, obtaining the results displayed in FIG. 5.5. At  $z = -28\ \mu\text{m}$  we found the behaviour just described, while for lower initial coordinates the surface was fully ablated and

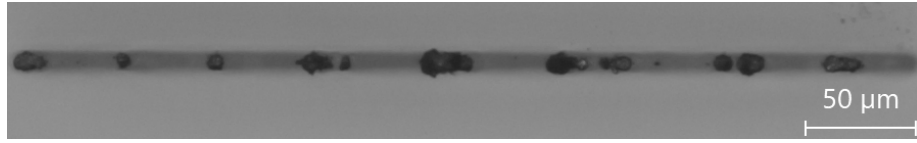


FIGURE 5.4: *Bottom view* of a trench ablated with  $z_0 = -28 \mu\text{m}$ . The surface shows a peculiar pattern of ablated and non-ablated regions.

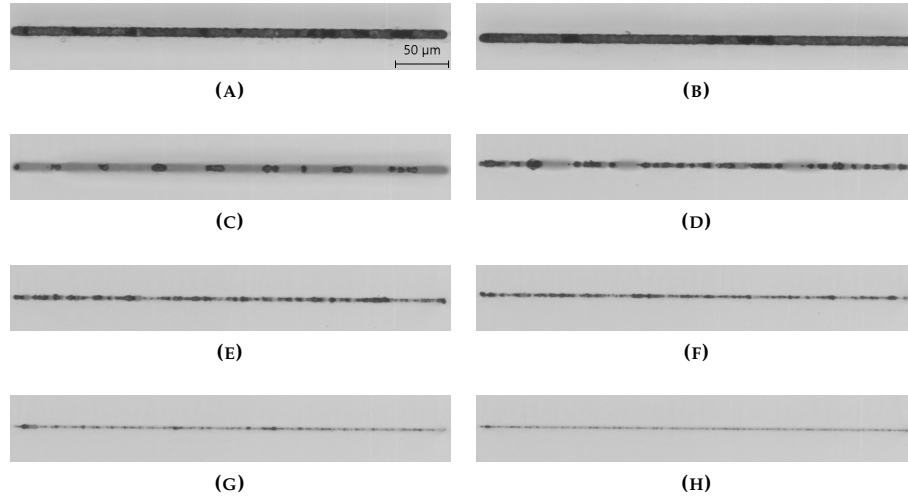


FIGURE 5.5: Study of the bottom surface of the trench with different starting  $z$ -coordinates. (A)  $z_0 = -100 \mu\text{m}$  (B)  $z_0 = -60 \mu\text{m}$  (C)  $z_0 = -28 \mu\text{m}$  (D)  $z_0 = -16 \mu\text{m}$  (E)  $z_0 = -8 \mu\text{m}$  (F)  $z_0 = -4 \mu\text{m}$  (G)  $z_0 = -0 \mu\text{m}$  (H)  $z_0 = 4 \mu\text{m}$ .

for higher initial coordinates the ablation was not started at all. The fact that we first see a complete bottom surface ablation when starting at  $z = -60 \mu\text{m}$ , apparently suggest that the focal point is somewhat "higher" than we expect it to be. This might be the result of a self-focusing mechanism, which has been often reported in FLM and causes the laser beam to focus *before* the actual focal length of the objective. Such phenomenon is strongly nonlinear, and this may be the reason why it does not take place during the alignment procedure, which is performed at very low intensities, but only during fabrication. This hypothesis is consistent with other results displayed further in this chapter.

**Pulse energy, writing speed and pitch.** These three quantities are the most relevant writing parameters for our structures. We fabricated a set of about 60 trenches to explore a subset of the space defined by these quantities. Specifically, we tested pulse energies ranging from 0.5 to 5  $\mu\text{J}$ , writing speeds ranging from 0.5 to 4  $\text{mm s}^{-1}$ , and  $\Delta h$  ranging from 1 to 4  $\mu\text{m}$ . For each trench, we measured the height of the ablated region, which is clearly distinguishable by microscope inspection (see FIG. 5.6), as already shown in [92]. For pulse energies lower than 1.5  $\mu\text{J}$  the ablation did not even start. For energies between 1.5 and 5  $\mu\text{J}$  our results are collected in the graphs of FIG. 5.8. With all pulse energies, the total ablated height evidently decreases with increasing  $\Delta h$ . This is reasonable,

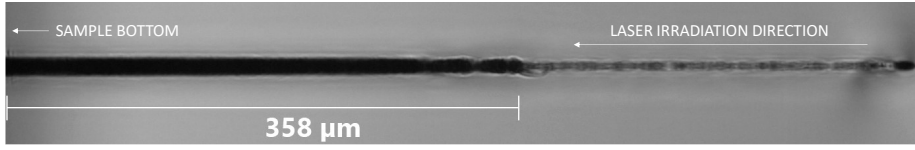


FIGURE 5.6: Side view of the trench with measurement of the ablated height.

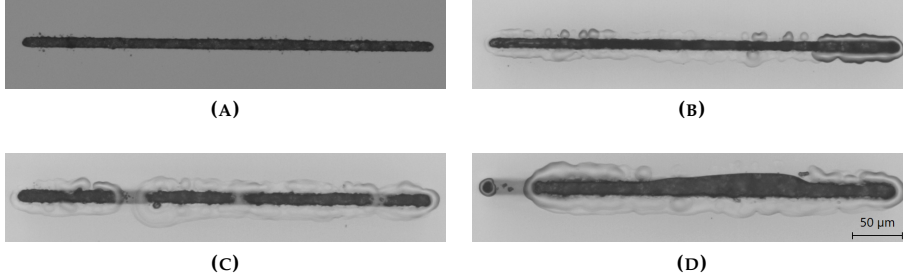


FIGURE 5.7: Bottom view of trenches ablated with different pulse energies. (A)  $E_p = 3 \mu\text{J}$  (B)  $E_p = 5 \mu\text{J}$  (C)  $E_p = 9 \mu\text{J}$  (D)  $E_p = 15 \mu\text{J}$ .

considering that a larger  $\Delta h$  implies the formation and removal of larger debris at each successive ablation line. At the same time, the ablated height evidently increases with the pulse energy, which is reasonable as the formation of higher energy plasma increases the probability of the material being correctly ejected. Finally, the dependence on the writing speed is less prominent but, once again, higher writing speeds seem to make the ablation less efficient, particularly in the  $5 \mu\text{J}$  energy range.

In order to have the ablation process as efficient as possible, it would seem reasonable to choose as the optimal set of writing parameters the only one that proved able to ablate the full  $400 \mu\text{m}$  irradiated height, i.e.  $E_p = 5 \mu\text{J}$ ,  $v_{\text{writing}} = 0.5 \text{ mm s}^{-1}$ ,  $\Delta h = 1 \mu\text{m}$ . However, the surface quality of the ablated structures must be considered as well. Specifically, we would like to ablate features with clean, sharp sides and without causing damage to the surrounding areas. As FIG. 5.7 clearly shows, pulse energies higher than  $3 \mu\text{J}$  lead to evident thermal modifications in the regions close to the bottom of the trench. As a result, we chose to perform the following ablation experiments with  $E_p = 3 \mu\text{J}$ ,  $v_{\text{writing}} = 0.5$  or  $1 \text{ mm s}^{-1}$  and  $\Delta h = 1 \mu\text{m}$  as our main reference parameters.

**Further insights.** Once a first, functional set of the main fabrication parameters was found, we explored the effects of other variables in the ablation process.

We first wanted to determine whether the apparent decrease in ablation efficiency for higher writing speeds and higher  $\Delta h$  was due to the intrinsic phenomena involved in the ablation process, i.e. the proper formation and ejection of debris, or due to the fact that water could not flow into the crack and reach the ablated zone quickly enough. Indeed, if a trench of a given height is ablated with a larger  $\Delta h$  between one scan and the other, the total height of the trench will be reached in shorter time or, in other words, the ablation process will have a higher *vertical* speed. The same is true for a higher writing speed,

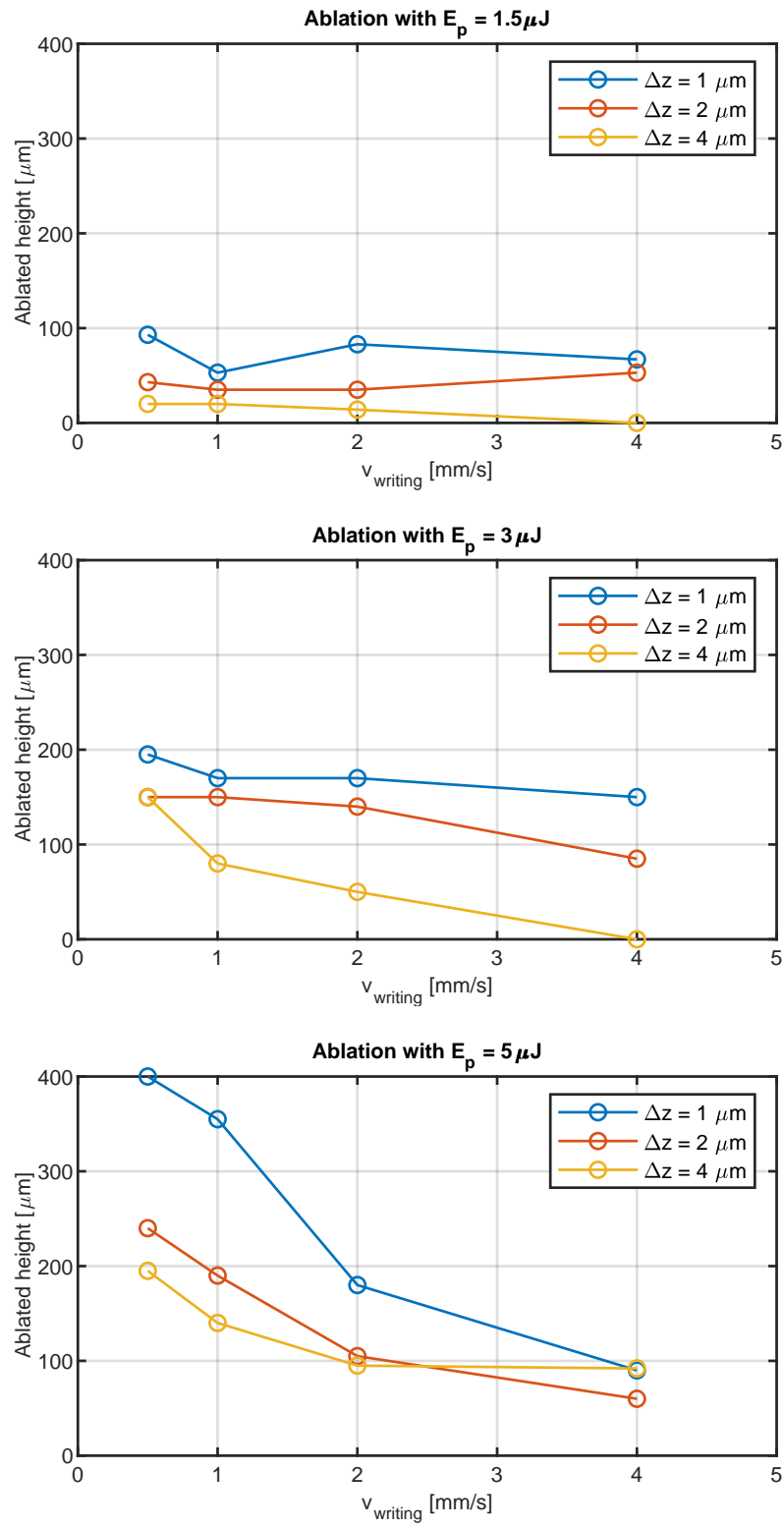


FIGURE 5.8: Dependence of the ablated height on writing speed, pulse energy and  $\Delta h$ .



which allows to perform each scan in a shorter time, therefore also increasing the vertical speed of ablation, and a higher vertical speed might cause water not to reach the ablated area. Should that be the case, introducing a dwelling time (i.e. a pause of given duration  $t_{\text{dwell}}$  between successive ablation lines) would increase the efficiency of process and would yield taller trenches. In a first experiment, we increased  $\Delta h$  and  $t_{\text{dwell}}$  accordingly, in such a way to keep the *vertical* speed constant. In a second experiment, we kept instead  $\Delta h$  constant, and increased  $t_{\text{dwell}}$  so to *decrease* the vertical speed. In both cases, the presence of dwelling time proved to be completely insignificant, as the ablated height kept decreasing with  $\Delta h$  regardless of the dwelling. This confirms the results already shown in [91].

We then fabricated trenches tilted by different angles  $\vartheta$  with respect to the vertical direction. This was done by adding a lateral step  $\Delta y = \Delta h \tan(\vartheta)$  between each successive scan. As  $\vartheta$  increased, the vertical height of the trenches decreased, but the length of the ablated track remained approximately constant, showing no particular correlation with  $\vartheta$  up to  $\vartheta = 60^\circ$ . This is positive for us, as it indicates that, if a given set of parameters proves able to ablate, for instance, a 200  $\mu\text{m}$  tall vertical trench, we can expect it to also ablate an approximately 200  $\mu\text{m}$  long tilted trench. This provides a good geometrical flexibility to the technique.

To test our initial hypothesis that what prevents the process from reaching larger ablation heights is the clogging of debris inside the crack, we tried to ablate thicker trenches, assuming that a thicker trench would favour the ejection of debris and the flowing of water. The trenches were realized by performing multiple ablation scans on the *same* horizontal plane, separated by a distance  $\Delta y$ , before moving up by  $\Delta h$ . An example of the irradiation pattern with 2 scans is schematized in FIG. 5.9. We explored different numbers of scans and different values of  $\Delta y$ . Values of  $\Delta y$  larger than 4  $\mu\text{m}$  resulted in visibly separated trenches and proved inefficient to ablate higher structures. For  $\Delta y$  equal or smaller than 4  $\mu\text{m}$ , instead, increasing the number of scans, i.e. the thickness of the trench, resulted in taller trenches, as foreseen. As an example, we show in FIG. 5.10 that a trench realized with 3 scans per plane, separated by  $\Delta y = 4 \mu\text{m}$ , was ablated up to the full irradiated height of 400  $\mu\text{m}$  when using  $E_p = 3 \mu\text{J}$ ,  $v_{\text{writing}} = 0.5 \text{ mm s}^{-1}$ ,  $\Delta h = 4 \mu\text{m}$ . The same parameters had previously yielded a single-scan trench only 150  $\mu\text{m}$  tall.

As a final experiment, we decided to explore higher repetition rates, which may allow to employ higher writing speeds. Specifically, we fabricated a set of trenches where the repetition rate and the writing speed were increased accordingly to keep constant the number of pulses (i.e. the energy deposited) per unit length, which is what supposedly determines most of the ablation properties. As an example, if we chose to write at  $0.5 \text{ mm s}^{-1}$  with 50 kHz, we would write at  $1 \text{ mm s}^{-1}$  with 100 kHz, and so on. However, we found that at higher writing speeds the ablated height was invariably lower, and at 200 kHz

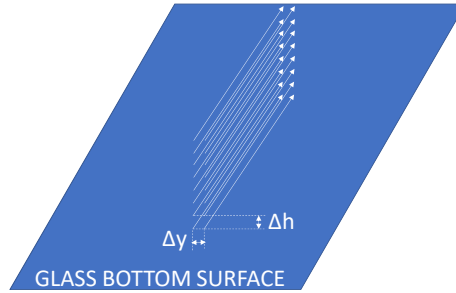


FIGURE 5.9: Schematic of the irradiation pattern for the ablation of a trench.

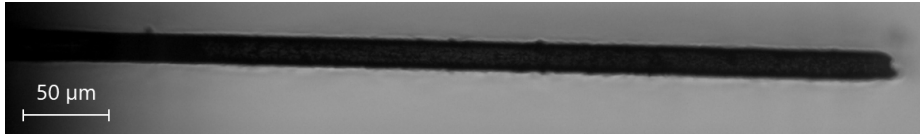


FIGURE 5.10: Side view of a trench ablated with 3 scans per plane, separated by  $\Delta y = 4 \mu\text{m}$ .

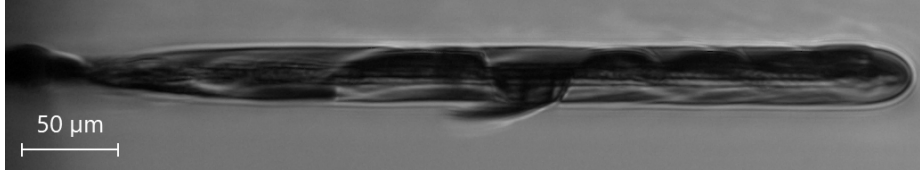


FIGURE 5.11: Side view of a trench ablated with 200 kHz repetition rate. The whole structure was evidently melted.

the area surrounding the trench was melted, as shown in FIG. 5.11. Thermal effects due to high repetition rates seem thus detrimental in our process. As a result, we decided to keep the repetition rate of 50 kHz and the writing speed of  $0.5$  to  $1 \text{ mm s}^{-1}$  as standard parameters for all successive fabrications. This writing speed is much higher than most literature has shown up to now, and is only comparable to the one employed in [95] and [94] where, however, a picosecond laser was employed.

### 5.1.3 Boxes

As a next study, we investigated the ablation of rectangular boxes, using the same idea presented in [95], that is to remove significant volumes of material by ablating their sides and letting them detach, rather than ablating the full volume. A schematic of the irradiation pattern displayed in FIG. 5.12. As irradiation parameters, we adopted  $E_p = 3 \mu\text{J}$ ,  $v_{\text{writing}} = 0.5 \text{ mm s}^{-1}$ ,  $\Delta h = 1 \mu\text{m}$ , as optimized with the study of trenches presented in the previous paragraph.

After being ablated, the boxes need to detach from the substrate. In order

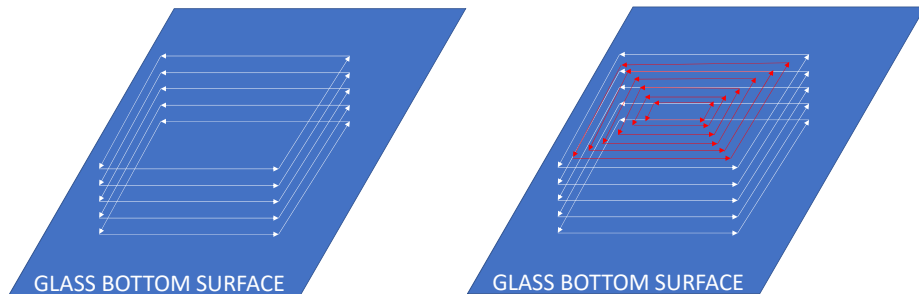
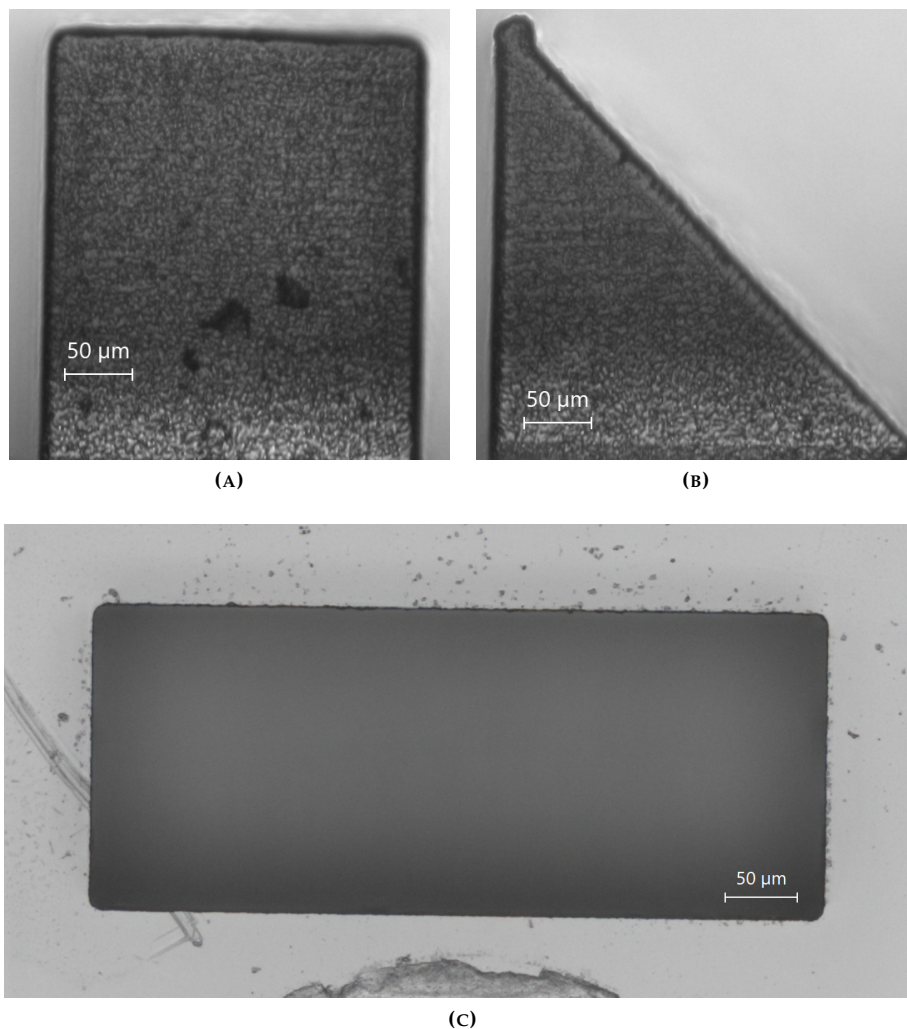


FIGURE 5.12: Irradiation pattern for the ablation of a rectangular box. First, the sides of the box are ablated by performing circular patterns with steps  $\Delta h$ . Last, the top of the box is ablated by shrinking the patterns until reaching the center.

to facilitate the detachment, we decided to fabricate them with one side tilted by some angle  $\theta$  with respect to the vertical. We explored boxes 100 and 200  $\mu\text{m}$  tall, 100 and 200  $\mu\text{m}$  wide, 500  $\mu\text{m}$  long, and with  $\theta$  ranging from 0 (i.e. straight walls) to  $45^\circ$ . All the boxes detached perfectly, and we were thus able to demonstrate a full range of geometries, from the perfectly rectangular box, to a box with a  $45^\circ$  tilted side which resulted in a triangular wedge. These two examples are shown in FIG. 5.13.



**FIGURE 5.13:** (A) *Side view* of a 200  $\mu\text{m}$  tall rectangular box. (B) *Side view* of a 200  $\mu\text{m}$  tall triangular wedge. (C) *Bottom view* of a rectangular box with horizontal cross-section of 200  $\mu\text{m} \times 500 \mu\text{m}$ .

Boxes taller than approximately 250 - 300  $\mu\text{m}$  proved more difficult to ablate and detach, as the ablation would often stop before completing the full pattern. We qualitatively distinguished two types of failure: width-limited and height-limited. In width-limited failures, the sides of the box were totally ablated, but

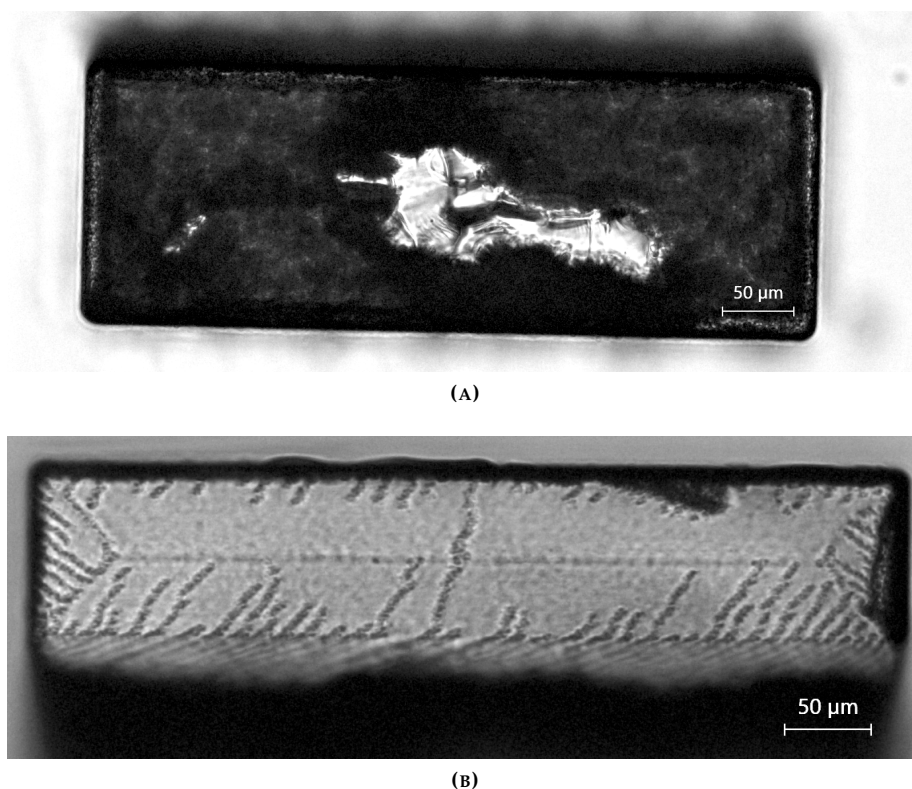


FIGURE 5.14: *Top view* in transmission mode. (A) The top part is ablated except for a small area. (B) The top part was not ablated because water was unable to reach the full height of the box.

the top part was not completely "closed", as in the example of FIG. 5.14A. In these cases, which typically happened for boxes lower than  $300\ \mu\text{m}$ , we often found that, even if the box was not initially detached, it would easily detach after few minutes in the ultrasound cleaner without showing visible damage to the side walls. In height-limited failures, instead, the ablation stopped before reaching the top surface. This limitation was analogous to the one found for trenches, and this type of failures typically happened for boxes taller than  $300\ \mu\text{m}$ . An example is reported in FIG. 5.14B. Here, the supposed height of the box was  $400\ \mu\text{m}$ , which we knew from the trenches experiment to be most likely out of reach with the chosen irradiation parameters. The ablation was indeed unable to reach the top part of the box, which consequently remained attached to the substrate.

A more quantitative analysis of the circumstances associated to failed ablations revealed that boxes were not fully ablated when the sum of the vertical and the horizontal path (where the horizontal path corresponds to half of the box's width, since the top part is ablated from both directions) were longer than about  $350\ \mu\text{m}$ . However, given the same overall path, boxes low and wide proved generally easier to ablate than boxes tall and slim.

Finally, with the purpose of ablating taller boxes, we tried to stack multiple boxes one on top of each other. We supposed that if what actually stops the

ablation is the presence of debris blocking the water flow, removing a full portion of material should allow the ejection of all debris and water should be able to completely fill the gap, so that ablation can then restart from a clean surface. This method showed indeed very good results, and we were able to fabricate a fully ablated 600  $\mu\text{m}$  tall box, realized in 4 steps of 150  $\mu\text{m}$ . The result is shown in FIG. 5.15. Multi-step boxes can also be useful to ablate more reliably boxes that would be within the limit of single-step ablation, having as an only downside a slight increase in fabrication time and some minor surface imperfections at the conjunction planes.

#### 5.1.4 Horizontal ablation

At this stage, the only significant geometrical feature we are missing for being able to fabricate a cantilever is the horizontal ablation. The main problem with horizontal ablation is that, as opposed to what we have done up to this point, it is not possible to just ablate the sides and let a portion of material detach, because an obstacle of intact material is present underneath it, so it cannot "fall" like the boxes normally do. As a first trial, we then decided to ablate the horizontal region by irradiating the full volume, i.e. by closely stacking a fine pattern of lines until the whole volume is covered. In detail, we fabricated two simple rectangular boxes close to each other and then tried to connect them by the top with an horizontal ablation region. This produces a U-shaped ablated pattern, and what remains is a bridge-like structure. The results were very encouraging, as we were able to produce structures with a wide range of geometries, of which we show two examples in FIG. 5.16.

The method seemed very reliable and repeatable, and resulted in a very clean horizontal region. However it presented some downsides. First, as can be seen in FIG. 5.17, the horizontal ablated region was not perfectly rectangular because of the opening and closing delays of the mechanical shutter. This can be solved by some simple re-design of the irradiation pattern. Second and more importantly, fabricating four structures took more than ten hours. This is because volume ablation requires to perform a dense pattern of ablation lines and is therefore severely time consuming. To overcome this issue, we then started considering to remove the horizontal region by breaking it into pieces, rather than ablating the full volume. The problem is making sure that the pieces can fall off laterally and free the region, which is clearly easier with structures that have shorter horizontal regions. We explored two different irradiation patterns. In the first, we subdivided the region in rectangles, each one ablated with a pattern similar to that of FIG. 5.12. In the second, we subdivided it into triangular prisms which, having tilted surfaces, should favour the falling of the detached pieces. We found that both pattern were able to successfully ablate

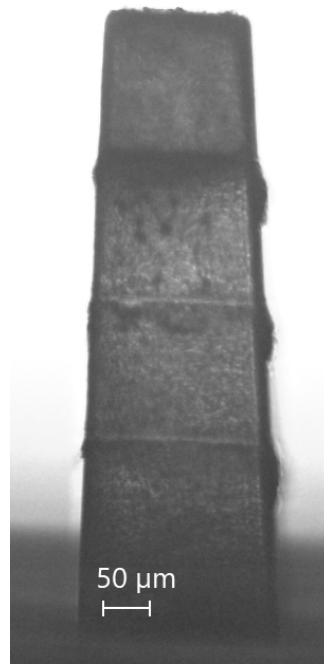


FIGURE 5.15: Side view of a 600  $\mu\text{m}$  tall box realized in 4 steps.



a 100  $\mu\text{m}$  wide horizontal region. However, the rectangular pattern showed slightly better surfaces and took less time, so we decided to employ it in the next fabrications.

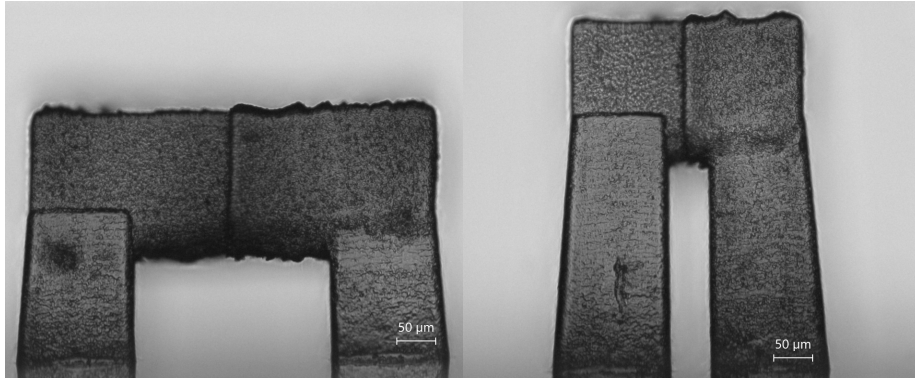


FIGURE 5.16: *Side view* of U-shaped ablation structures with different geometries.

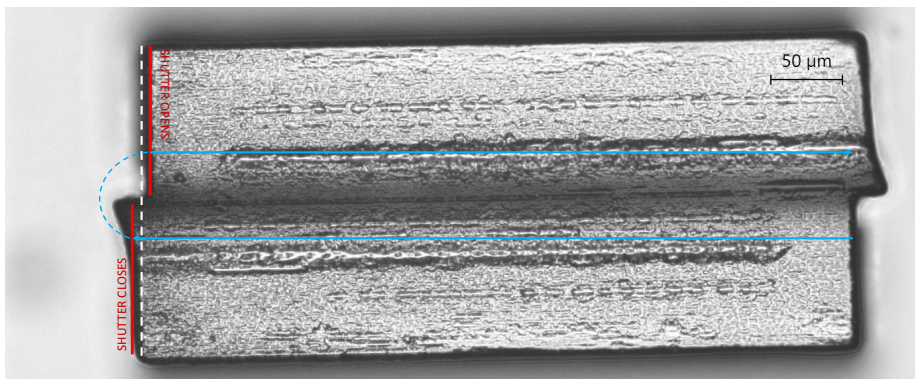


FIGURE 5.17: *Top view* of the U-structures. The ablation was performed by irradiating the two halves of the box in opposite directions (light blue line), connecting them by an external arc. The white dashed line represents the ideal point of opening and closure of the shutter. However, a mechanical delay is present, such that the shutter closes slightly late and re-opens slightly late. This results in a slight displacement of the two halves, which is worse around the centre line, where the re-opening follows the closure very quickly.

### 5.1.5 Bubbles

From our very first experiment, we have witnessed the formation of several vapour bubbles below the sample. These bubbles are persistent, meaning they do not re-condense, but remain stuck below the surface of the sample for several hours, even after the irradiation process is completed.

We have observed that the formation of large bubbles is an incremental process. During the first minutes of fabrication, microscopic bubbles are formed around the region of irradiation and tend to be pushed laterally, towards the

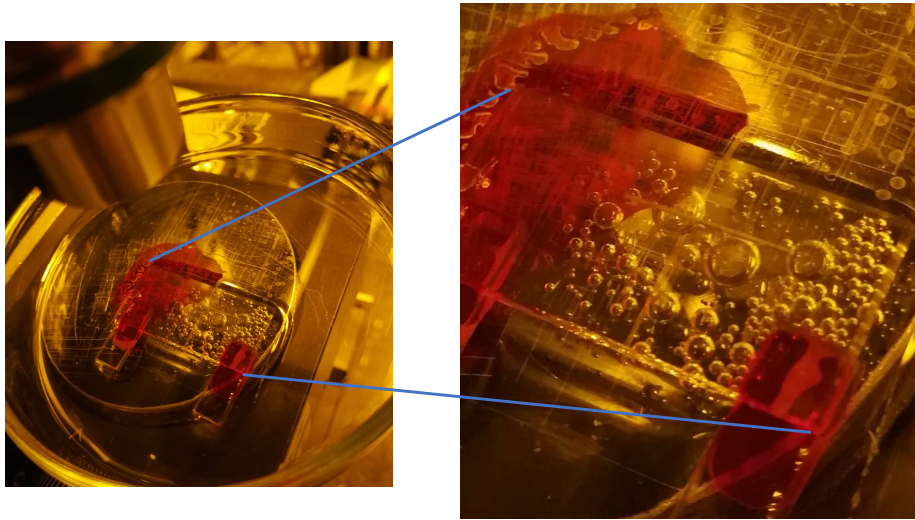


FIGURE 5.18: Macroscopic persistent vapour bubbles formed during the fabrication.

sides of the irradiated area, forming a pattern that is visually similar to a fine foam. However, as the ablation process goes on, they seem to unify into larger bubbles which, within a time frame of about one hour, acquire visible dimensions, with diameters in the order of millimetres. An example of this stage is reported in FIG. 5.18.

The problem with bubbles is that they interrupt the contact between water and glass, so they can cause the ablation to stop. As mentioned, bubbles tend to be pushed away from the irradiated region, so they do not usually represent a problem for the ablation of a single feature. On the other hand, they can be detrimental when performing the ablation of several structures in different areas of the sample, as it can randomly happen to start an ablation within the area of a bubble, in which case the ablation will not start, as happened with the structure shown in FIG. 5.19.

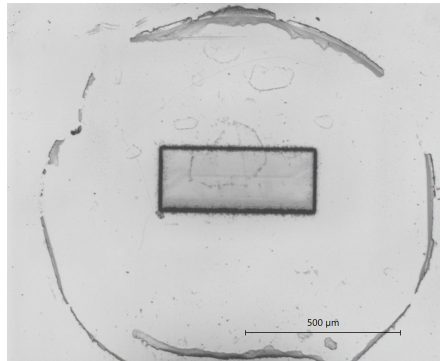


FIGURE 5.19: *Bottom view* of a failed ablation due to the formation of a bubble.

As a matter of fact, the formation of shock waves and cavitation bubbles is a well-known effect of laser-induced optical breakdown in water. According to most authors, this is also the reason why water-assisted ablation is much more efficient than "dry" ablation, as it helps at the same time to create and remove the debris. However, cavitation bubbles are a transitory phenomenon and collapse very quickly. The formation of macroscopic, persistent bubbles has not generally been reported. We may speculate that this phenomenon is linked to the fact that we are using a 50 kHz repetition rate, rather than the "usual" 1 kHz. With a 50 kHz repetition rate, pulses are separated by a time interval

of 20  $\mu\text{s}$ . If this time interval is comparable to the collapsing time of cavitation bubbles, then an additive effect might take place and lead to the formation of macroscopic bubbles. Indeed, both [99] and [100] studied the dynamics of femtosecond-lase induced cavitation bubbles in water, and reported a collapsing time in their order of 10  $\mu\text{s}$  for a pulse energy of 1  $\mu\text{J}$ .

To fully address this phenomenon some further investigation should be performed, which is beyond the scope of this work. A dynamic water supply would probably mitigate the problem, as bubbles would be brought away as soon as they form and they would probably not grow in size as they do in our case. Within the fabrications presented in this work, we simply dealt with the problem knowing that it can represent a small, random probability of failure.

## 5.2 The cantilever

At this point, all the basic elements are ready for the realization of the cantilever structure, which is essentially a bridge with a cut on one side. In principle, the cut could be realized by simply ablating a trench. However, even when the trench is correctly ablated, we have found that some material tends to remain stuck inside it, so we preferred to perform the cut as a narrow box, with the usual irradiation pattern of FIG. 5.12. We fabricated four cantilevers with  $l = 1 \text{ mm}$ ,  $t = 50 \text{ }\mu\text{m}$  and  $w = 250 \text{ }\mu\text{m}$ , as designed in Sect. 4.3. The width of the extremity cut was set at 50, 30, 15 and 10  $\mu\text{m}$ . All cantilevers were correctly ablated, so all the subsequent cantilever were fabricated with an extremity cut of 10  $\mu\text{m}$ . The results are shown in FIG. 5.20. FIG. 5.21 shows instead a side view of one of these cantilevers.

From the bottom view images, a high cleanliness and precision of the cuts is observable. On the other hand, the side view shows that horizontal surfaces (i.e. the top part of the cantilever) tend to have a much worse quality than vertical surfaces. These was foreseen and discussed in Sect. 4.3, and is connected to the asymmetry of the nonlinear interaction region.

What we also want to emphasize is that, whereas the horizontal dimensions of the cantilever are as designed within an accuracy of few micrometres (see FIG. 5.20), the vertical dimensions of our structure are slightly larger than expected by about 30  $\mu\text{m}$  (see FIG. 5.21). Specifically, the resulting width of the cantilever is about 280  $\mu\text{m}$  instead of the designed 250  $\mu\text{m}$ , and the depth of the cavity is 330  $\mu\text{m}$  instead of the designed 300  $\mu\text{m}$ . A similar effect was also reported in [94]. Our hypothesis is that this behaviour is linked to the same phenomena we reported in Sect. 5.1.2 when discussing the starting z-coordinate. It is possible that a combination of self-focusing and aberration effects is present and causes the nonlinear interaction region to take place *before* the actual focal point of the objective. As a result, the ablation always happens at a higher point than we encode in the control software, so our ablated features result slightly "taller". Furthermore, both aberrations and self-focusing depend on the fabrication depth. Taller structures are closer to the top surface, so the laser beam crosses a smaller portion of substrate, therefore the effect is less prominent. This is evident in FIG. 5.15, where the last step looks visibly shorter than the first, despite being equally coded at software level. As a result, the problem of taller structures cannot be solved by simply adding a negative vertical offset in the code.



In conclusion, this is a further proof the designing our cantilever for in-plane oscillation was a correct choice, because neither the surface imperfections nor the mismatch of the dimensions have any effect on the static and dynamic behaviour of the structure. As a matter of fact, having a cantilever 280  $\mu\text{m}$  rather than 250  $\mu\text{m}$  wide is completely equivalent from a practical point of view.

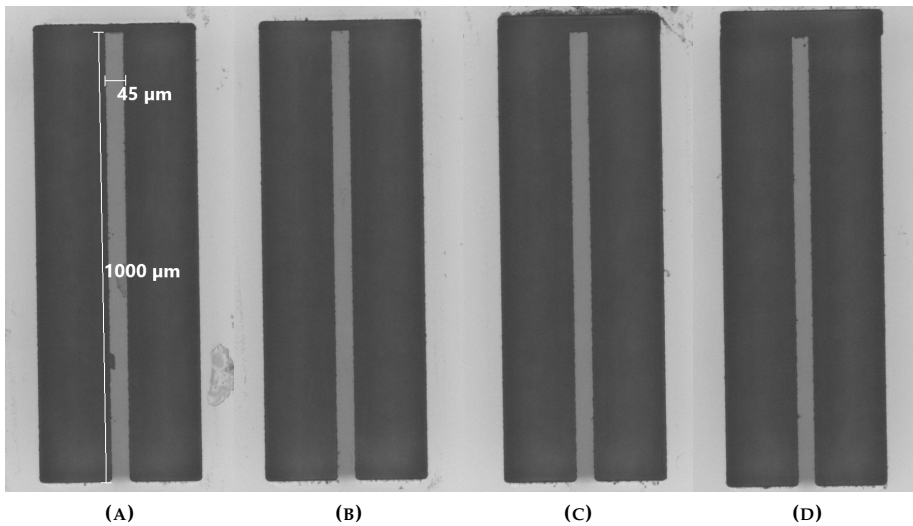


FIGURE 5.20: *Bottom view* of cantilevers with an extremity cut of 10, 15, 30, 50  $\mu\text{m}$ .

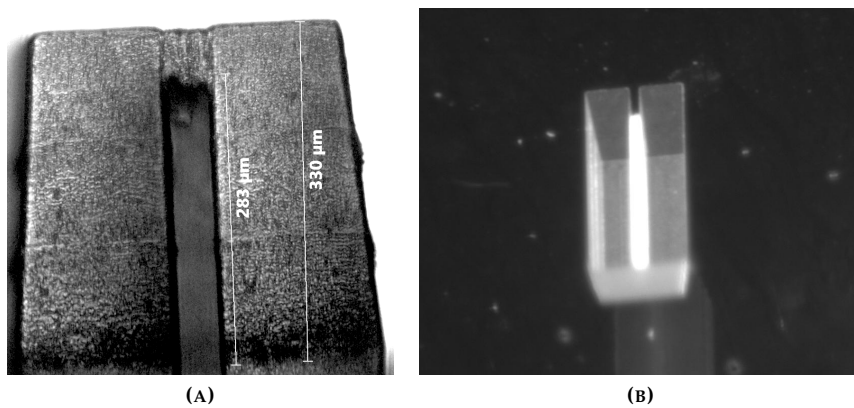


FIGURE 5.21: (A) *Side view* of a cantilever. Notice that the horizontal surface has a worse quality than vertical surfaces. Also notice that the vertical dimensions are slightly larger than designed. (B) Photograph with macro objective.

Once the first set of cantilevers was produced, we fabricated several more in successive experiments. We varied the length while keeping the thickness and width constant, and we successfully demonstrated a range from 0.5 mm to 2 mm, which are reported in FIG. 5.22 as example. In a subset of these cantilevers we integrated the waveguide, as discussed in the next paragraph.

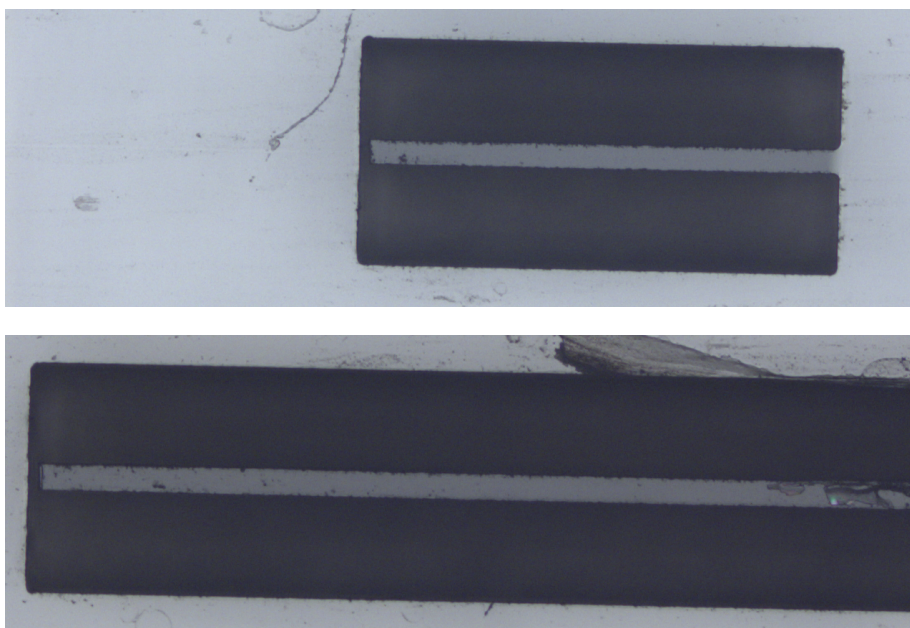


FIGURE 5.22: *Bottom view* of two cantilevers with lengths of 0.5 mm and 2mm respectively. The second one does not fit into a single image.

### 5.3 The waveguide

The properties and performances of FLM written waveguides are highly sensitive to all irradiation parameters. Extensive literature exists on waveguides written in borosilicate at different repetition rates. Our case, however, has several peculiarities given by the fact that we want to write a waveguide inside the cantilever within a *single* fabrication, rather than performing the work in two or more steps. The main reason for this, besides the obvious purpose of time saving, is that the alignment of all structures, and particularly the relative alignment of waveguide and cantilever, can be reproduced with much greater accuracy.

As an immediate consequence, since the cantilever is ablated from the bottom surface, our waveguides need to be written at a considerable depth from the top surface, which is an uncommon condition for waveguide writing. In order to have the waveguide passing approximately along the center of the cantilever, we decided to write it at  $150\ \mu\text{m}$  from the bottom surface. We will write the waveguide using the same 20x Achromatic objective employed for ablation, since exchanging the objective would imply re-performing the alignment procedure.

Finally, we should consider the repetition rate. Eaton *et al* [44] showed that waveguide writing in borosilicate benefits from heat accumulation effects due to high repetition rates, particularly above 200 kHz, with 1 MHz as the optimum parameter. In our case, the 50 kHz needed for ablation are achieved by setting the internal repetition rate of the laser to 200 kHz and the pulse picker to 4. While the pulse picker can be changed on-the-run, changing the internal repetition rate requires to switch off the laser, which then requires at least one hour to reach again stable operation. Consequently, as a mere matter

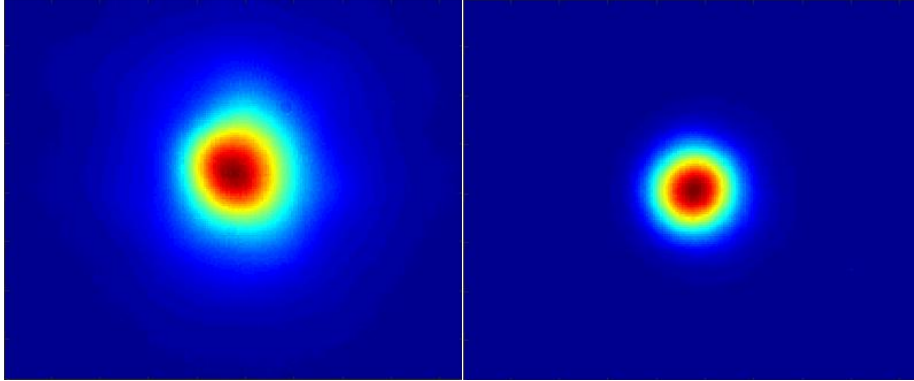


FIGURE 5.23: Comparison between waveguide mode (left) and fiber mode (right). The waveguide mode has  $\sigma_x = 7.5 \mu\text{m}$  and  $\sigma_y = 8 \mu\text{m}$ .

of practicality and of time-saving in the fabrications, we decided to write our waveguides with a repetition rate of 200 kHz.

Following the reference work of [44], we chose to optimize our waveguides for an input wavelength of 1550 nm. We fabricated a set of about 70 waveguides with pulse energies ranging from 0.1 to 2  $\mu\text{J}$  and writing speeds from 2 to 20  $\text{mm s}^{-1}$ . The best single mode waveguide was achieved with  $v_{\text{writing}} = 2 \text{ mm s}^{-1}$  and  $E_p = 1.54 \mu\text{J}$ . The acquired image of the mode is displayed in FIG. 5.23 against the fiber mode. The mode is almost circular and its measured dimensions are  $\sigma_x = 7.5 \mu\text{m}$  and  $\sigma_y = 8 \mu\text{m}$ . Its overlap integral with the fiber mode is about 70%.

Integrating the waveguide in the cantilever is straightforward. We write the waveguide first, in order to avoid any border and aberration effects, then we perform the ablation. This way, the cantilever is practically fabricated "around the waveguide". The only point of intersection between the ablation pattern and the waveguide is the extremity cut of the cantilever. With fiber coupling, we achieved an overall transmission of 16%, corresponding to a total insertion loss of about 7.95 dB. This result is not particularly competitive with respect to most of the literature in borosilicate, but is sufficient for our purpose, so we proceeded and used this waveguide for our subsequent experiments.



## Chapter 6

# Static and dynamic characterization

We experimentally characterized the static and dynamic properties of two cantilevers 1.2 mm and 1.5 mm long. We will refer to them in the following as *Cantilever 1* and 2 respectively. A third cantilever, 730  $\mu\text{m}$  long, was only used in one experiment, as we shall later discuss. We employed an experimental setup conceptually equal to the one of FIG. 3.3. We first pigtailed the input fiber to the sample, in order to have a stable coupling with the lowest possible losses, while the output light was collected with an objective. Both the pigtailling operation and the actual characterization experiment were performed on the hexapods setup (see Sect. 3.3).

### 6.1 Static characterization

#### 6.1.1 Experiment and results

As a first characterization we measured the intensity transmitted by the waveguide through the cantilever as a function of a static displacement applied to its extremity. Applying such displacement with micro- or sub-micrometer precision is a nontrivial problem. In our case, we took advantage of the superior position accuracy of the hexapods. We mounted our sample on the sample stage (see FIG. 3.5) through a specific holder. We then built a simple crane-like structure, which we mounted on the left-side hexapod, to which we attached a thin steel needle, in such a way that the needle was kept at about  $45^\circ$  with respect to the horizontal plane. This allowed us to insert the needle in the lateral apertures of the cantilever and bend it with precise steps of 1  $\mu\text{m}$  (FIG. 6.1) in both directions. The collection objective was mounted on the right-side hexapod and the output of the waveguide was imaged onto the powermeter. Our results are summarized in the graphs of FIG. 6.2

#### 6.1.2 Discussion

Our experimental data show a bell-shaped curve which is compatible with the predictions we discussed in Sect. 4.1, where the transmission was modelled

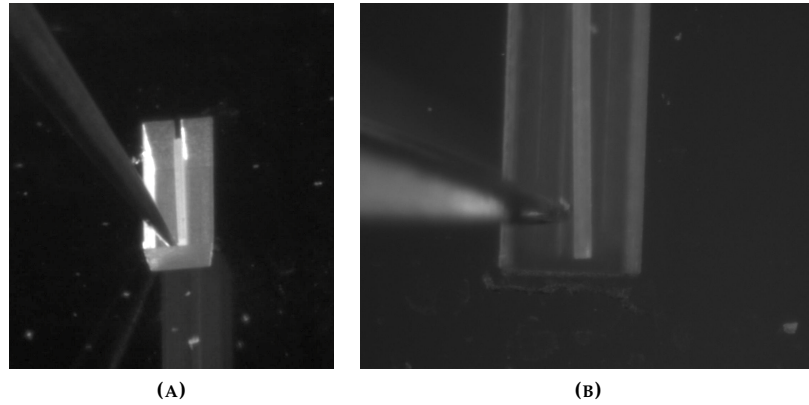


FIGURE 6.1: (A) Photograph with macro objective of cantilever and needle. (B) Microscope image of the needle displacing the cantilever towards the right.

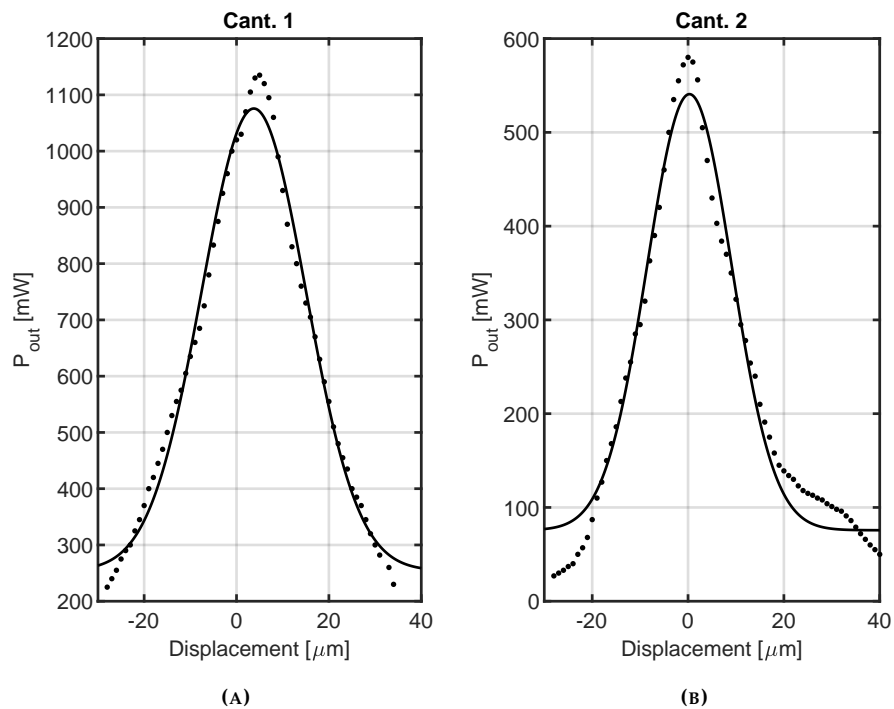


FIGURE 6.2: Transmitted optical power as a function of the static displacement of the cantilever. The dots represent experimental values, while the solid line represents a gaussian fit. (A) Cantilever 1. The fit yields  $\sigma_1 = 11.3 \mu\text{m}$  with  $R^2 = 0.98$ . (B) Cantilever 2. The fit yields  $\sigma_2 = 8.8 \mu\text{m}$  with  $R^2 = 0.97$ .

as the convolution integral of two Gaussian mode shapes, so we expect to find another Gaussian. We then fitted our data with Gaussian curves of the form  $f(x) = A \exp[-(x - x_0)^2 / (2\sigma^2)] + B$ , where  $A$ ,  $x_0$ ,  $\sigma$  and  $B$  are unknown. Both fits do not seem extremely accurate, the first one yielding  $R^2 = 0.98$  and the second one  $R^2 = 0.97$ . However, by extracting the  $\sigma$ -parameter of the Gaussian, they allow us to obtain a rough estimation of the width of the bell and compare it to our theoretical predictions. In detail, the first cantilever yielded  $\sigma_1 \simeq 11.3 \mu\text{m}$  and the second  $\sigma_2 \simeq 8.8 \mu\text{m}$ . Let us now consider the model we described in Sect. 4.1, specifically referring to Eq. (4.6). Comparing the theoretical equation with our fit model the relation  $2\sigma^2 = 4\sigma_x^2$  must hold true, therefore we should expect  $\sigma = \sqrt{2}\sigma_x$  ( $\sigma_x$  is the measured width of the guided mode). We know that  $\sigma_x = 7.5 \mu\text{m}$  after the characterization of our waveguide, therefore we expect  $\sigma = 10.6 \mu\text{m}$ . The first cantilever, with  $\sigma_1 = 11.3 \mu\text{m}$ , seems to closely match the prediction within an error of less than 7%, while the second cantilever, with  $\sigma_2 = 8.8 \mu\text{m}$ , shows an error of about 17%.

The two cantilevers contain identical waveguides, so in principle they should yield the same result in this experiment. We attribute the difference of the two  $\sigma$  to repeatability issues connected to the relative positioning of the needle with respect to the cantilever, which determines how the displacement of the first (which is the one we control through the hexapod) is transmitted to the latter. This is hard to replicate exactly in different experiments. As an example, if the needle touches the cantilever at a point closer to the base, it will induce a larger displacement of the extremity. We have also noticed that the tip of the needle has a tendency to degrade during the experiment because of the contact with the cantilever, becoming more rounded and causing slight drifts in the positioning. Furthermore, the elastic constant of the needle is surely higher than the one of the cantilever, but not infinite, so the displacement we apply to the needle is not identically transmitted to the cantilever. The stiffness of the needle strongly depends on its angle with respect to the surface, the depth at which it was inserted into the lateral aperture (FIG. 6.1) and so on.

What will be more relevant for the subsequent experiments is the observation that the maximum transmitted power for *Cantilever 1* is not at zero-displacement, i.e. its rest position, but is slightly displaced to the right, by approximately  $5 \mu\text{m}$ . This is not an artificial effect produced by our experimental technique, as we have repeatedly displaced the cantilever in both directions and always observed the offset in the same direction. This effect might suggest a misalignment between the two facing extremities of the waveguide at the cantilever's tip. However, the waveguide is written in a single scan, so it cannot be misaligned with itself, and it would also be unreasonable to assume that the ablation process caused the cantilever to be permanently displaced out of its rest position. We therefore attributed this behaviour to some surface imperfection at the extremity cut of the cantilever caused by the ablation process. In detail, it might be linked to scattering or reflections due to surface roughness, or to an actual modification of the extremities of the waveguide during ablation. To surely address the cause of this phenomenon, some further investigation would be needed. The effect did not preclude our subsequent experiment, but it was linked to a peculiar behaviour we observed, which we shall describe in the following section.

## 6.2 Dynamic characterization

To characterize the dynamic response of the cantilever, we replaced the powermeter with an InGaAs photodiode that has a 10 MHz bandwidth (PDA20CS by Thorlabs) and we connected its output to an oscilloscope that has a bandwidth of 200 MHz (Tektronix DPO 2024B). The oscillation of the cantilever translates into an oscillation of the output intensity, which we are able to detect.

### 6.2.1 Time domain characterization

We first tried to characterize the dynamic properties of the cantilever by performing a time domain measurement. Indeed, a linear system is fully characterized by its response to an impulse or to a step. We tried to produce such step using the same setup of the static characterization. We used the needle to displace the cantilever by a given amount, we then lifted the needle vertically so that, when the tip of the needle passed over the side of the cantilever, the cantilever would flip back towards its rest position showing some damped oscillation. In a standard damped harmonic oscillator, free oscillations have the form

$$x(t) = A \exp(-\zeta \omega_0 t) \sin(\sqrt{1 - \zeta^2} \omega_0 t + \varphi) \quad (6.1)$$

where  $A$  is the initial amplitude and  $\zeta$  the damping factor. In our case, this should translate in a damped oscillation of the output intensity with frequency  $2\omega_0$  which, as the cantilever moves back to its rest position, should move back to its maximum. In principle, by properly fitting the resulting curve, we should be able to extract both  $\omega_0$  and  $\zeta$  which, through equation Eq. (1.7), yields the quality factor of our oscillator. In practice, however, the best measurement we managed to extract from this experiment is similar to the one displayed in FIG. 6.3.

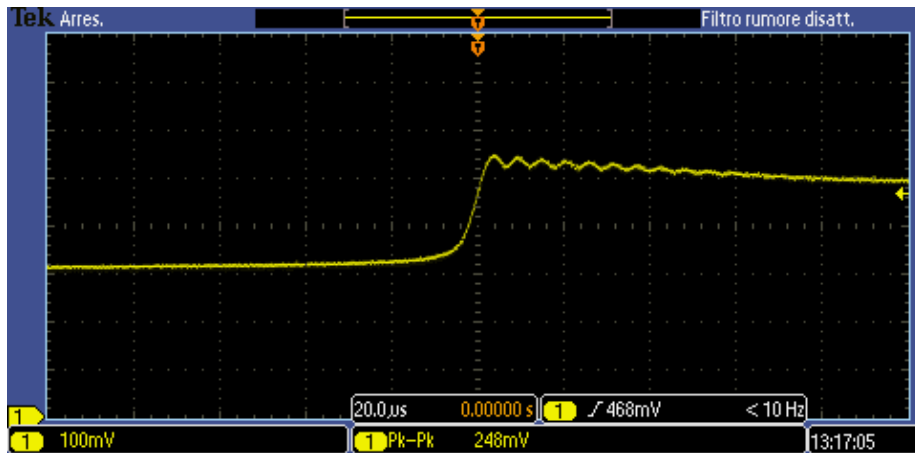


FIGURE 6.3: Result of the impulse response experiment. The intensity shows very small oscillations. The shape of the curve is of difficult interpretation, as an unexpected drift is superimposed to the oscillations.

The curve is of difficult interpretation. We can observe some minute oscillations superimposed to a drift. Overall, the intensity seems to oscillate around a



value different from the one to which it finally settles, and to settle to a value that is not the transmission maximum. Fitting the curve to an analytical function is not feasible, as we are unsure of the physical origin of such behaviour. A direct measurement of the temporal distance between the small peaks showed that the oscillation frequency is of about 90 kHz, which is compatible with the theoretical resonant frequency of about 85 kHz associated to the 730  $\mu\text{m}$  long cantilever tested in this specific experiment. The oscillations, however are too few and too small to allow a good estimation of the damping factor, which is also complicated by the presence of the drift.

In conclusion, we were unable to extract significant information from this experiment and, as a result, we moved to a different characterization method, working in the *frequency domain* rather than in the *time domain*.

### 6.2.2 Frequency domain characterization

For an experiment in the *frequency domain* we need to couple to the cantilever a mechanical oscillation of a given frequency. We decided to employ a commercial piezoelectric plate (PRYY-0111 by PI) driven by a generator (Tektronix AFG3011C) that has a 10 MHz bandwidth and provides a sine wave with 20 V<sub>pp</sub> maximum amplitude. The piezo is a disk with a diameter of 1.5 cm and a thickness of 2 mm. It is designed to have the bias applied to the flat surfaces, so that the electric field acts orthogonally to the surfaces, i.e. along the thickness of the plate. The resulting deformation is parallel to the electric field, as summarized in FIG. 6.4.

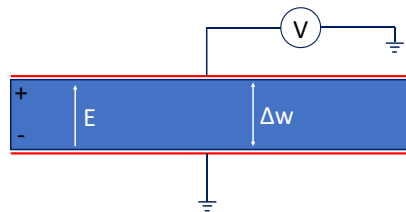


FIGURE 6.4: Schematic of the electrical connections of the piezo and consequent deformation.

We first tried to mount the sample and the piezoelectric plate in the sandwich-like configuration schematized in FIG. 6.5. The sample, with the fiber pigtailed to its back, is leant on an aluminum plate. The piezoelectric disk is positioned on top of it, and they are clamped by an aluminum bar fixed by two screws. Electric contacts to the piezo are provided with two aluminum foils. The whole setup is mounted on the left-side hexapod and the collection objective is mounted on the sample stage. The output of the waveguide is imaged onto the photodiode.

In this configuration, the deformation of the piezoelectric acts vertically, i.e. orthogonally with respect to the sample and the plate. However, because piezo and sample are firmly clamped, some deformation will take place also in the horizontal direction, and the ratio between the two is defined by the Poisson coefficient  $\nu$ . However, the method proved too inefficient and we were unable to detect any visible oscillation of the output intensity. As a matter of fact, the pressure pattern associated to the bending of the cantilever is almost completely localized on the beam and on the immediate surroundings of its base, as clearly shown in the simulations of FIG. 6.7. Therefore any pressure (or equivalent deformation) applied to the whole sample will have a very inefficient coupling with the oscillation mode.

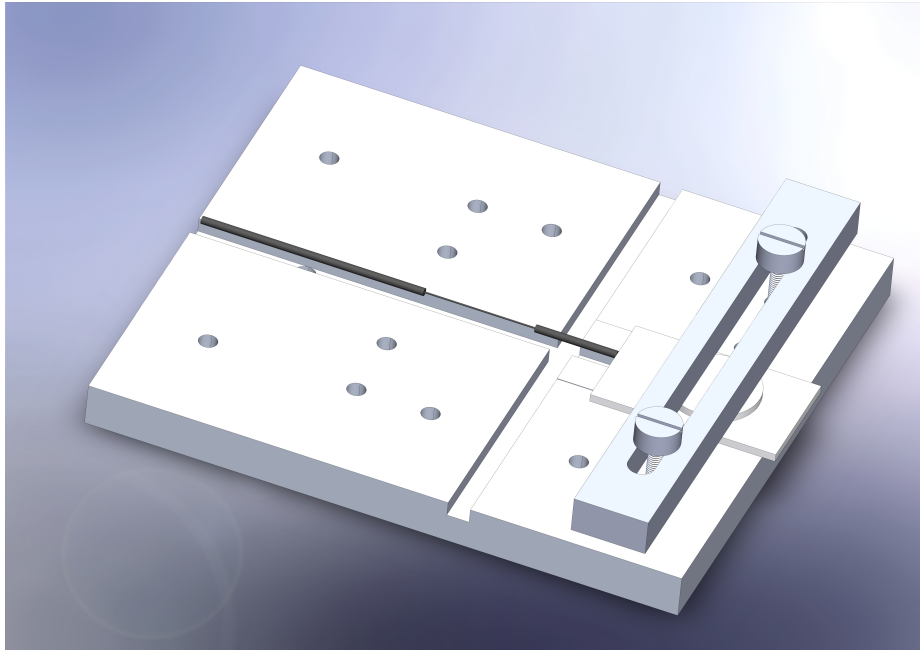


FIGURE 6.5: Schematic of the horizontal mounting. The deformation of the piezo acts orthogonally to the plate, therefore orthogonally with respect to the bending direction of the cantilever.

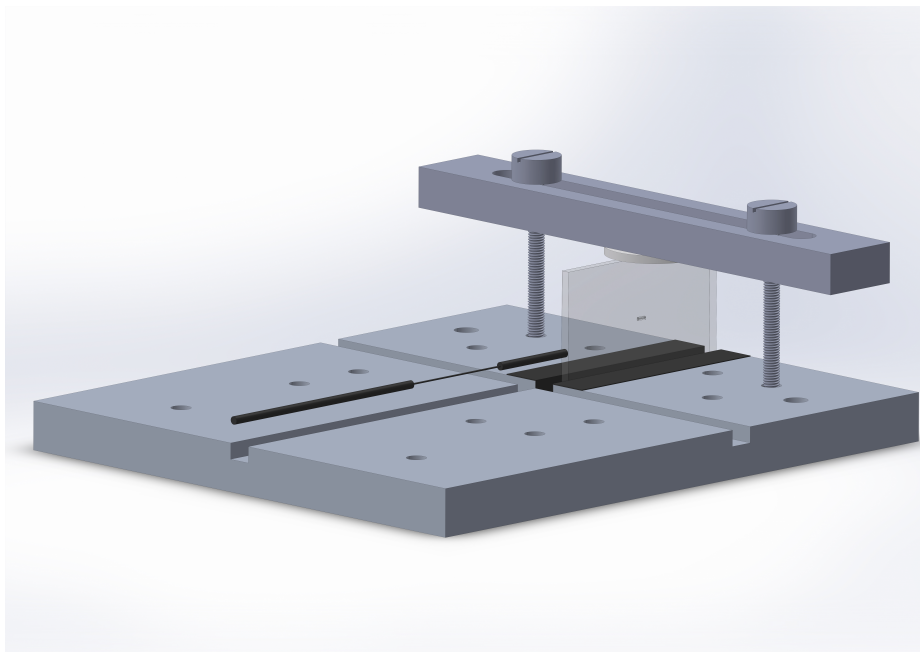


FIGURE 6.6: Schematic of the vertical mounting. The sample is lent on some layers of rubber tape that allow its vibration while maintaining it steady.

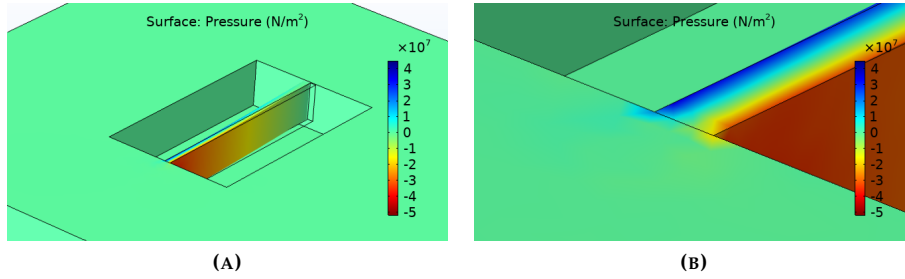


FIGURE 6.7: (A) Simulation of the pressure distribution associated to the bending of the cantilever. The close-up (B) shows that the pattern extends only in a very narrow region around the base.

What has been often done in literature [5, 15, 17, 19] is having instead the whole substrate vibrating along the bending direction of the cantilever, so that the beam is excited by a displacement that is transmitted through its base (a complete theory will be provided further on in this chapter). An advantage of having the cantilever oscillating out-of-plane with respect to the substrate is that the substrate can be simply attached to the piezoelectric plate. In our case the cantilever oscillates in-plane, so we came up with the solution represented in FIG. 6.6. We covered the aluminum plate with some layers of rubber tape. We then exploited the groove already present in the plate to host the side of the sample. The other side, facing upwards, was firmly clamped with the piezo by two screws. In such configuration, the deformation of the piezo produces a vertical vibration of the substrate and the rubber tape allows the sample to vibrate while maintaining it stable. With this configuration, we performed a fine frequency scan and we were finally able to observe clear resonant peaks of the cantilevers as a periodic modulation of the transmitted intensity. This time the interpretation of the measured signal was undoubted, as both the intensity peak and the phase shift typical of resonant behaviour (see FIG. 1.2) were evident. Our results are summarized in the following section and in TABLE 6.1 and TABLE 6.2.

### 6.2.3 Results

**Fundamental mode.** The two cantilevers are 1.2 mm and 1.5 mm long respectively. Since both cantilevers are supposed to be 50  $\mu\text{m}$  thick, they should correspond to theoretical first order resonant frequencies  $f_1 = 31.2$  kHz and  $f_2 = 19.9$  kHz (either computed through Eq. (1.27) or simulated). However, we found a significant mismatch with the actual measured frequencies, which turned out to be  $f_1^* = 23.8$  kHz (see FIG. 6.8) and  $f_2^* = 16.1$  kHz. We then went back to check precisely the dimensions of both cantilevers and we found that, whereas the *lengths* of the two were very close to the intended ones, *Cantilever 1* had a *thickness* of about 38  $\mu\text{m}$  and *Cantilever 2* had a thickness of 41  $\mu\text{m}$ , rather than the expected 50  $\mu\text{m}$  (FIG. 6.9). This was a result of the lateral apertures being slightly larger than expected by approximately 5  $\mu\text{m}$ . Re-computing the frequencies with  $t_1 = 38$   $\mu\text{m}$  and  $t_2 = 41$   $\mu\text{m}$  yielded  $f_1 = 23.7$  kHz and  $f_2 = 16.3$  kHz, in perfect agreement with the experimental values.

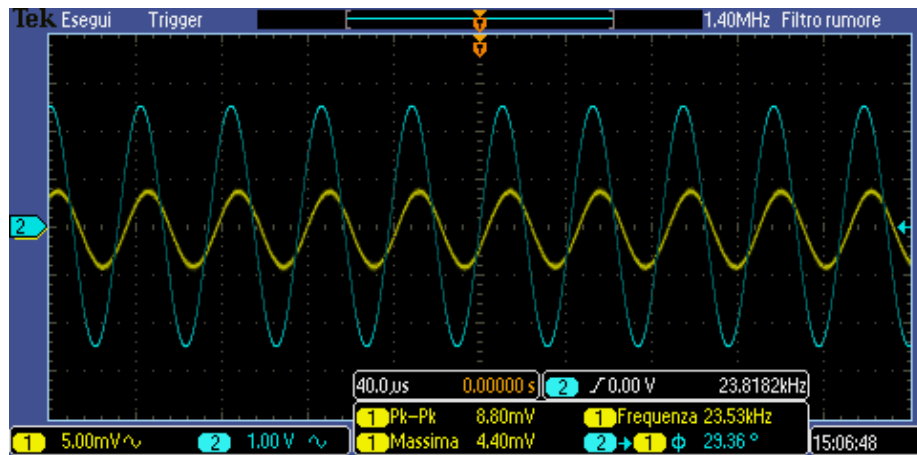


FIGURE 6.8: Fundamental oscillation mode of *Cantilever 1*. The blue line represents the signal of the function generator, which is used as reference and trigger. The yellow line is the signal of the photodiode. The measured frequency is 23.8 kHz.

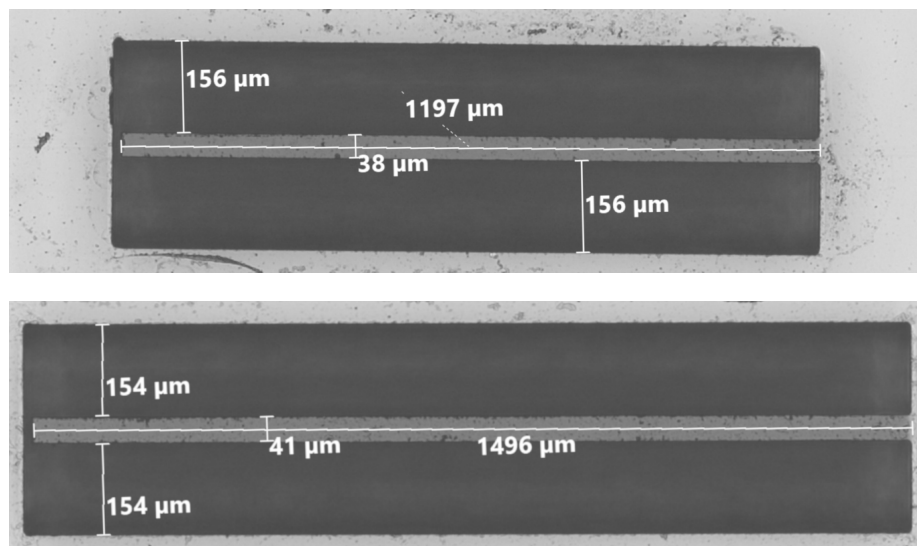


FIGURE 6.9: Actual dimensions of *Cantilever 1* and 2. Both cantilever result thinner than expected, causing a decrease of the resonant frequency.

**Higher modes.** Continuing our scan beyond the frequency of the fundamental mode, we identified several clear resonant peaks at higher frequencies. For *Cantilever 1* we individuated peaks at 23.8 kHz, 143 kHz, 148 kHz, 204 kHz, 415 kHz, 763 kHz, 806 kHz. Given the fundamental in-plane mode at 23.8 kHz, the peaks at 148 kHz, 415 kHz and 806 kHz are immediately recognized as the 2nd, 3rd and 4th order in-plane modes (again, indifferently by using Eq. (1.27) or the simulations). The other peaks can therefore only be associated to out-of-plane modes. However, the actual vertical dimension of these cantilevers turned out to be of about 260  $\mu\text{m}$ , as displayed in FIG. 6.10. This should correspond to a theoretical resonant frequency of 160 kHz, which does not match any of the measured ones. However, if we reasonably assume that the oscillation at 143 kHz corresponds to the first out-of-plane mode and we adjust the height of the cantilever to have the simulation match the measurement, then also the 763 kHz peak finds good match as the 2nd order out-of-plane mode. In detail, the vertical dimension had to be set at 237  $\mu\text{m}$ , which is considerably lower than the real value. At this point, the only peak that does not find a match is the one at 204 kHz. Our best hypothesis is that it might be connected to a torsional mode, which our simulations predicted at 236 kHz.

Similar results were found for *Cantilever 2*. The 1st order in-plane mode closely matched the predicted frequency, and higher in-plane modes were clearly individuated. For the out-of-plane modes, the measured frequency did not match the predicted one, but if the simulation was adapted to match the 1st order (in this case the vertical dimension was set at 245  $\mu\text{m}$ , closer to the real one) then also the 2nd order was retrieved. In this case, no peak associated to torsional modes was found.

TABLE 6.1 and TABLE 6.2 summarize our results.

#### 6.2.4 Discussion

**In-plane modes.** The frequencies associated to in-plane modes show a practically perfect match with the simulated ones, with errors lower than 1%. The width of the cantilever, which is what determines such frequencies, is systematically lower than designed by about 10  $\mu\text{m}$ . In other words, the cavities ablated on each side of the cantilever are larger than designed by about 5  $\mu\text{m}$  each, which leads to a shrink of the remaining part, hence a thinner cantilever. However, the behaviour seems rather systematic and predictable, so it could be easily corrected. In any case, once the actual dimension of the fabricated cantilever is taken into account, its behaviour is almost perfectly ideal.

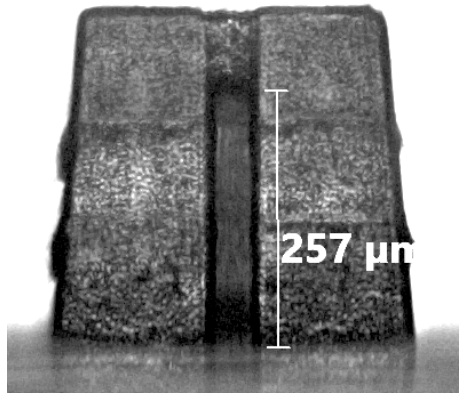


FIGURE 6.10: Side view of *Cantilever 1* with quotes.

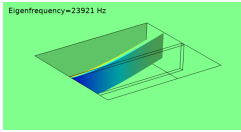
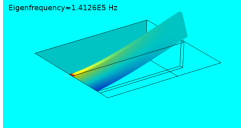
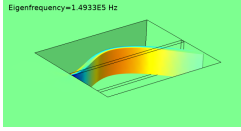
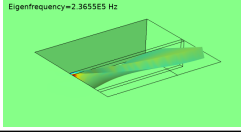
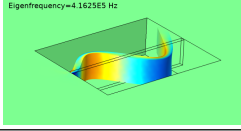
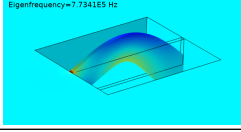
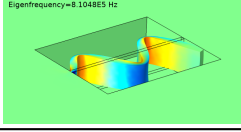
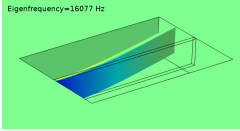
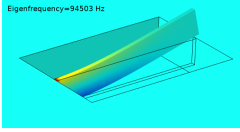
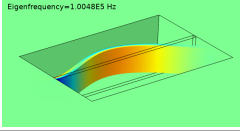
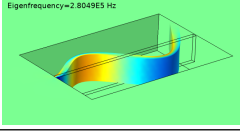
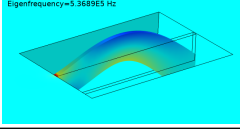
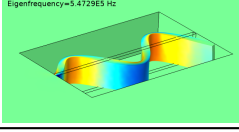
MODE	Simulation	$f_{\text{meas}}$ [kHz]	$f_{\text{sim}}$ [kHz]
1st IN PLANE		23.8	23.9
1st OFF PLANE		143	141
2nd IN PLANE		148.5	149.3
1st TORSIONAL		204	236
3rd IN PLANE		415	416
2nd OFF PLANE		763	773
4th IN PLANE		806	810

TABLE 6.1: Results of the frequency response characterization for *Cantilever 1*. In the simulation, the length and the thickness of the cantilever are set to the measured values and the material parameters (Young's modulus, density) are set according to the glass manufacturer data sheet. The width of the cantilever, which determines the frequency of the out-of-plane modes, was set to 237  $\mu\text{m}$  to match the measured frequencies.

MODE	Simulation	$f_{\text{meas}}$ [kHz]	$f_{\text{sim}}$ [kHz]
1st IN PLANE		16.1	16.0
1st OFF PLANE		94.2	94.5
2nd IN PLANE		101	100
3rd IN PLANE		282	280
2nd OFF PLANE		531	537
4th IN PLANE		551	547

**TABLE 6.2:** Results of the frequency response characterization for *Cantilever 2*. The width of the cantilever, which determines the frequency of the out-of-plane modes, was set to 245  $\mu\text{m}$  to match the measured frequencies.

**Out-of-plane modes.** The frequencies associated to out-of-plane modes are instead more difficult to match. With both cantilevers, we had to set the width (i.e. the vertical dimension) of the cantilever to a value significantly lower than the designed  $250\ \mu\text{m}$ . On the contrary, the microscope inspection showed that vertical dimensions were always slightly larger than designed, so the discrepancy between simulation and experiment is evident. Our best hypothesis is that such poor predictability, especially if compared to the perfect predictability of the in-plane modes, might be linked to the difference in surface quality between horizontal and vertical surfaces. Looking back at FIG. 6.10, the difference is evident. Furthermore, the image is taken from the side in transmission mode, so we are effectively observing a projection of the cantilever along its whole length, and we are thus unable to observe, for instance, slight variations of its width. For a definite assessment of its causes, the problem should be further investigated. In our case, as the cantilever was designed for in-plane oscillation, the matter is not critical.

**Double frequency.** As explained at the end of Sect. 4.1, for an oscillation of the cantilever at frequency  $f$  we should expect in principle an oscillation of the transmitted intensity at frequency  $2f$ , because the point of maximum transmission is supposed to be at the rest position, which is crossed twice during each oscillation period. However, if we observe FIG. 6.8 (and the same was true for any of the other measurements shown in TABLE 6.1 and TABLE 6.2), the signal from the photodiode (yellow line) always oscillates at the same frequency as the signal from the function generator (blue line). The only explanation for this is that the cantilever does *not* oscillate around the point of maximum transmission. This is compatible with the observation we pointed out in FIG. 6.2, where we noticed that indeed the maximum of transmission was not coincident with the rest position, for *Cantilever 1*. Consider now the schematics of FIG. 6.11. If the cantilever oscillates around a point that is not the transmission maximum, for small oscillations the transmission varies linearly with the displacement, so the oscillation of intensity will match the shape of the oscillation of the cantilever. For larger oscillations, the transmission curve will start to be asymmetric and the maxima will start to saturate. For even larger oscillations, the cantilever will have a second minimum when reaching the other side, and a second maximum when crossing the point of maximum transmission on the way back, thus starting to show the double frequency behaviour. The measurements of FIG. 6.11, where we varied the amplitude of the oscillation by increasing the driving voltage of the piezo, show this precise behaviour.

This specific measurement was performed on the 1st out-of-plane mode of *Cantilever 1*. With the same cantilever, we were unable to repeat the measurement on the 1st in-plane mode, as even with the highest voltage from the generator we could not reach the saturation point. In other words, we could not excite a vibration of the cantilever larger than approximately  $5\ \mu\text{m}$ , i.e. the distance of the maximum from the rest position (see FIG. 6.2). This might be an indication that the point of maximum transmission has a vertical displacement, with respect to the rest position, much smaller than the horizontal one.

On the contrary, with *Cantilever 2*, which according to FIG. 6.2 has the maximum centered on the rest position, we were always able to reach the saturation point and to see the second minimum appear. However, all oscillations showed



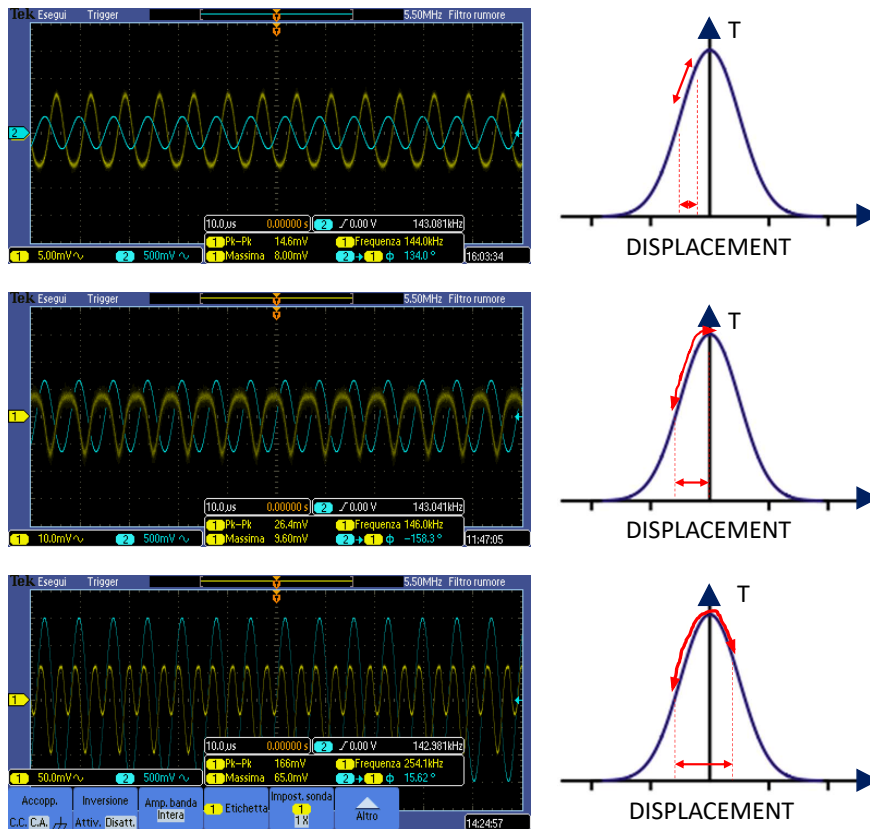


FIGURE 6.11: For small oscillations, the transmission is linear. For larger oscillations, the maxima start to saturate. For even larger oscillations, a second minimum appears.

asymmetric minima, similar to the ones of FIG. 6.11, and for small driving voltage they would invariably scale back to the single-peak behaviour. This indicates that a slight mismatch between the center of mechanical oscillation and the maximum of optical transmission is invariably present.

## 6.3 Quality factor

### 6.3.1 Theory of an harmonic oscillator actuated by the base

In Sect. 1.2.1 we showed that the idealization of the cantilever as a damped mass-spring system is justified by the fact that the displacement of the extremity is a linear function of the applied force, therefore an equivalent elastic constant can be defined (see Eq. (1.14) and Eq. (1.15)). As a result, its basic dynamic behaviour, and particularly the resonant response, can be modelled as that of a one-dimensional harmonic oscillator. However, the model we presented in Sect. 1.1 started by assuming a force applied to the mass. In the analogy, this would correspond to a force applied to the extremity of the cantilever.

Our present case is different, since the vibration of the cantilever is not excited by a direct force, but by a vibration of the whole sample, which is transmitted to the cantilever through its base. In the mass-spring analogy, this would be equivalent to exciting the vibration of the mass by moving the *other side* of the spring. Furthermore, we are not interested in the absolute position of the cantilever, because if it moves rigidly with respect to the sample we will not detect any variation of the output intensity. What we are sensing is the *deflection* of the cantilever which, in the analogy, corresponds to the length variation of the spring. Basic physical intuition would suggest that when the base oscillates at frequencies much lower than the natural frequency of the cantilever, it basically behaves like a static beam, following rigidly the displacement of the base thus giving null deflection. Conversely, if the base oscillates at frequencies much higher than the natural frequency, the tip of the beam will not be able to keep up with the oscillation, so it will basically stay still while the base moves, thus giving a deflection equal and opposite to the displacement of the base. We also expect to have a peak corresponding to the resonant frequency.

To give a mathematical model, let us consider FIG. 6.12, where  $x_1$  is the coordinate of the body and  $x_0$  of the other extremity of the spring. Let us define  $l_0$  the rest length of the spring,  $l = x_1 - x_0$  the actual length, and  $\Delta l = l - l_0 = x_1 - x_0 - l_0$  the elongation. Then the equation of motion of  $x_1$  reads as

$$\ddot{x}_1 + 2\zeta\omega_0\dot{x}_1 + \omega_0^2\Delta l = 0 \quad (6.2)$$

where the definitions of  $\zeta$  and  $\omega_0$  are the same as in Eq. (1.3). Let us write  $x_1$  in terms of  $\Delta l$  as  $x_1 = \Delta l + x_0 + l_0$ , substitute it in Eq. (6.2) and properly rearrange. We obtain the equation of motion of  $\Delta l$  as a function of  $x_0$ :

$$\ddot{\Delta l} + 2\zeta\omega_0\dot{\Delta l} + \omega_0^2\Delta l = -\ddot{x}_0 - 2\zeta\omega_0\dot{x}_0. \quad (6.3)$$

In the Laplace domain the equation reads as

$$\Delta l(s) = -\frac{s(s + 2\zeta\omega_0)}{s^2 + 2\zeta\omega_0s + \omega_0^2} x_0(s) \quad (6.4)$$

therefore the transfer function of this system is

$$T(s) = -\frac{s(s + 2\zeta\omega_0)}{s^2 + 2\zeta\omega_0s + \omega_0^2}, \quad (6.5)$$

whose corresponding Bode diagram is presented in FIG. 6.13. While it is strikingly evident, by comparing FIG. 1.2 with FIG. 6.13, that the two dynamic systems are profoundly different (the first is a low-pass, the second a high-pass filter), we demonstrate in the following that, in the limit of  $\zeta \ll 1$ , their behaviour at resonance is substantially the same.

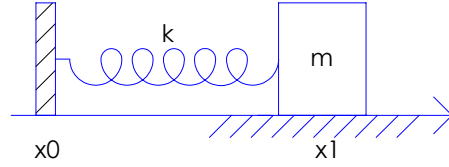


FIGURE 6.12: Damped mass-spring system.  $x_0$  and  $x_1$  define the positions of the two extremities of the spring.

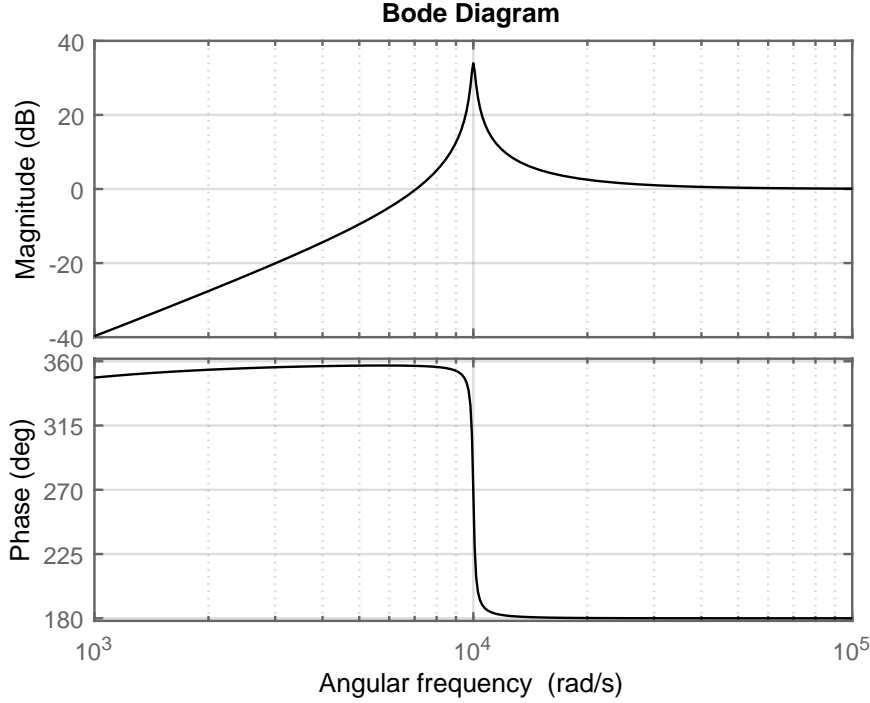


FIGURE 6.13: Frequency response of a cantilever idealized as a damped mass-spring system and actuated by the base. The plot is for  $\omega_0 = 10 \text{ krad s}^{-1}$  and  $\zeta = 0.01$ . Notice the difference of this figure with respect to FIG. 1.2. This system is a high-pass filter, while the first one is a low-pass filter.

Let us evaluate the transfer function of Eq. (6.5) in  $j\omega$  and multiply it by its complex conjugate, so to obtain:

$$|T(j\omega)|^2 = \frac{\omega^4 + 4\zeta^2\omega_0^2\omega^2}{\omega^4 + 2\omega_0^2(2\zeta^2 - 1)\omega^2 + \omega_0^4} \simeq \frac{\omega^4}{\omega^4 + 2\omega_0^2(2\zeta^2 - 1)\omega^2 + \omega_0^4} \quad (6.6)$$

The approximation is valid because, in proximity of the resonance, i.e. for  $\omega \simeq \omega_0$ , the second term of the numerator is much smaller than the first because of  $\zeta^2$ . By computing the first derivative and putting it to zero we get

$$\omega_{\max} = \frac{\omega_0}{\sqrt{1 - 2\zeta^2}}. \quad (6.7)$$

Inserting it back into Eq. (6.6) we get

$$|T(j\omega_{\max})|^2 = \frac{1}{4(\zeta^2 - \zeta^4)} \simeq \frac{1}{4\zeta^2}. \quad (6.8)$$

Now we need to find  $\omega_{\text{HM}}$  such that

$$|T(j\omega_{\text{HM}})|^2 = \frac{|T(j\omega_{\max})|^2}{2} = \frac{1}{8\zeta^2}. \quad (6.9)$$

The calculations start again from Eq. (6.6) and are tedious but ultimately trivial, once the higher powers of  $\zeta$  (like  $\zeta^4$ ) are properly neglected, and yield

$$\omega_{\text{HM}} = \omega_0 \frac{\sqrt{1 + 2\zeta - 2\zeta^2}}{\sqrt{1 - 8\zeta^2}}. \quad (6.10)$$

Now  $\Delta\omega_{\text{FWHM}} = 2|\omega_{\text{max}} - \omega_{\text{HM}}|$ . Using the well known approximation  $\sqrt{1+x} \simeq 1+x/2$  for small  $x$ , this results in

$$\Delta\omega_{\text{FWHM}} = 2\omega_0 \frac{\zeta + 2\zeta^2 - \zeta^3 + \zeta^4}{1 - 5\zeta^2 + 4\zeta^4} \quad (6.11)$$

and, once more, for small  $\zeta$  (for example  $\zeta = 0.01$ ) the first order approximation is more than sufficient, thus finally giving

$$\Delta\omega_{\text{FWHM}} = 2\omega_0\zeta \quad (6.12)$$

and consequently

$$Q_{\text{cant}} = \frac{\omega_0}{\Delta\omega_{\text{FWHM}}} = \frac{1}{2\zeta} \quad (6.13)$$

which is the same as Eq. (1.7). Finally, consider Eq. (6.8) and by the last relation we obtain

$$|T(j\omega_{\text{max}})| = Q \quad (6.14)$$

These last results are worth some comments. First, notice the difference between Eq. (1.9) and Eq. (6.7). For a standard harmonic oscillator the presence of damping produces a slightly *decrease* of the resonant frequency by a factor of  $\sqrt{1 - 2\zeta^2}$ . For an harmonic oscillator actuated "by the other side", meaning a cantilever actuated by the base, the resonant frequency *increases* by the same factor (see Sect. 1.3.1 for further discussion on this matter). Secondly, compare Eq. (1.8) with Eq. (6.14). It is obvious that, if the system is actuated by a force (as in the first case), the displacement of the body will be inversely proportional to the spring constant, hence the  $1/\omega_0^2$  factor in Eq. (1.8). This means that stiffer systems are harder to actuate and would have smaller oscillation amplitude. That is not the case for our type of actuation, because the system is driven by an imposed displacement which is independent of the stiffness. Therefore, in principle, as far as the piezo can exert enough force to make the whole sample oscillate, nothing prevents us from being able to actuate higher frequency cantilevers except, in practice, the bandwidth of the piezo itself, which is anyway much higher than the frequencies of interest.

### 6.3.2 Measurements and results

We measured the quality factor of the first in-plane and out-of-plane modes of both *Cantilever 1* and *2*. The measure was performed by executing a fine frequency scan in proximity of the resonant peak and registering the corresponding peak-to-peak amplitude of the signal from the photodiode. We took care of keeping the driving voltage low enough to be in the linear region, so that the amplitude of the measured signal varies linearly with respect to the amplitude of the mechanical oscillation. We then fitted the experimental points

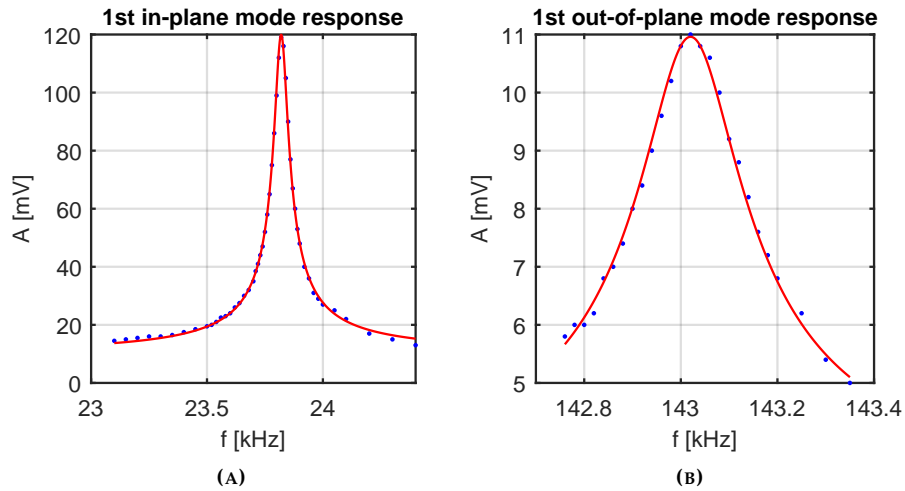


FIGURE 6.14: Frequency response of the first two oscillation modes for *Cantilever 1*. The blue dots are the experimental values, the red line is the fitted curve. (A) The fit yields  $\zeta = 1.25 \cdot 10^{-3}$  with  $R^2 = 0.999$ . (B) The fit yields  $\zeta = 7 \cdot 10^{-4}$  with  $R^2 = 0.994$ .

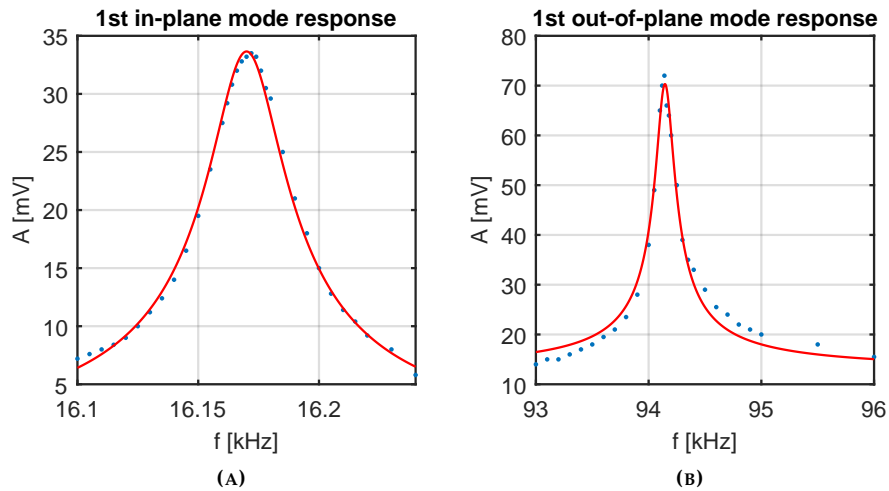


FIGURE 6.15: Frequency response of the first two oscillation modes for *Cantilever 2*. The blue dots are the experimental values, the red line is the fitted curve. (A) The fit yields  $\zeta = 9.6 \cdot 10^{-4}$  with  $R^2 = 0.996$ . (B) The fit yields  $\zeta = 8.6 \cdot 10^{-4}$  with  $R^2 = 0.987$ .

MODE	$t$ [ $\mu\text{m}$ ]	$w$ [ $\mu\text{m}$ ]	$Q_{\text{Newell}}$	$Q_{\text{Blom}}$	$Q_{\text{Hosaka}}$	$Q_{\text{Lee}}$	$Q_{\text{exp}}$
1 - IP	38	260	7900	1655	18	12	400
1 - OOP	260	38	54050	31950	317	428	714
2 - IP	41	260	5055	1510	17	11.8	520
2 - OOP	260	41	34590	24920	257	367	581

**TABLE 6.3:** Comparison between experimental values and theoretical predictions of the quality factors of, in the order, *Cantilever 1* in-plane and out-of-plane, *Cantilever 2* in-plane and out-of-plane. The following values were used in the calculations  $\gamma_{\text{air}} = 1.82 \cdot 10^{-5}$  Pa s,  $\rho_{\text{air}} = 1.225 \text{ kg m}^{-3}$ ,  $\rho_{\text{glass}} = 2380 \text{ kg m}^{-3}$ ,  $E = 73.6 \text{ GPa}$ .

with the theoretical frequency response obtained in Eq. (6.6), and the results are plotted in FIG. 6.14 and FIG. 6.15.

With the exception of the last measurement, where the tails of the curve are not precisely fitted (most likely because of a drift of transmission during the measurement) all other fits proved to be extremely accurate, with  $R^2$  higher than 0.99. This indicates that our theoretical model appropriately describes the resonant behaviour of the structures, and we can thus extract a precise value for  $\xi$ . We can then calculate the Q-factor of each resonance peak using Eq. (6.13), obtaining

$$Q_{1\text{-IP}} = 400; \quad Q_{1\text{-OOP}} = 714; \quad Q_{2\text{-IP}} = 520; \quad Q_{2\text{-OOP}} = 581; \quad (6.15)$$

where 1 and 2 stand for the respective cantilever, IP stands for the in-plane mode and OOP for the out-of-plane mode.

The interpretation of these results is not trivial. For instance, as we already discussed in Sect. 1.3, we would expect resonant peaks of higher frequency to have higher quality factors. This proved true for each cantilever, where the out-of-plane mode showed higher Q factor than the in-plane mode, which is reasonable since, for a given length  $L$ , the out-of-plane mode has a higher frequency. However, it was rather surprising to see *Cantilever 2* showing a higher quality factor than *Cantilever 1* on the fundamental in-plane mode, since *Cantilever 1* is shorter and has higher resonance frequency.

We then decided to compare our results with the predictions of some of the theoretical models presented in Sect. 1.3.2. Specifically, we compared the models by Newell, Blom (with the equivalent cross-section approximation  $R = \sqrt{wL/\pi}$ ), Hosaka and Lee. For all calculations, we assumed  $\gamma_{\text{air}} = 1.82 \cdot 10^{-5}$  Pa s,  $\rho_{\text{air}} = 1.225 \text{ kg m}^{-3}$ ,  $\rho_{\text{glass}} = 2380 \text{ kg m}^{-3}$ ,  $E = 73.6 \text{ GPa}$ . For *Cantilever 1* we set  $L_1 = 1.2 \text{ mm}$ ,  $t_1 = 38 \mu\text{m}$ ,  $w_1 = 260 \mu\text{m}$ . For *Cantilever 2* we set  $L_2 = 1.5 \text{ mm}$ ,  $t_2 = 41 \mu\text{m}$ ,  $w_2 = 260 \mu\text{m}$ . Notice that, for a given cantilever, the only difference between in-plane and out-of-plane oscillation mode is that  $t$  and  $w$  are inverted. The results are summarized in TABLE 6.3.

The predictions of the theoretical models differ from each other by orders of magnitude, and none of them seems to match our experimental results, which leads us to the conclusion that none of them is suitable for a description of our specific problem. Understanding why our case seems to elude every model is complicated by the fact that half of them heavily overestimate the actual value, while the other ones heavily underestimate it. We may speculate that a key difference from the cases reported in literature is that our cantilever

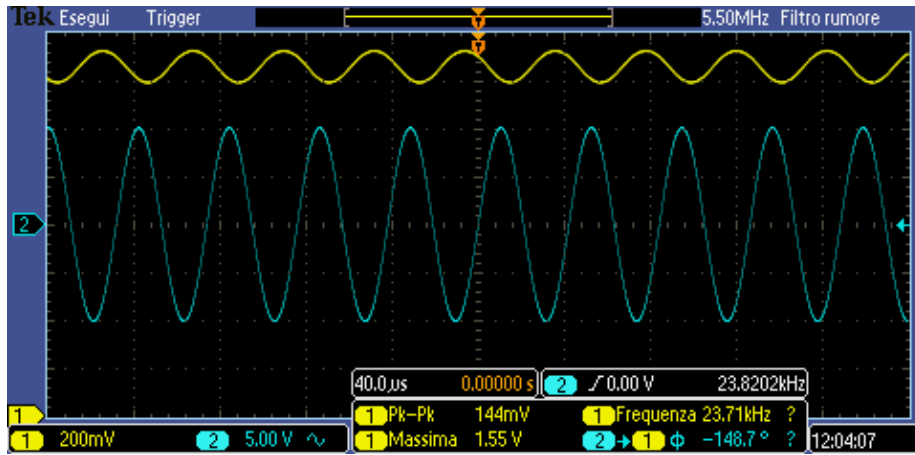


FIGURE 6.16: Largest oscillation observable with *Cantilever 1* on the 1st in-plane mode. The sinusoidal component has an amplitude of 144 mV on an overall DC signal of 1.55 V, corresponding to a modulation of approximately 9%.

operates close to the side walls, which might influence the fluid dynamics of the surrounding air. One aspect where, instead, all models seemed to find agreement, is that *Cantilever 1* should have a higher quality factor than *Cantilever 2* on its fundamental in-plane mode, which is reasonable since *Cantilever 1* is shorter. However, our experiments showed the opposite result. At this stage, we do not possess enough data to assess the problem any deeper. A further understanding would require to perform these measurements on a much wider set of cantilevers with different lengths, in such a way to be able to identify clearer patterns.

### 6.3.3 Maximum amplitude of oscillation

FIG. 6.16 shows the largest oscillation we were able to observe for the 1st in-plane mode of *Cantilever 1*. The piezo was driven at 20 V<sub>pp</sub>, i.e. the maximum output voltage of the generator. We observed an oscillation with an amplitude of 144 mV on an overall DC signal of 1.55 V, corresponding to a modulation of approximately 9%. Let us consider again the static displacement curve of FIG. 6.2. For small oscillations around the zero position the transmission curve can be well linearized, as shown in FIG. 6.17. It is then straightforward to calculate that an overall modulation of 9% must correspond to an oscillation of approximately 3 μm (±1.5 μm on each side).

Let us now consider Eq. (6.14). At the highest point of the peak, the modulus of the transfer function is equal to  $Q$ . This means that the oscillation of the cantilever is amplified by a factor of  $Q$  with respect to the oscillation of the sample. In this case we have  $Q = 400$ , therefore the sample is oscillating by approximately 7.5 nm. According to the datasheet from the producer, the piezo actuator has  $d_{33} = 400 \cdot 10^{-12}$  m/V, therefore applying a voltage of 20 V<sub>pp</sub> corresponds to an oscillation of 8 nm.

This shows that the mounting we employed (see FIG. 6.6) provides an optimal coupling between piezo and sample, as the vibration of the first is

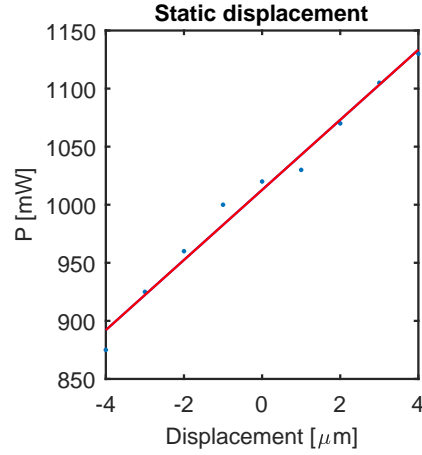


FIGURE 6.17: Detail of the transmission curve from FIG. 6.2 with regression line. The equation of the line is  $y = 30.17x + 1013$ .

almost entirely transmitted to the latter. Furthermore, it is a further proof that the theoretical model we proposed accurately describes the resonant behaviour of the cantilever with this type of actuation.

### 6.3.4 Q-factor at lower pressure

As a proof that the main limitation to the quality factor of the cantilever is the presence of air, we decided to repeat the measurement at lower pressure. We achieved it by glueing the head of a rubber hose to the sample and connecting the other extremity to a vacuum pump. By specifications, the pump should provide -0.5 bar so, except for small losses due to the connections of the tube, we can expect the pressure in the area of the cantilever to be approximately the same.

Once the data were collected, we observed the resonance frequency of the cantilever increasing from 23.83 to 23.87 kHz. More importantly, we observed the resonance peak getting higher and narrower (see FIG. 6.18). We then fitted the new curve as we did before, and we found that the Q-factor had increased from  $Q_{\text{amb}} = 400$  to  $Q_{\text{pump}} = 588$ . This is coherent with the theory proposed in [5] where, in the viscous regime, the quality factor was found to be inversely proportional to the square root of the pressure. In other words, this implies

$$Q_{\text{amb}}/Q_{\text{pump}} = \sqrt{p_{\text{pump}}/p_{\text{amb}}}.$$

In our case  $Q_{\text{amb}}/Q_{\text{pump}} = 0.68$  and  $\sqrt{p_{\text{pump}}/p_{\text{amb}}} = 0.7$  (ambient pressure corresponds to 1 bar), so in this case we find good agreement with the theory.



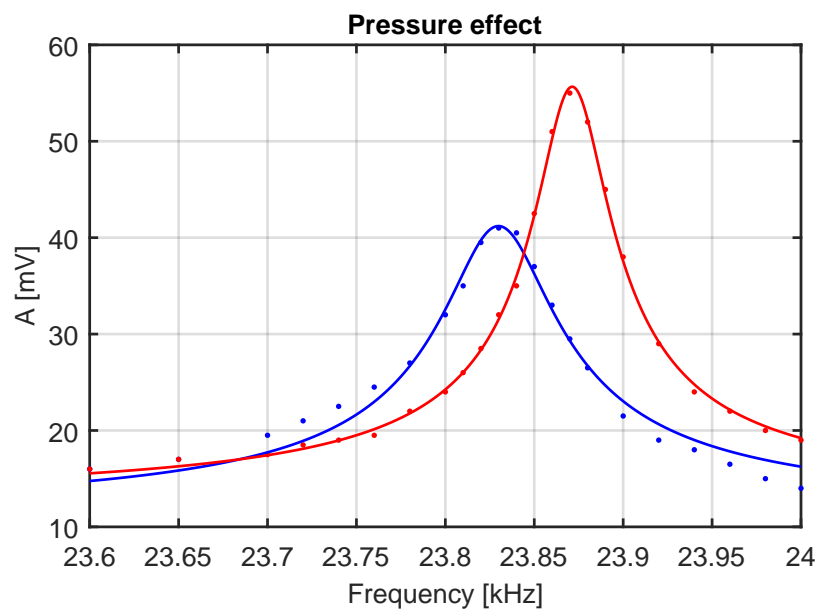


**FIGURE 6.18:** Comparison between the frequency response of the 1st in-plane mode of *Cantilever 1* at ambient pressure (blue) and at approximately 0.5 bar (red). The dots are experimental values, the solid lines fitted curves. We can observe the resonance peak moving from 23.83kHz to 23.87 kHz. The red curve provides  $\xi = 8.5 \cdot 10^{-4}$ , corresponding to  $Q_{\text{pump}} = 588$ .



# Conclusions and future perspectives

We have demonstrated a resonant optomechanical intensity modulator entirely realized by femtosecond laser micromachining.

The realization of the modulator was enabled by the optimization of a water-assisted laser ablation technique on a borosilicate glass substrate. The irradiation parameters were adjusted as a suitable trade-off between the dimensions and the surface quality of the ablated structures. We demonstrated the possibility of removing efficiently significant portions of volume and we explored a wide range of geometries.

We employed this ablation technique for the realization of a microcantilever which was fully characterized in its static and dynamic properties. We modified the standard theory of the one-dimensional harmonic oscillator to account for the particular type of actuation we employed in the dynamic characterization, obtaining a theoretical curve that provided an excellent fit of our experimental data for the shape of the resonance peak. As a result, we were able to perform a precise measurement of the quality factor of the cantilever, which proved to be higher than 400. The model also correctly accounted for the amplitude of the oscillation. Finally, we gave a proof that air damping is the most significant limitation to the quality factor of our structure by performing the measurement at lower pressure.

We have been able to demonstrate an intensity modulation in the order of 10%. This is not sufficient for employing our device as an optical shutter. However, obtaining a deeper modulation is at this point rather straightforward. On one side, the driving voltage of the piezo can be safely increased in order to obtain a larger oscillation of the cantilever. This would require an amplification stage or a generator with higher peak to peak voltage. On the other side, a waveguide with smaller mode diameter would be highly beneficial, as the same oscillation would lead to a deeper modulation of the transmitted signal. Our waveguide, which was fabricated with a 200 kHz repetition rate, had a mode diameter of 15  $\mu\text{m}$ . For the 1550 nm wavelength, mode diameters in the order or smaller than 10  $\mu\text{m}$  are routinely achieved by FLM with 1 MHz repetition rate. With shorter wavelengths in the visible range, for example a 530 nm green light, mode diameters smaller than 5  $\mu\text{m}$  are easily achievable.

This work opens several interesting perspectives. The optimization of water-assisted ablation is in itself worthy of consideration, as a significant increase in writing speed was achieved (almost ten times higher) and the possibility of performing microstructuring in borosilicate glass might open the way to a

whole new class of integrated optical devices.

As far as mechanical modulators are concerned, an interesting perspective is the exploitation of the elasto-optic effect (i.e. the change in refractive index due to a mechanical stress applied to the material) for performing fast phase shifting. In such a case, the mechanical stress caused by the oscillation of the resonator would be exploited to change the optical path of a waveguide. Preliminary simulations that we performed show that, for proper geometries of the resonator, such device would be theoretically feasible.

Finally, we should not underestimate the fact that we have effectively developed a cantilever with an integrated optical readout mechanisms. This could have impact on the applications of these cantilevers as sensors. As we pointed out in Sect. 1.4.2, external readout schemes tend to be bulky and suffer from external noise, while integrated readout schemes require specific coatings with piezoelectric or piezoresistive materials that are usually not extremely sensitive and tend to be invasive. In our case, we have developed a readout scheme that is, potentially, extremely sensitive and non-invasive. Our work is conceptually similar to the one by Dominguez *et al* [24]. However, in that case the cantilever itself was acting as a waveguide, therefore changing its dimensions (for example to tune its resonance frequency) would also change the optical properties of the scheme, while in our case the two are disentangled. Furthermore, the device presented in [24] was extremely complex, required several fabrication steps, and suffered from very high insertion losses (27 dB). Our device is instead very simple, fabricated in a single step and, despite using a waveguide far from optimal, showed a total power loss of 8 dB. Dominguez *et al* achieved an impressive resolution of 0.04 nm with their device through hard frequency filtering and noise rejection. In our case, with the instrumentation employed in our experiment, we surely have a resolution in the order or below 100 nm. Since the resolution ultimately depends on the signal to noise ratio, the fact that we have much higher transmission and that we can bring the mode diameter down to few micrometres encourages to think that, using similar noise rejection techniques, we might be able to achieve even better resolution.

# Ringraziamenti

Per quanto concerne questo lavoro di tesi, i miei primi sentiti ringraziamenti vanno senz'altro al prof. Osellame per avermi assegnato un progetto di grande respiro e ricco di sfide, e per aver creato un gruppo di ricerca straordinario sia dentro che fuori dai laboratori. Grazie ad Andrea per avermi guidato con erudita saggezza lungo tutto il percorso. Grazie ad entrambi per i tanti consigli e per l'aiuto per il mio futuro oltre il Politecnico. Un grazie anche al Politecnico stesso e alla Repubblica Italiana per avermi permesso di studiare in un'università *pubblica* di altissimo livello.

Un sentito e doveroso grazie a Francesco per gli innumerevoli consigli, per avermi affiancato durante tutta l'attività, per avermi fatto muovere i primi passi nel magico mondo del Femtobosco, ma soprattutto per il suo proverbiale know-how in fatto di *imbarcazioni* e ravioli *cannella e vaniglia*. Grazie a Petra per avermi introdotto per prima ai laboratori e per il buonumore sempre contagioso, ma soprattutto per non aver perso le speranze con uno che nel giro di una settimana è riuscito a far sparire un campione non suo e a mettere in dubbio i titoli universitari altrui. Grazie a Giacomo per avermi insegnato a usare gli hexapod, per accoppiare fibre come nessun altro può né ha mai potuto, ma soprattutto per avermi fatto conoscere Alessandro Canino. Grazie a Fede per avermi dato l'idea delle scatole a matrioska, ma soprattutto per aver organizzato tutti gli apertivi. Grazie a tutto il resto del gruppo per essere sempre stati prodighi di aiuti e consigli, tra cui i miei colleghi tesisti Alessandro, Raffaele e Roberto. Grazie soprattutto ad Ale per aver contribuito ad accrescere in modo significativo il mio – peraltro già considerevole – repertorio di battute scorrette.

Grazie ai miei coinquilini passati e presenti: Mike, Totò, Pippo, Luca, Checco, Dade, Pimer, Buch, Maranga, Tommy, Peppo, Pedo, Sbrìe, Spugna, Gaolo, Gio', Sedici, Titti, 'Ssette, Samsung, 'Ciotto, Pij, Vaz, Lollo, Gigio e Ciano. In particolare, devo ringraziare Sedici, 'Ssette, 'Ciotto e Ciano per la sequenza di soprannomi più epica che si ricordi. Grazie Gio' per non avermi mai lasciato solo la notte (*if you know what I mean*). Grazie Titti per essere stato un grande amico, anche ora che ormai sei *cintura nera*. Grazie Vaz per i "*laseroni*". Grazie a Vaz, Samsung, Sette e Ciano per le conversazioni filosofiche. Soprattutto a Ciano che avrà (forse...) il raro privilegio di essere matricola per due anni consecutivi. Grazie Sedici e Pij per ricordarmi sempre cosa ho passato prima di arrivare a questo momento. Grazie a Gigio per le chiacchierate, la Formula 1 e la play. Grazie a Lollo per aver contribuito al bene dell'umanità insegnando a Gigio come giocare alla play con le cuffie.

Grazie a Bruno e Gabriele, fedeli amici e compagni di banco e di studi, per le innumerevoli conversazioni, gli sfoghi, la memorabile serata alla fine del

primo anno, il bagno nella piscina dietro la Nave che dopo 5 anni in realtà non abbiamo mai fatto, e i pippozzi teorici di Gabri che, pure dopo 5 anni, in realtà non abbiamo mai capito. In effetti, caro Gabri, anche se sei passato al lato oscuro di quelli così teorici che alla parola *OSCILLOSCOPIO* hanno una disfunzione cardiaca, rimarrai sempre un ingegnere dentro.

Grazie ai Jupiter per essere stati la più grave minaccia sulla via della mia laurea. Una minaccia che, potessi tornare indietro, rifarei ogni singola volta, perché cantare con voi per dieci anni e dirigervi per tre è stata la più grande esperienza della mia vita, e le soddisfazioni che ho avuto con voi, come musicisti e come amici, sono impareggiabili.

Infine, il grazie più importante va sicuramente alla mia famiglia, in particolare ai miei genitori, per aver sempre avuto grande lungimiranza sull'importanza dello studio, e per avermi sostenuto in ogni mia scelta in modo totale e incondizionato. Grazie a Elia per darmi la soddisfazione di avere un fratello esageratamente buono e brillante.

Ad Anna il mio ultimo ringraziamento. Impossibile da comprendere. Impossibile da esprimere a parole. Grazie per questi anni di vita insieme. Grazie per i molti a venire.

# References

- <sup>1</sup>R. M. Langdon, "Resonator sensors - a review", *Journal of Physics E: Scientific Instruments* **18**, 103 (1985).
- <sup>2</sup>R. Bogue, "Recent developments in MEMS sensors: A review of applications, markets and technologies", *Sensor Review* **33**, 300–304 (2013).
- <sup>3</sup>M. E. Motamedi, *MOEMS : micro-opto-electro-mechanical systems* (SPIE Press, 2005), p. 614.
- <sup>4</sup>C. Bergaud, L. Nicu, and A. Martinez, "Multi-mode air damping analysis of composite cantilever beams", *Japanese Journal of Applied Physics, Part 1: Regular Papers and Short Notes and Review Papers* **38**, 6521–6525 (1999).
- <sup>5</sup>F. R. Blom, S. Bouwstra, M. Elwenspoek, and J. H. J. Fluitman, "Dependence of the quality factor of micromachined silicon beam resonators on pressure and geometry", *Journal of Vacuum Science & Technology B: Microelectronics and Nanometer Structures* **10**, 19 (1992).
- <sup>6</sup>G. Binnig, C. F. Quate, and C. Gerber, "Atomic Force Microscope", *Physical Review Letters* **56**, 930–933 (1986).
- <sup>7</sup>P. Biagioni, "Lecture notes - Principles and Applications of Atomic Force Microscopy", (2018).
- <sup>8</sup>N. V. Lavrik, M. J. Sepaniak, and P. G. Datskos, "Cantilever transducers as a platform for chemical and biological sensors", *Review of Scientific Instruments* **75**, 2229–2253 (2004).
- <sup>9</sup>S. Saadon and O. Sidek, "A review of vibration-based MEMS piezoelectric energy harvesters", in *Energy conversion and management*, Vol. 52, 1 (Jan. 2011), pp. 500–504.
- <sup>10</sup>A. Carpinteri, *Structural Mechanics-A Unified Approach*. (Taylor & Francis, 1997).
- <sup>11</sup>J. Mertens, E. Finot, T. Thundat, A. Fabre, M.-H. Nadal, V. Eyraud, and E. Bourillot, "Effects of temperature and pressure on microcantilever resonance response", *Ultramicroscopy* **97**, 119–126 (2003).
- <sup>12</sup>R. Sandberg, W. Svendsen, K. Mølhave, and A. Boisen, "Temperature and pressure dependence of resonance in multi-layer microcantilevers", *Journal of Micromechanics and Microengineering* **15**, 1454–1458 (2005).
- <sup>13</sup>J. E. Sader, "Frequency response of cantilever beams immersed in viscous fluids with applications to the atomic force microscope", *Journal of Applied Physics* **84**, 64–76 (1998).

- <sup>14</sup>W. E. Newell, "Miniaturization of tuning forks.", *Science* (New York, N.Y.) **161**, 1320–6 (1968).
- <sup>15</sup>K. Yasumura, T. Stowe, E. Chow, T. Pfafman, T. Kenny, B. Stipe, and D. Rugar, "Quality factors in micron- and submicron-thick cantilevers", *Journal of Microelectromechanical Systems* **9**, 117–125 (2000).
- <sup>16</sup>W. Zhang and K. L. Turner, "Pressure-dependent damping characteristics of micro silicon beam resonators for different resonant modes", in *Proceedings of IEEE Sensors*, Vol. 2005 (2005), pp. 357–360.
- <sup>17</sup>T. Ikehara, J. Lu, M. Konno, R. Maeda, and T. Mihara, "A high quality-factor silicon cantilever for a low detection-limit resonant mass sensor operated in air", *Journal of Micromechanics and Microengineering* **17**, 2491–2494 (2007).
- <sup>18</sup>Wei Pang, Le Yan, Hao Zhang, Hongyu Yu, Eun Sok Kim, and William C. Tang, "Ultrasensitive Mass Sensor Based on Lateral Extensional Mode (LEM) Piezoelectric Resonator", in *19th IEEE International Conference on Micro Electro Mechanical Systems* (2006), pp. 78–81.
- <sup>19</sup>H. Hosaka and K. Itao, "Theoretical and Experimental Study on Airflow Damping of Vibrating Microcantilevers", *Journal of Vibration and Acoustics* **121**, 64–69 (1999).
- <sup>20</sup>J.-H. Lee, S.-T. Lee, C.-M. Yao, and W. Fang, "Comments on the size effect on the microcantilever quality factor in free air space", *Journal of Micromechanics and Microengineering* **17**, 139–146 (2007).
- <sup>21</sup>F. Lochon, I. Dufour, and D. Rebière, "An alternative solution to improve sensitivity of resonant microcantilever chemical sensors: comparison between using high-order modes and reducing dimensions", *Sensors and Actuators B: Chemical* **108**, 979–985 (2005).
- <sup>22</sup>A. Johansson, M. Calleja, P. Rasmussen, and A. Boisen, "SU-8 cantilever sensor system with integrated readout", *Sensors and Actuators A: Physical* **123-124**, 111–115 (2005).
- <sup>23</sup>G. Meyer and N. M. Amer, "Erratum: Novel optical approach to atomic force microscopy (*Applied Physics Letters* (1988) 53, (1045))", *Applied Physics Letters* **53**, 2400–2402 (1988).
- <sup>24</sup>C. Dominguez, J. A. Plaza, K. Zinoviev, L. M. Lechuga, and V. J. C. Busto, "A Novel Optical Waveguide Microcantilever Sensor for the Detection of Nanomechanical Forces", *Journal of Lightwave Technology*, Vol. 24, Issue 5, pp. 2132–24, 2132 (2006).
- <sup>25</sup>M. Nordström, D. A. Zauner, M. Calleja, J. Hübner, and A. Boisen, "Integrated optical readout for miniaturization of cantilever-based sensor system", *Applied Physics Letters* **91**, 103512 (2007).
- <sup>26</sup>D. Du, X. Liu, G. Korn, J. Squier, and G. Mourou, "Laser-induced breakdown by impact ionization in SiO<sub>2</sub> with pulse widths from 7 ns to 150 fs", *Applied Physics Letters* **64**, 3071–3073 (1994).
- <sup>27</sup>P. Pronko, S. Dutta, J. Squier, J. Rudd, D. Du, and G. Mourou, "Machining of sub-micron holes using a femtosecond laser at 800 nm", *Optics Communications* **114**, 106–110 (1995).



- <sup>28</sup>H.-B. Sun and S. Kawata, "Two-Photon Photopolymerization and 3D Lithographic Microfabrication", in (Springer, Berlin, Heidelberg, 2006), pp. 169–273.
- <sup>29</sup>E. N. Glezer, M. Milosavljevic, L. Huang, R. J. Finlay, T.-H. Her, J. P. Callan, and E. Mazur, "Three-dimensional optical storage inside transparent materials", *Optics Letters* **21**, 2023 (1996).
- <sup>30</sup>K. Miura, J. Qiu, S. Fujiwara, S. Sakaguchi, and K. Hirao, "Three-dimensional optical memory with rewriteable and ultrahigh density using the valence-state change of samarium ions", *Applied Physics Letters* **80**, 2263–2265 (2002).
- <sup>31</sup>K. König, I. Riemann, P. Fischer, and K. J. Halhuber, "Intracellular nanosurgery with near infrared femtosecond laser pulses.", *Cellular and molecular biology (Noisy-le-Grand, France)* **45**, 195–201 (1999).
- <sup>32</sup>Y. Bellouard, A. Said, M. Dugan, and P. Bado, "Fabrication of high-aspect ratio, micro-fluidic channels and tunnels using femtosecond laser pulses and chemical etching", *Optics Express* **12**, 2120 (2004).
- <sup>33</sup>R. R. Gattass and E. Mazur, "Femtosecond laser micromachining in transparent materials", *Nature Photonics* **2**, 219–225 (2008).
- <sup>34</sup>G. Della Valle, R. Osellame, and P. Laporta, "Micromachining of photonic devices by femtosecond laser pulses", *Journal of Optics A: Pure and Applied Optics* **11** (2009) 10.1088/1464-4258/11/1/013001.
- <sup>35</sup>C. B. Schaffer, A. Brodeur, and E. Mazur, "Laser-induced breakdown and damage in bulk transparent materials induced by tightly focused femtosecond laser pulses", *Measurement Science and Technology* **12**, 1784–1794 (2001).
- <sup>36</sup>E. N. Glezer and E. Mazur, "Ultrafast-laser driven micro-explosions in transparent materials", *Applied Physics Letters* **71**, 882–884 (1997).
- <sup>37</sup>A. Brodeur and S. L. Chin, "Band-Gap Dependence of the Ultrafast White-Light Continuum", *Physical Review Letters* **80**, 4406–4409 (1998).
- <sup>38</sup>K. M. Davis, K. Miura, N. Sugimoto, and K. Hirao, "Writing waveguides in glass with a femtosecond laser", *Optics Letters* **21**, 1729 (1996).
- <sup>39</sup>K. Miura, J. Qiu, H. Inouye, T. Mitsuyu, and K. Hirao, "Photowritten optical waveguides in various glasses with ultrashort pulse laser", *Applied Physics Letters* **71**, 3329–3331 (1997).
- <sup>40</sup>A. M. Streltsov and N. F. Borrelli, "Study of femtosecond-laser-written waveguides in glasses", *Journal of the Optical Society of America B* **19**, 2496 (2002).
- <sup>41</sup>C. B. Schaffer, A. Brodeur, J. F. García, and E. Mazur, "Micromachining bulk glass by use of femtosecond laser pulses with nanojoule energy", *Optics Letters* **26**, 93 (2001).
- <sup>42</sup>C. B. Schaffer, J. F. García, and E. Mazur, "Bulk heating of transparent materials using a high-repetition-rate femtosecond laser", *Applied Physics A: Materials Science and Processing* **76**, 351–354 (2003).
- <sup>43</sup>J. W. Chan, T. Huser, S. Risbud, and D. M. Krol, "Structural changes in fused silica after exposure to focused femtosecond laser pulses", *Optics Letters* **26**, 1726 (2001).

- <sup>44</sup>S. M. Eaton, H. Zhang, P. R. Herman, F. Yoshino, L. Shah, J. Bovatsek, and A. Y. Arai, "Heat accumulation effects in femtosecond laser-written waveguides with variable repetition rate", *Optics Express* **13**, 4708 (2005).
- <sup>45</sup>C. B. Schaffer, A. Brodeur, J. F. García, and E. Mazur, "Micromachining bulk glass by use of femtosecond laser pulses with nanojoule energy", *Optics Letters* **26**, 93 (2001).
- <sup>46</sup>K. Minoshima, A. M. Kowalevich, I. Hartl, E. P. Ippen, and J. G. Fujimoto, "Photonic device fabrication in glass by use of nonlinear materials processing with a femtosecond laser oscillator", *Optics Letters* **26**, 1516 (2001).
- <sup>47</sup>S. Nolte, M. Will, J. Burghoff, and A. Tuennermann, "Femtosecond waveguide writing: A new avenue to three-dimensional integrated optics", *Applied Physics A: Materials Science and Processing* **77**, 109–111 (2003).
- <sup>48</sup>G. Cerullo, R. Osellame, S. Taccheo, M. Marangoni, D. Polli, R. Ramponi, P. Laporta, and S. De Silvestri, "Femtosecond micromachining of symmetric waveguides at 15  $\mu\text{m}$  by astigmatic beam focusing", *Optics Letters* **27**, 1938 (2002).
- <sup>49</sup>A. Arriola, S. Gross, N. Jovanovic, N. Charles, P. G. Tuthill, S. M. Olaizola, A. Fuerbach, and M. J. Withford, "Low bend loss waveguides enable compact, efficient 3D photonic chips", *Optics Express* **21**, 2978 (2013).
- <sup>50</sup>G. Corrielli, S. Atzeni, S. Piacentini, I. Pitsios, A. Crespi, and R. Osellame, "Symmetric polarization insensitive directional couplers fabricated by femtosecond laser waveguide writing", **26**, 15101–15109 (2018).
- <sup>51</sup>D. Homoelle, S. Wielandy, A. L. Gaeta, N. F. Borrelli, and C. Smith, "Infrared photosensitivity in silica glasses exposed to femtosecond laser pulses", *Optics Letters* **24**, 1311 (1999).
- <sup>52</sup>L. Gui, B. Xu, and T. Chong, "Microstructure in Lithium Niobate by Use of Focused Femtosecond Laser Pulses", *IEEE Photonics Technology Letters* **16**, 1337–1339 (2004).
- <sup>53</sup>Ik-Bu Sohn, Man-Seop Lee, and Jeong-Yong Chung, "Fabrication of optical splitter and passive alignment technique with a femtosecond laser", *IEEE Photonics Technology Letters* **17**, 2349–2351 (2005).
- <sup>54</sup>J. Liu, Z. Zhang, S. Chang, C. Flueraru, and C. P. Grover, "Directly writing of 1-to-N optical waveguide power splitters in fused silica glass using a femtosecond laser", *Optics Communications* **253**, 315–319 (2005).
- <sup>55</sup>D. K. Low, H. Xie, Z. Xiong, and G. C. Lim, "Femtosecond laser direct writing of embedded optical waveguides in aluminosilicate glass", *Applied Physics A: Materials Science and Processing* **81**, 1633–1638 (2005).
- <sup>56</sup>A. M. Streltsov and N. F. Borrelli, "Fabrication and analysis of a directional coupler written in glass by nanojoule femtosecond laser pulses", *Optics Letters* **26**, 42 (2001).
- <sup>57</sup>K. Minoshima, A. Kowalevich, E. Ippen, and J. Fujimoto, "Fabrication of coupled mode photonic devices in glass by nonlinear femtosecond laser materials processing", *Optics Express* **10**, 645 (2002).
- <sup>58</sup>W. Watanabe, T. Asano, K. Yamada, K. Itoh, and J. Nishii, "Wavelength division with three-dimensional couplers fabricated by filamentation of femtosecond laser pulses", *Optics Letters* **28**, 2491 (2003).

- <sup>59</sup>A. M. Kowalewicz, V. Sharma, E. P. Ippen, J. G. Fujimoto, and K. Minoshima, “Three-dimensional photonic devices fabricated in glass by use of a femtosecond laser oscillator”, *Optics Letters* **30**, 1060 (2005).
- <sup>60</sup>K. Suzuki, V. Sharma, J. G. Fujimoto, E. P. Ippen, and Y. Nasu, “Characterization of symmetric [3 x 3] directional couplers fabricated by direct writing with a femtosecond laser oscillator”, *Optics Express* **14**, 2335 (2006).
- <sup>61</sup>S. Eaton, W. Chen, L. Zhang, H. Zhang, R. Iyer, J. Aitchison, and P. Herman, “Telecom-Band Directional Coupler Written With Femtosecond Fiber Laser”, *IEEE Photonics Technology Letters* **18**, 2174–2176 (2006).
- <sup>62</sup>G. Li, K. A. Winick, A. A. Said, M. Dugan, and P. Bado, “Waveguide electro-optic modulator in fused silica fabricated by femtosecond laser direct writing and thermal poling”, *Optics Letters* **31**, 739 (2006).
- <sup>63</sup>A. Crespi, R. Ramponi, R. Osellame, L. Sansoni, I. Bongioanni, F. Sciarrino, G. Vallone, and P. Mataloni, “Integrated photonic quantum gates for polarization qubits”, *Nature Communications* **2**, 566 (2011).
- <sup>64</sup>L. Sansoni, F. Sciarrino, G. Vallone, P. Mataloni, A. Crespi, R. Ramponi, and R. Osellame, “Two-Particle Bosonic-Fermionic Quantum Walk via Integrated Photonics”, *Physical Review Letters* **108**, 010502 (2012).
- <sup>65</sup>A. Crespi, R. Osellame, R. Ramponi, D. J. Brod, E. F. Galvão, N. Spagnolo, C. Vitelli, E. Maiorino, P. Mataloni, and F. Sciarrino, “Integrated multimode interferometers with arbitrary designs for photonic boson sampling”, *Nature Photonics* **7**, 545–549 (2013).
- <sup>66</sup>A. Crespi, R. Osellame, R. Ramponi, V. Giovannetti, R. Fazio, L. Sansoni, F. De Nicola, F. Sciarrino, and P. Mataloni, “Anderson localization of entangled photons in an integrated quantum walk”, *Nature Photonics* **7**, 322–328 (2013).
- <sup>67</sup>A. Crespi, R. Osellame, R. Ramponi, M. Bentivegna, F. Flamini, N. Spagnolo, N. Viggianiello, L. Innocenti, P. Mataloni, and F. Sciarrino, “Suppression law of quantum states in a 3D photonic fast Fourier transform chip”, *Nature Communications* **7**, 10469 (2016).
- <sup>68</sup>F. Flamini, L. Magrini, A. S. Rab, N. Spagnolo, V. D’Ambrosio, P. Mataloni, F. Sciarrino, T. Zandrini, A. Crespi, R. Ramponi, and R. Osellame, “Thermally reconfigurable quantum photonic circuits at telecom wavelength by femtosecond laser micromachining”, *Light: Science & Applications* **4**, e354–e354 (2015).
- <sup>69</sup>P. C. Humphreys, B. J. Metcalf, J. B. Spring, M. Moore, P. S. Salter, M. J. Booth, W. Steven Kolthammer, and I. A. Walmsley, “Strain-optic active control for quantum integrated photonics”, *Optics Express* **22**, 21719 (2014).
- <sup>70</sup>B.N.Chichkov, C.Momma, S.Nolte, F. von Alvensleben, and A.Tiinnermann, “Femtosecond, picosecond and nanosecond laser ablation of solids”, *Appl. Phys* **63**, 109–115 (1996).
- <sup>71</sup>X. Liu, D. Du, and G. Mourou, “Laser ablation and micromachining with ultrashort laser pulses”, *IEEE Journal of Quantum Electronics* **33**, 1706–1716 (1997).
- <sup>72</sup>A. Marcinkevičius, S. Juodkazis, M. Watanabe, M. Miwa, S. Matsuo, H. Misawa, and J. Nishii, “Femtosecond laser-assisted three-dimensional microfabrication in silica”, *Optics Letters* **26**, 277 (2001).

- <sup>73</sup>R. Osellame, H. J. Hoekstra, G. Cerullo, and M. Pollnau, "Femtosecond laser microstructuring: An enabling tool for optofluidic lab-on-chips", *Laser and Photonics Reviews* **5**, 442–463 (2011).
- <sup>74</sup>Y. Bellouard, A. Said, M. Dugan, and P. Bado, "Fabrication of high-aspect ratio, micro-fluidic channels and tunnels using femtosecond laser pulses and chemical etching", *Optics Express* **12**, 2120 (2004).
- <sup>75</sup>R. Taylor, C. Hnatovsky, and E. Simova, "Applications of femtosecond laser induced self-organized planar nanocracks inside fused silica glass", *Laser and Photonics Reviews* **2**, 26–46 (2008).
- <sup>76</sup>Y. Shimotsuma, P. G. Kazansky, J. Qiu, and K. Hirao, "Self-organized nanogratings in glass irradiated by ultrashort light pulses", *Physical Review Letters* **91**, 1–4 (2003).
- <sup>77</sup>V. R. Bhardwaj, E. Simova, P. P. Rajeev, C. Hnatovsky, R. S. Taylor, D. M. Rayner, and P. B. Corkum, "Optically Produced Arrays of Planar Nanostructures inside Fused Silica", *Phys. Rev. Lett.* **96**, 57404 (2006).
- <sup>78</sup>P. Paiè, F. Bragheri, D. Di Carlo, and R. Osellame, "Particle focusing by 3D inertial microfluidics", *Microsystems & Nanoengineering* **3**, 17027 (2017).
- <sup>79</sup>P. Paiè, F. Bragheri, A. Bassi, and R. Osellame, "Selective plane illumination microscopy on a chip", *Lab on a Chip* **16**, 1556–1560 (2016).
- <sup>80</sup>P. Paiè, F. Bragheri, R. M. Vazquez, and R. Osellame, "Straightforward 3D hydrodynamic focusing in femtosecond laser fabricated microfluidic channels", *Lab Chip* **14**, 1826–1833 (2014).
- <sup>81</sup>F. Bragheri, P. Minzioni, R. Martinez Vazquez, N. Bellini, P. Paiè, C. Mondello, R. Ramponi, I. Cristiani, and R. Osellame, "Optofluidic integrated cell sorter fabricated by femtosecond lasers", *Lab on a Chip* **12**, 3779 (2012).
- <sup>82</sup>F. Bragheri, P. Paiè, R. M. Vazquez, A. Bassi, T. Yang, G. Nava, P. Minzioni, I. Cristiani, R. Osellame, and R. Osellame, "Optofluidic Devices for Mechanical Probing and Imaging of Cells by Laser Light", in *Advanced photonics 2018* (bgpp, ipr, np, noma, sensors, networks, sppcom, sof) (July 2018), SeTh3E.6.
- <sup>83</sup>A. Ben-Yakar and R. L. Byer, "Femtosecond laser ablation properties of borosilicate glass", *Journal of Applied Physics* **96**, 5316–5323 (2004).
- <sup>84</sup>M. D. Perry, B. C. Stuart, P. S. Banks, M. D. Feit, V. Yanovsky, and A. M. Rubenchik, "Ultrashort-pulse laser machining of dielectric materials", *Journal of Applied Physics* **85**, 6803–6810 (1999).
- <sup>85</sup>A. Y. Vorobyev and C. Guo, "Direct femtosecond laser surface nano/microstructuring and its applications", *Laser and Photonics Reviews* **7**, 385–407 (2013).
- <sup>86</sup>A. Kruusing, "Underwater and water-assisted laser processing: Part 1 - General features, steam cleaning and shock processing", *Optics and Lasers in Engineering* **41**, 307–327 (2004).
- <sup>87</sup>A. Kruusing, "Underwater and water-assisted laser processing: Part 2—Etching, cutting and rarely used methods", *Optics and Lasers in Engineering* **41**, 329–352 (2004).
- <sup>88</sup>Y. Li, K. Itoh, W. Watanabe, K. Yamada, D. Kuroda, J. Nishii, and Y. Jiang, "Three-dimensional hole drilling of silica glass from the rear surface with femtosecond laser pulses", *Optics Letters* **26**, 1912 (2001).

- <sup>89</sup>D. J. Hwang, T. Y. Choi, and C. P. Grigoropoulos, "Liquid-assisted femtosecond laser drilling of straight and three-dimensional microchannels in glass", *Applied Physics A: Materials Science and Processing* **79**, 605–612 (2004).
- <sup>90</sup>R. An, Y. Li, Y. Dou, H. Yang, and Q. Gong, "Simultaneous multi-microhole drilling of soda-lime glass by water-assisted ablation with femtosecond laser pulses", *Optics Express* **13**, 1855 (2005).
- <sup>91</sup>R. An, Y. Li, Y. Dou, D. Liu, H. Yang, and Q. Gong, "Water-assisted drilling of microfluidic chambers inside silica glass with femtosecond laser pulses", *Applied Physics A: Materials Science and Processing* **83**, 27–29 (2006).
- <sup>92</sup>X. Zhao and Y. C. Shin, "Femtosecond laser drilling of high-aspect ratio microchannels in glass", *Applied Physics A: Materials Science and Processing* **104**, 713–719 (2011).
- <sup>93</sup>Y. Li and S. Qu, "Water-assisted femtosecond laser ablation for fabricating three-dimensional microfluidic chips", *Current Applied Physics* **13**, 1292–1295 (2013).
- <sup>94</sup>H. Degawa, N. Urano, and S. Matsuo, "Laser fabrication of miniature internal thread in glass substrate", *Micromachines* **8** (2017) 10.3390/mi8020048.
- <sup>95</sup>R. Murakami, H. Nakagawa, and S. Matsuo, "Water-assisted laser drilling for miniature internal thread in glass and evaluation of its strength", *Journal of Laser Micro Nanoengineering* **12**, 203–206 (2017).
- <sup>96</sup>S. PIACENTINI, "Femtosecond laser writing of polarization insensitive photonic circuits for quantum optics and astrophotonics applications",
- <sup>97</sup>J. Bures, *Guided optics : optical fibers and all-fiber components* (Wiley-VCH, 2009), p. 344.
- <sup>98</sup>R. Osellame, V. Maselli, R. M. Vazquez, R. Ramponi, and G. Cerullo, "Integration of optical waveguides and microfluidic channels both fabricated by femtosecond laser irradiation", *Applied Physics Letters* **90**, 231118 (2007).
- <sup>99</sup>T. Juhasz, G. A. Kastis, C. Suárez, Z. Bor, and W. E. Bron, "Time-resolved observations of shock waves and cavitation bubbles generated by femtosecond laser pulses in corneal tissue and water", *Lasers in Surgery and Medicine* **19**, 23–31 (1996).
- <sup>100</sup>C. B. Schaffer, N. Nishimura, E. N. Glezer, A. M.-T. Kim, and E. Mazur, "Dynamics of femtosecond laser-induced breakdown in water from femtoseconds to microseconds", *Optics Express* **10**, 196 (2002).